DYNAMIC MAGNETIC RESONANCE IMAGING FOR TUMOR PROGNOSIS

APPROVED BY SUPERVISORY COMMITTEE

RALPH P. MASON, PH.D., C Sci., C. Chem
SUPERVISING PROFESSOR _____

PETER P. ANTICH, PH.D., D.SC _____

JIHONG WANG, PH.D. _____

DAWEN ZHAO, M.D., PH.D. _____

RODERICK MCCOLL, PH.D. _____

DYNAMIC MAGNETIC RESONANCE IMAGING FOR TUMOR PROGNOSIS

By

Lan Jiang

DISSERTATION

Presented to the faculty of the Graduate School of Biomedical Sciences
The University of Texas Southwestern Medical Center at Dallas
In partial fulfillment of the Requirements
For the Degree of

DOCTOR OF PHILOSOPHY

The University of Texas Southwestern Medical Center at Dallas
Dallas, Texas
August, 2006

DEDICATION

To

My Wife

Hong Qiao Jiang

My Two Sons

David Jiang, and Yixing (Jacky) Jiang

My parents and parents-in-law
My brothers and sisters

Whose encouragement, love, supports, and sacrifices

led to this academic accomplishment

ACKNOWLEDGMENTS

My deep gratitude goes to my mentor, Dr. Ralph P. Mason, as outstanding scientist for introducing me to MRI and the cancer research field. His enthusiasm, imagination, knowledge, good judgment, and rigorous attitude toward scientific research greatly inspired me in my research work. I deeply appreciate his constant encouragement, support in my study and research. I am very lucky to be his student.

I am very grateful as well to Dr. Dawen Zhao for his teaching and advice in MRI experiments and Dr. Anca Constantinescu for support in animal experiments. I am deeply indebted to an Advanced Radiological Sciences division chairman, Dr. Peter P. Antich, for his continuous encouragement and support in a variety of ways. I thank Drs. Roddy McColl, Paul Weatherall, Debu Tripathy, and Jihong Wang for support and advice in my clinical research. I am also grateful for their service as the members of my dissertation defense committee and their valuable suggestions to this work.

Finally, I would like to render my deepest thanks to my wife, Hong Qian Jiang, and my two sons, David Jiang and Yixing (Jacky) Jiang for their love, and sacrifices over the years. Also, I would like to thank my parents, parents-in-law, brothers, and sister in China for encouragement and support in my Ph.D. study.

While the focus of my research has been breast cancer, I had initially been included in research related to other cancers. This work was principally supported by a predoctoral research fellowship from the Department of Defense Breast Cancer Initiative (DAMD17-02-1-0592(LJ)), additionally by NIH R01 79515, and the facilities of the Rogers MR center, a NIH BTRP Facility #P41-RR02584, and the Cancer Imaging Program (Pre-ICMIC) P20 CA86354.

ABSTRACT

DYNAMIC MAGNETIC RESONANCE FOR CANCER PROGNOSIS

Publication No. _____

Lan Jiang
The University of Texas Southwestern Medical Center at Dallas, 2006

Supervising Professor: Ralph P. Mason, Ph.D., C Sic., C. Chem.

Breast and prostate cancers are the most common non-smoking cancers among American women and men. Radiotherapy and chemotherapy in conjunction with surgery are the most common treatment protocols in the clinic. However, a lot of experimental and clinical studies have shown that tumor hypoxia and the microcirculation play a very important role in cancer progression and therapy. There is strong evidence that hypoxic cells are one of the major reasons for failure to control tumors with conventional radiotherapy and chemotherapy. Several approaches (hyperthermia, and carbogen inhalation), which improve tumor oxygenation during radiotherapy and chemotherapy, have been used in clinical trials. There is increasing demand for tumor prognostic information in the clinical setting. So far, increasing clinical data have indicated that poorly oxygenated tumors have poor prognosis. To better understand the underlying tumor physiological mechanisms, it is very important to develop novel non-invasive approaches to accurately assess tumor microcirculation and oxygenation for further therapy planning. However, these parameters have been extremely difficult to assess in routine clinical practice and have therefore not been easily integrated in to general patient care.

With development of MRI the non-invasive technique, BOLD (Blood Oxygenation Level Dependent) contrast MRI, has been widely used for neuroscience research to detect brain activations. Because deoxyhemoglobin ($dHbO_2$) is paramagnetic and oxyhemoglobin (HbO_2) is non-magnetic, the change of concentration of deoxyhemoglobin and oxyhemoglobin can cause a Bulk Magnetic Susceptibility (BMS) change and the T2* signal response during MR imaging. Here, I applied this technique to assess tumor physiological characteristics. In order to study the BOLD mechanism, I designed a phantom system and built it for *in-vitro* study. Since inhalation of oxygen could cause variation in the blood flow and oxygenation, and BOLD MRI is sensitive to both these factors, it becomes very important to explore the correlation between the BOLD response and these two factors. Considering the different vascular orientation, the angle between vessel and the static magnetic field (B_0) could be further analyzed in phantoms. The phantom study showed that contribution of oxygenation was much higher than that of flow to the BOLD signal. Interestingly, a signal decrease was observed in extra-vessel region accompany increasing intra-vessel oxygenation.

The DCE (Dynamic Contrast Enhanced) and BOLD MRI have been compared in the animal experiments and the clinical setting. The experimental pre-clinical results showed that tumor sublines with different vascular development showed different DCE and BOLD regional response. This correlation between DCE and BOLD in regional response indicated the potential value of BOLD technique in tumor physiological research.

Finally, the clinical results showed there is prognostic value in DCE and BOLD MRI. There is high correlation between high BOLD response and good therapeutic outcome. BOLD and DCE MRI provide novel non-invasive prognostic tools for the clinic. It provides new insight into tumor physiological changes during chemotherapy and radiotherapy. I found correlation between BOLD response in tumors accompanying oxygen breathing and the clinical response of advanced local breast to chemotherapy. This technique could early become a routine addition to the clinical setting benefiting cancer patient population in near future.

PUBLICATIONS ARISING FROM THIS RESEARCH

PAPERS

1. Dawen Zhao, Anca Constantinescu, **Lan Jiang**, Eric W. Hahn, and Ralph P. Mason. Prognostic Radiology: Quantitative Assessment of Tumor Oxygen Dynamics by MRI.*Am. J Clin Oncol.* 24(5):462-466, 2001.
2. Dawen Zhao, **Lan Jiang**, and Ralph P. Mason. Measuring changes in tumor oxygenation. *Methods Enzymol.* 386, 378-418, 2004.
3. **Lan Jiang**, Dawen Zhao, Anca Constantinescu and Ralph P. Mason. Comparison of BOLD contrast and Gd-DTPA Dynamic Contrast Enhanced imaging in rat prostate tumor. Magn. Reson. Magn. Reson. Med. 51, 953-60, 2004.
4. Dawen Zhao, **Lan Jiang**, Anca Constantinescu, Eric W. Hahn, and Ralph P. Mason. Continuous low-dose (metronomic) chemotherapy on rat prostate tumors evaluated using MRI *in vivo* and comparison with histology. *Neoplasia,* 7, 678-87, 2005.
5. Dawen Zhao, **Lan Jiang**, Eric W. Hahn, and Ralph P. Mason. Tumor physiological response to combretastatin A4 phosphate assessed by MRI. *Int. J. Radiat. Oncol. Biol. Phys.* 62(3):872-880, 2005.

ABSTRACTS

1. Zhao, D., **Jiang, L**., Constantinescu, A., Hahn , E. W., Mason R. P. Comparison of tumor blood flow and oxygen dynamics in two diverse Dunning prostate tumor sublines. #2088, Proc. *92nd AACR,* New Orleans, Mar. 2001
2. Zhao, D., **Jiang, L**., Constantinescu, A., Hahn, E.W., and Mason, R.P. Insight into interdependent parameters of tumor blood flow and oxygenation. #3 MS10. *48th Radiat. Res. Soc.* San Juan, Peurto Rico, Apr 2001.
3. Zhao, D., Constantinescu, A., **Jiang, L**., Chang, K., Gall, K., Hahn, E.W., and Mason, R.P. Prognostic Radiology: the value of *FREDOM*. Proc. EPR Viable Systems *9th International Meeting*, #S-8, Dartmouth, NH, Sep 2001
4. Zhao, D., **Jiang, L**., Constantinescu, A., Hahn, E.W., and Mason, R.P. *In vivo* MRI monitoring of prostate tumor vasculature and oxygen dynamics. *AACR New Discoveries in Prostate Cancer Biology and Treatment*, # B-56, Naples, FL, Dec 2001.
5. **Jiang, L**., Zhao, D., Constantinescu, A., Hahn, E.W., and Mason, R.P. Assessment of tumor vasculature by comparison of BOLD and Gd-DTPA contrast enhanced MRI in prostate tumors. *4th International Symposium on Anti-Angiogenic Agents*, Dallas, TX, Jan 2002.

6. **Jiang, L**., Zhao, D., Constantinescu, A., Hahn, E.W., and Mason, R.P. Comparison of BOLD and Gd-DTPA contrast enhanced MRI for the assessment of the two prostate tumor sublines exhibits different vascular development. *10th ISMRM,* Honolulu, Hawaii, May 2002.

7. **Jiang, L**., Zhao, D., Constantinescu, A., Hahn, E.W., and Mason, R.P. Assessing tumor vasculature by MRI: comparison of prostate tumor sublines known to exhibit different vascular development. *8th International Workshop on Tumor Microenvironment and Its Impact on Cancer Therapies*, Miami, FL, May 2003.

8. Zhao, D., **Jiang, L**., Constantinescu, A., Hahn, E.W., and Mason, R.P. Interrogation of tumor vasculature and oxygenation by integrated ^{1}H and ^{19}F MRI. *51st Radiat. Res. Soc*. St. Louis, MO, Apr 2004.

9. Zhao, D., **Jiang, L**., Constantinescu, A., Hahn, E.W., and Mason, R.P. Evaluation of breast tumor microcirculation and oxygenation using a combination of BOLD, DCE and ^{19}F MRI. *11th ISMRM,* # 220, Kyoto, Japan, May 2004.

10. Bourke, V., Gilio, J., **Jiang, L**., Constantinescu, A., Zhao, D., Kodibagkar, V., and Mason, R.P. Further Validation of MR Oximetry as a Useful Prognostic Indicator of Tumor Radiation Response. *11th ISMRM,* #2025, Kyoto, Japan, May 2004.

11. Bourke, V., Gilio, J., Zhao, D., Constantinescu, A., Kodibagkar, V., **Jiang, L**., Hahn, E.W., and Mason, R.P. Correlation of Tumor Oxygen Dynamics with Radiation Response of the Dunning Prostate R3327-AT1 Tumor. *51st Radiat. Res. Soc*. St. Louis, MO, Apr 2004

12. **Jiang,L.**, McColl, R., Weatherall, P., Tripathy, D., Mason, R.P. BOLD and Gd-DTPA Contrast Enhanced MRI for Early Assessment of Breast Cancer Chemotherapy. *13th ISMRM*, Miami, May. 2005

13. **Lan Jiang**, Roddy McColl, Paul Weatherall, Debu Tripathy, Ralph P. Mason. Using BOLD and GD-DTPA Contrast Enhanced MRI for Early Evaluation of Breast Cancer Chemotherapy. *Era of Hope 2005* for the Department of Defense (DOD) Breast Cancer Research Program (BCRP) , June 8-11, 2005, Philadelphia, Pennsylvania.

14. **Lan Jiang**, Roddy McColl, Paul Weatherall, Debu Tripathy, Ralph P. Mason. Blood Oxygenation Level Dependent (BOLD) contrast MRI for early evaluation of breast cancer chemotherapy. *The 28th Annual San Antonio Breast Cancer Symposium*, December 8 - 11, 2005. San Antonio, TX

15. **Lan Jiang**, Roddy McColl, Ralph P. Mason. BOLD Phantom Investigations of the Relationship between Blood Oxygenation, Flow Variation and Intra- and Extra-vessel Signal Change. *14th ISMRM*, Seattle, May. 2006

16. **Lan Jiang,** Roddy McColl, Paul Weatherall, Debu Tripathy, Ralph P. Mason. Blood Oxygenation Level Dependent (BOLD) and Gd-DTPA contrast MRI for early evaluation of breast cancer chemotherapy. *14th ISMRM*, Seattle, May. 2006

TABLE OF CONTENTS

LIST OF FIGURES

CHAPTER 2

CHAPTER 3

CHAPTER 4

CHAPTER 5

LIST OF TABLES

CHAPTER 2

CHAPTER 3

CHAPTER 4

CHAPTER 5

LIST ABBREVIATION

AUC (Area Under Curve)

ARCON (Accelerated Radiotherapy with CarbOgen and Nicotinamide)

ANOVA(ANalysis Of VAriance)

B_0 (static magnetic field direction)

BMS (Bulk Magnetic Susceptibility)

BOLD (Blood Oxygenation Level Dependent)

CA4P (Combretastatin A4 phosphate)

CPMGT2 (Carr-Purcell Meiboom-Gill T2)

CSF (CerebroSpinal Fluid)

DCE (Dynamic Contrast Enhanced)

DMXAA (5,6-DiMethylXanthenone-4-Acetic Acid)

$dHbO_2$ (Deoxyhemoglobin)

EES (Extravascular Extracellar Space)

FLASH (Fast Low-Angle SHot)

FLOOD (FLOw and Oxygenation Dependent)

FOV (Field Of View)

fMRI (functional MRI)

FREDOM (Fluorocarbon Relaxometry Using Echo Planar Imaging for Dynamic Oxygen Mapping)

Gd-DTPA (Gadolinium DiethyleneTriamine Penta-acetic Acid)

GRE (GRadient Echo)

HbO_2 (Oxyhemoglobin)

HF (Hypoxic Fraction)

HFB (HexaFluoroBenzene)

IAUC (Initial Area Under Curve)

MRI (Magnetic Resonance Imaging)

NIR (Near InfRrared)

Re.N (Reynolds Number)

SaO_2 (Arterial Oxygen Saturation)

TE (Echo Time)

TR (repetition Time)

VDT (Volume Doubling Time)

VTA (Vascular Targeting Agent)

CHAPTER 1

INTROUCTION

Great progress has been made in the detection of breast cancer, particularly from increased public awareness, and widespread mammography. Furthermore, novel diagnostic devices (*e.g.,* MRI) and therapeutic modalities (*e.g.,* cryotherapy, brachytherapy, immunotherapy) offer increasingly versatile, and complex choices to medical oncologists (1). However, 180,000 new cases of breast cancer are diagnosed each year in the United States and despite improved therapeutic success, 46,000 deaths occur annually. New therapies are under development, but a crucial issue remains the choice of optimal therapeutic approach, particularly for non-surgical procedures. Considerable experimental and clinical studies have demonstrated that microcirculation and oxygenation play a very important role in the responsiveness of tumors including breast tumor to cytotoxic treatment. In chemotherapy and immunotherapy, tumor perfusion, capillary permeability, and interstitial pressure are crucial factors in the delivery of therapeutic agents. Numerous studies have provided evidence that poor vascular supply and the presence of hypoxic cells are critical factors contributing to treatment failure after radiation therapy (2-9).

Tumor microcirculation and oxygenation have long been implicated as important determinants of radiation therapy and chemotherapy response. However, these parameters have been extremely difficult to assess in routine clinical practice and have

therefore not been easily integrated into general patient care. With the advances of functional MRI, and the adaptation of perfusion MRI to oncological imaging, a new method of assessing tumor microcirculation has recently become available in clinical practice (10-13). The dynamic contrast MRI used in human studies is based on the combination of rapid dynamic MRI techniques and bolus injection of gadolinium (Gd) contrast agent. In extra cranial tissues, T1-weighted imaging methods based on conventional spin-echo, or gradient-echo techniques, such as fast low-angle shot (FLASH) or snapshot FLASH, are usually employed (14,15). The Blood Oxygenation Level Dependent (BOLD) mechanism utilized in MRI provides a noninvasive means to evaluate the success of oxygen intervention and to gain an understanding of tumor hypoxia (16-19). In BOLD imaging, the paramagnetic property of blood produces bulk susceptibility differences between a blood vessel and the surrounding tissue, producing resonance frequency shifts in extra-vessel molecules (20-23). The BOLD effect is sensitive to venous blood volume and to vessel size and oxygenation (14,15). The BOLD technique has been used to analyze vessel function *in vivo* (24,25). The inhaled oxygen may itself provide a useful contrast agent for proton MRI in terms of BOLD contrast changes. Reports have shown that, as an intrinsic contrast, the BOLD MR method is being explored as a noninvasive means to monitor local changes of microcirculation and oxygenation in tumors (26-32).

The historic work by Ogawa *et al.* (20) and Thulborn *et al.* (24) suggested that the oxygenation state of blood could produce contrast in proton MRI. Specifically, deoxyhemoglobin is paramagnetic and leads to signal loss in T_2 weighted images. This phenomenon is the basis of traditional functional MRI (fMRI), whereby changes in O_2

consumption or delivery in response to external stimulation (*e.g.,* finger flexion, auditory, or visual excitation) has been observed in the brain (33), Others have investigated the oxygenation of major blood vessels based on T_2 contrast (34). Tumors present a more difficult target since vessels are generally microscopic and may be highly tortuous (35-37). While there are equations relating MRI signal to hemoglobin saturation (SaO_2), hemoglobin concentration (Hb), and flow in vessels (38,39), the mixed signal of blood and tissue obtained from tumors has limited application of the BOLD technique.

Assessment of tissue microcirculatory parameters such as perfusion, blood volume, and capillary permeability using MR imaging techniques is gaining popularity (10-13). Tumor enhancement patterns observed by dynamic contrast-enhanced magnetic resonance imaging have recently emerged as a promising method to assess response to cytotoxic therapy in various malignancies and has been a subject of recent study (40,41). The Blood Oxygenation Level Dependent (BOLD) method has been applied to examine oxygenation of brain tumors in the clinic. Indeed there have been several reports of BOLD investigations of clinical brain tumor and limited studies of other sites (42,43). The studies have shown that, in BOLD imaging, the paramagnetic property of blood produces Bulk Magnetic Susceptibility (BMS) difference between a blood vessel and the surrounding tissue, producing resonance frequency shifts in extra-vessel molecules (16,18,20,21,24,44-46). As an intrinsic contrast agent, compared with Gadolinium injection, inhaled oxygen is non-invasive to patients, easy to implement clinically, reproducible multiple times, allowing for tumor response monitoring during therapy. The BOLD technique is influenced by a combination of hemoglobin saturation (SaO_2), hemoglobin concentration (Hb), and blood flow in vessels (35).

Phantoms have been widely used to study MR imaging including vasculature and blood flow *in vitro* (47). There are many advantages to using an inanimate vascular phantom instead of a living subject, in particular, the ability to isolate and control specific parameters (48). I studied the MRI BOLD signal, which is related to hemoglobin concentration and blood flow in microvascular phantom, especially the "steal effect". By studying the relationship between changes of blood hemoglobin state, blood flow and MRI BOLD signal, I sought new understanding of BOLD characteristics.

Objective/Hypothesis: The fundamental hypothesis is that oxygen inhalation will generate contrast in proton MRI (BOLD effect), which will provide insight into breast tumor microvasculature and potentially therapeutic prognosis. By combining studies in phantoms, rat tumor models and clinical breast tumor data, I investigated the reliability of measurements, as a foundation for potential clinical application.

Aim: three specific aims:

1. Quantitatively relate MRI signal to oxyhemoglobin / deoxyhemoglobin concentration, and blood flow in phantom system. Explore the BOLD signal related to variation in oxygenation and blood flow in the vessel and signal loss during oxygenation change
2. Study animal tumor microvascular distribution, perfusion and oxygenation using BOLD, DCE MRI techniques and correlate with histological analysis in tumor hypoxia.

3. Translate BOLD and DCE MRI to clinical setting for early assessment of breast cancer chemotherapy.

CHAPTER 2

BACKGROUND OF HEMOHYNAMICS AND PHANTOM DESIGN

2.1 Introduction

BOLD as a functional imaging technique has been applied in neuroscience to study brain function (20,21). It has been used in cancer research for detecting physiological changes (36,49,50). The previous studies showed BOLD signal is related to change of the blood oxygenation and the blood flow, so called FLOOD (Flow and Oxygenation Level Dependent). It is impossible to control these parameters separately in *in-vivo* study. A phantom system can provide a possibility to study each parameter related to the BOLD signal. Phantom study has been widely used in medical research. It is easy to minimize other factors and to focus on specific factors without physiological limitation. Phantom design is based on the knowledge of fluid dynamics, hemodynamics and background reviewed here.

2.2 Basic Hemodynamics

Hemodynamics concerns the physical factors governing blood flow within the circulatory system. Blood flow through an organ or any vascular network is driven by a pressure gradient or perfusion pressure that is normally represented by the difference between the arterial and venous pressures across the organ. The actual blood flow at any given pressure gradient is determined by the resistance to blood flow. The relationship between flow, pressure, and resistance is given below (51):

$$F = \frac{\left(P_A - P_V\right)}{R} = \frac{\Delta P}{R} \qquad (2\text{-}1)$$

where F = flow, P_A and P_V = mean arterial and mean venous pressures, respectively, and R = resistance to flow (termed vascular resistance). (The perfusion pressure is sometimes denoted as Δ P). This relationship is a hydrodynamic form of Ohm's Law where current (I) equals the voltage (V) divided by resistance (R).

2.2.1 Flow Resistance

There are three primary factors that determine the resistance to blood flow within a single vessel: diameter (or radius), length, and viscosity of the blood (51).

$$R \propto \frac{\eta \cdot L}{r^4} \qquad (2\text{-}2)$$

Vessel resistance (R) is directly proportional to the length (L) of the vessel and the viscosity (η) of the blood, and inversely proportional to the radius to the fourth power (r^4).

Therefore, a vessel having twice the length of another vessel (and each having the same radius) will have twice the resistance to flow. Similarly, if the viscosity of the blood increases 2-fold, the resistance to flow will increase 2-fold. In contrast, an increase in radius will reduce resistance. Furthermore, the change in radius will alter resistance to the fourth power. For example, a 2-fold increase in radius will decrease resistance by 16-fold. Therefore, vessel resistance is exquisitely sensitive to changes in radius (or diameter).

If the above expression for resistance is combined with the equation describing the relationship between flow, pressure and resistance (F=Δ P/R), then

$$F \propto \frac{\Delta P \cdot r^4}{\eta \cdot L} \qquad (2\text{-}3)$$

2.2.2 Type of Flow in Vessel

The blood flow in a vessel can be divided into two different types. Laminar and turbulent flow

- Laminar Flow

This flow is smooth or streamlined. It is called laminar because the blood flows in layers or laminar in smooth-walled vessels. These layers slide over each other, creating a parabolic (ie, curvelike) profile of laminar flow. This profile indicates parallel movement of molecules. The velocity of flow differs in each layer. Those layers toward the center flow fastest, those closer to the wall flow more slowly, and those against the wall do not move at all.

Laminar flow is the normal condition throughout most of the circulatory system and is characterized by concentric layers of blood moving in parallel down the length of a blood vessel. The highest velocity (Vmax) is found in the center of the vessel. The lowest velocity (V=0) is found along the vessel wall. The flow profile is parabolic once laminar flow is fully developed. This occurs in long, straight blood vessels, under steady flow conditions (Figure 2.1).

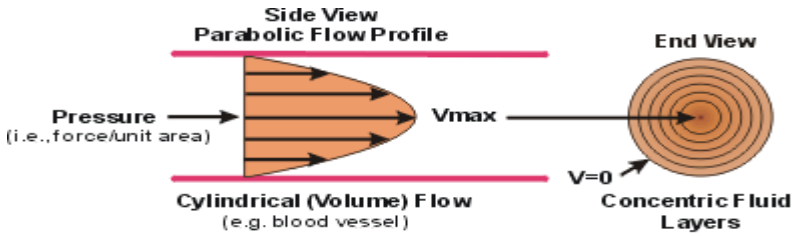

Figure 2.1 Laminar flow
(Graph from: www.oucom.ohiou.edu/CVPhysiology)

One practical implication of parabolic, laminar flow is that when flow velocity is measured using a Doppler flowmeter, the velocity value represents the average velocity of a cross-section of the vessel, not the maximal velocity found in the center of the flow stream.

Under ideal *laminar flow* conditions where vascular resistance is independent of flow and pressure, this relationship can be expressed as (51):

$$R = \frac{8 \cdot \eta \cdot L}{\pi \cdot r^4} \qquad (2\text{-}4)$$

Then, the flow is

$$F = \frac{\Delta P}{R} = \frac{\Delta P \cdot \pi \cdot r^4}{8 \cdot \eta \cdot L} \qquad (2\text{-}5)$$

This relationship (**Poiseuille's equation**) was first described by the French physician Poiseuille (1820). It is a description of how flow is related to perfusion pressure, radius, length, and viscosity. In the body, however, flow does not conform quantitatively to this relationship because this relationship assumes long, straight

tubes (blood vessels), a Newtonian fluid (e.g., water, not blood, which is non-Newtonian), and steady, laminar flow conditions.

- Turbulent Flow

Turbulence occurs when smoothly flowing, laminar flow is disrupted. This occurs at vessel branch points, and in the ascending aorta at high cardiac ejection velocities (Figure 2.2).

This flow is not streamlined, but moves crosswise, generating whorls, eddies, or swirls. These patterns occur as a result of obstructions or uneven edges in the vessel walls, such as occurs in atherosclerosis or in areas of shear stress (*i.e.,* the tendency for the vessel epithelium to be pulled along by the flowing blood, which causes it to deform). Injury occurs especially at points, where arteries branch

Figure 2.2 Turbulent flow
(Graph from: www.oucom.ohiou.edu/CVPhysiology)

The onset of turbulence under ideal conditions can be predicted by calculating the Reynolds number (Re) (51,52):

$$\mathrm{Re} = \frac{\left(\bar{v} \cdot D \cdot \rho\right)}{\eta} \qquad (2\text{-}6)$$

Where v = mean velocity, D = vessel diameter, ρ blood density, and η blood viscosity

- If Re.N. < 2,000 laminar flow
- If Re.N. > 3,000 turbulent flow

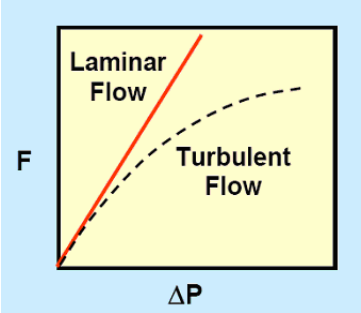

Figure 2.3 Laminar and Turbulent flow
(Graph from: www.oucom.ohiou.edu/CVPhysiology)

Turbulence causes energy losses that greatly exceed those predicted by Poiseuille's law, for Laminar flow conditions (Figure 2.3).

2.2.3 Vascular hemodynamic parameters

My goal was to design a phantom with controlled laminar flow (Re.N. < 2,000). And I referred to cardiovascular parameters of dog (Table 1) (53). It shows the turbulent flow mostly occurring in ascending aorta and big artery branch region, with the Laminar flow in capillaries. The mean microvascular flow velocity of rat a tumor is about 0.67 cm/s (54). Thus, I tried to use low flow conditions, although my studies were limited by the sensitivity of flowmeter and pump function.

Table 2.1 Dog cardiovascular parameters (53)

	Ascending aorta	Arteriole	Capillary	Venule
Internal diameter (cm)	1.5	0.005	0.0006	0.004
Blood velocity (cm/s)	20	0.75	0.07	0.35
Reynolds number	4500	0.09	0.001	0.035

2.3 Phantom Designs

Previous studies showed that the BOLD signal is related to change in the blood oxygenation and flow (21). Distinguishing the contribution of these factors to the BOLD signal is very important for understanding the physiological meaning. However, it is hard to distinguish the contribution of these two factors *in vivo*. The *in vitro* phantom study could be the best way to separately study these factors. BOLD responses signals mainly arise from the capillaries and venules in the tissue because this is related to the biggest oxygenation changes occur *in vivo*. However, the blood flow at the capillary (microcirculation) level is totally different from flow in the arteries. The flow in the capillaries and venules has specific characteristics: low Reynolds number, smooth flow and low flow velocity status. I designed and built the special phantom system.

2.3.1 Circulatory System

Considering the characteristics of capillaries and venules *in vivo*, I considered the following parameters: small diameter of "vessel", relatively smooth flow, low flow velocity, low Reynolds number and oxygenation level changeable. Since it is hard to find elastic tubing and special pump simulating heart pulse, I used non-elastic tubing and a regular pump although this could cause big pulses. Based on my previous experience in fluid dynamics, a circulatory phantom system was designed and built for MR study (Figure 2.4). The phantom consisted of pumps, windkessel units, oxygenation unit, flow regulation unit, vessel phantom unit, and various diameter tubing. The pump used to simulate the heart, the Windkessel unit used to get the compliance of arteries in the circulatory system, especially simulating aorta function. The oxygenation unit, which is built from hollow fibers, was used to simulate the lung to control blood oxygenation via gas blood exchange during experiment. The flow regulator1 and regulator2 were used to regulate flow volume in each vessel.

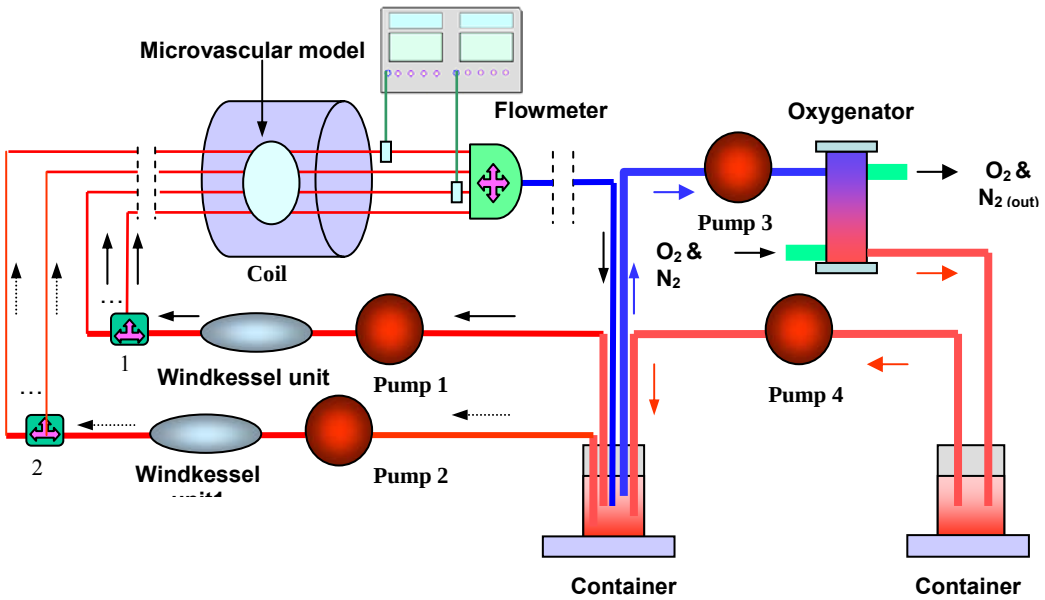

Figure 2.4 Diagram of the phantom system for experiment (ver1.0)

The pump1 and pump2 could separately control two vessel groups with different flow velocities. Pump3 was used to pump blood of container1 into oxygenator unit to finish blood oxygenation or de-oxygenation. Pump4 was to pump blood from container2 back to container1 in order to maintain the volume balance. Gases (air, N_2 and O_2) were used in the oxygenator to change circulatory blood oxygenation level.

The advantage of this version was that intra-systemic pressure and flow velocity in the vessel can be controlled at low levels. However, tests showed the flow in the vessels wasn't uniform although these vessels were controlled by a single pump. The blood viscosity caused different dynamic flow resistance. Therefore, the system model was modified (Figure 2.5).

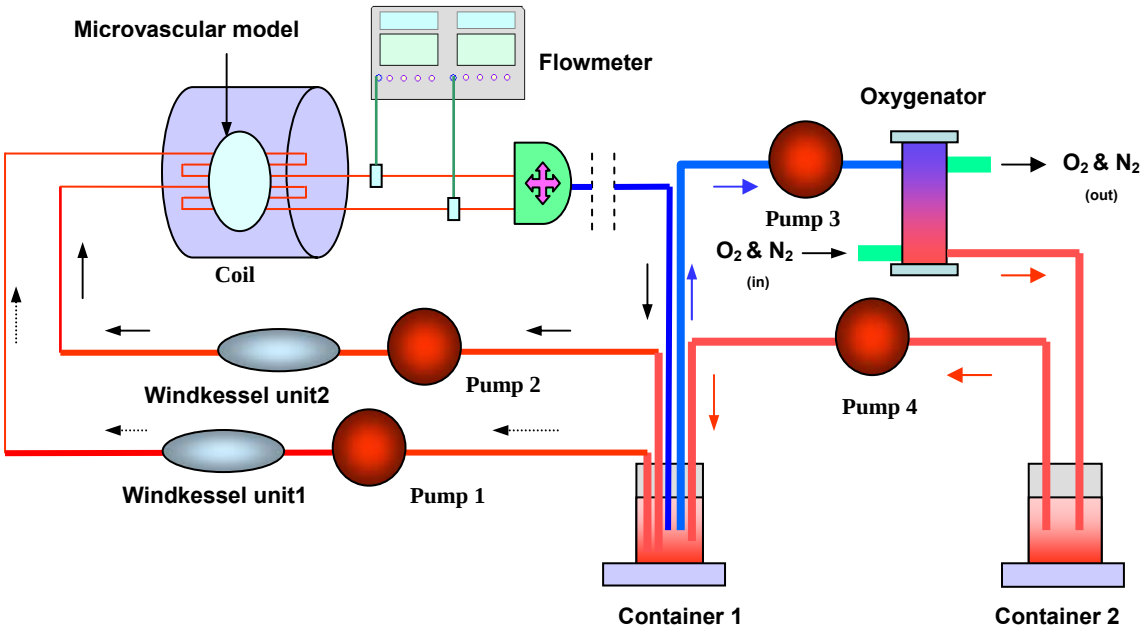

Figure 2.5 Diagram of the phantom system for experiment (ver2.0)

In the modified phantom system, two pumps controlled two vessel groups in the phantom without flow regulator. Vessels of a given group were connected serially in the system, guaranteeing a equal flow. However, the disadvantage was the working

pressure on the system was much higher because of resistance, potentially causing leakage. Fortunately, my phantom connectors worked perfectly.

2.3.2 Pumps

The pumps (MasterFlex® console drive model 7521-50) were used to control flow in vessel phantom (Figure 2.6). Two other pumps (MasterFlex® model 600) were used to pump blood from container1 to oxygenator and from container2 to container1.

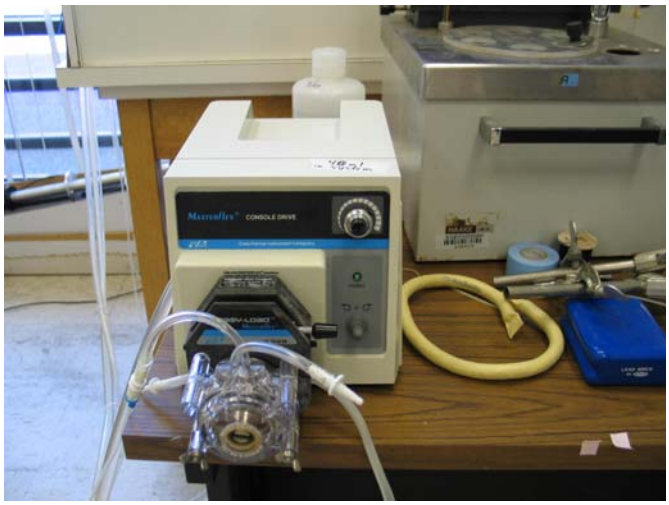

Figure 2.6 The pump of circulation phantom system

2.3.3 Oxygenator

The hollow fiber membranes were used to build my first version of oxygenator (Figure 2.7). The oxygenator was designed as a sealed unit, which simulated lungs to furnish exchange between gas and blood. It can control the blood oxygenation on the circulatory system. Gas (O_2, air) caused blood oxygenation increase (oxygenator), or decrease (N_2). An advantage of this design was no air-bubbles during operation. This

unit worked well as an oxygenator, but not as a deoxygenator. Thus, a second design used air bubbles (Figure 2.8).

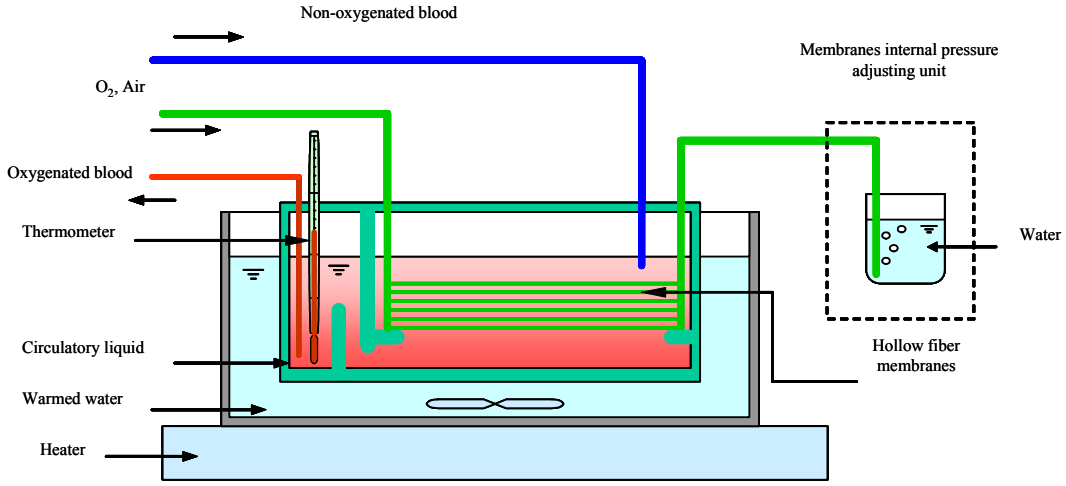

Figure 2.7 Diagram of the oxygenator (ver1.0)

The blood volume was about 1200 ml and the temperature of blood was room temperature (69°F). After testing, it took a few minutes to increase the blood oxygenation using O_2 gas (Figure 2.9). Deoxygenation was very ineffective requiring 19 hours to decrease 1200 ml blood with N_2 (Figure 2.10). Unfortunately, the red cells died due to the excessive time.

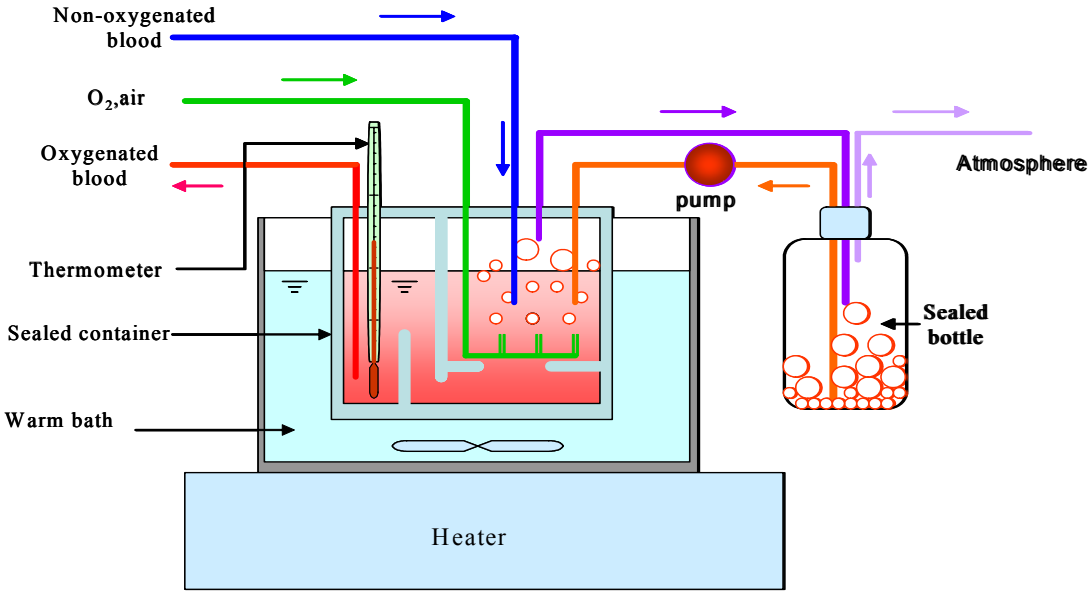

Figure 2.8 Diagram of the oxygenator (ver2.0)

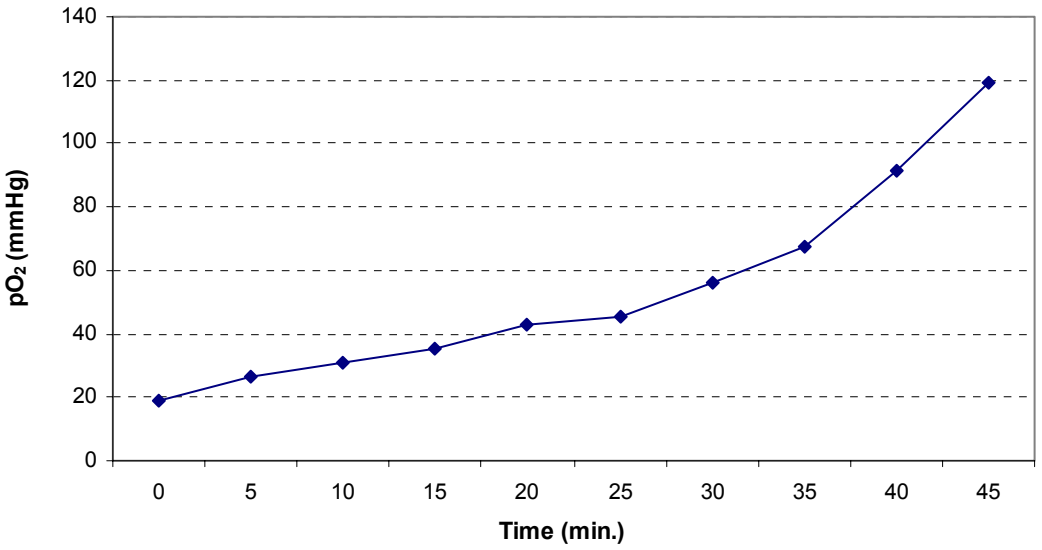

Figure 2.9 variation in blood oxygenation during oxygenation

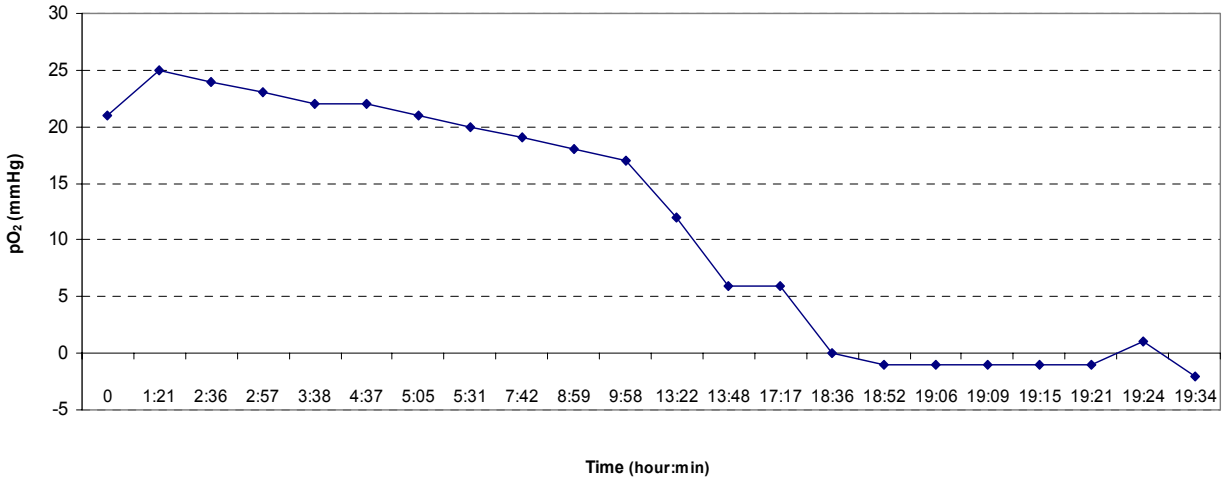

Figure 2.10 variation in blood during de-oxygenation

In my final phantom experiment, a commercial cardiovascular surgery oxygenator (AFFINITY®, Hollow Fiber Oxygenator) was used (Figure 2.11). Now both oxygenation and deoxygenation took only 30 min. with decrease in blood oxygenation to 10 mmHg. The disadvantage is the high cost of this oxygenator.

Figure 2.11 The commercial oxygenator
(AFFINITY®, Hollow Fiber Oxygenator)

2.3.4 Vessel model

Considering the image resolution, vessel number, diameter of coil, and fluid dynamic parameters, TEFLON tubing (1.19mm in diameter) was selected as vessel.

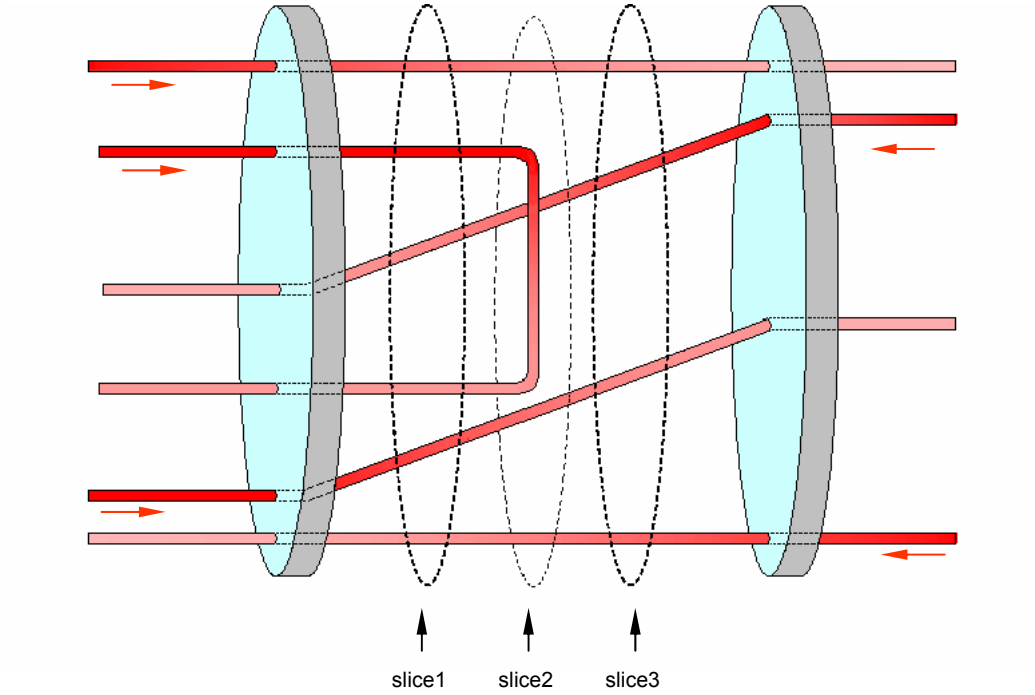

Figure 2.12 The microvessel model in MRI experiment

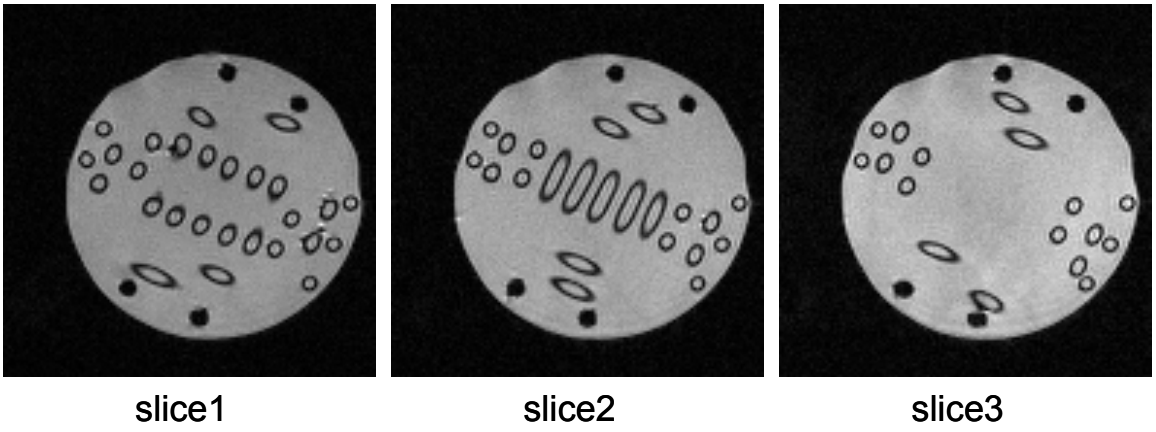

Figure 2.13. Three slices of microvessel model from MR imaging

(Spin Echo, TR/TE=900/12 ms, thickness=0.5 mm, Matrix=128×128, voxel size=0.39×0.39mm)

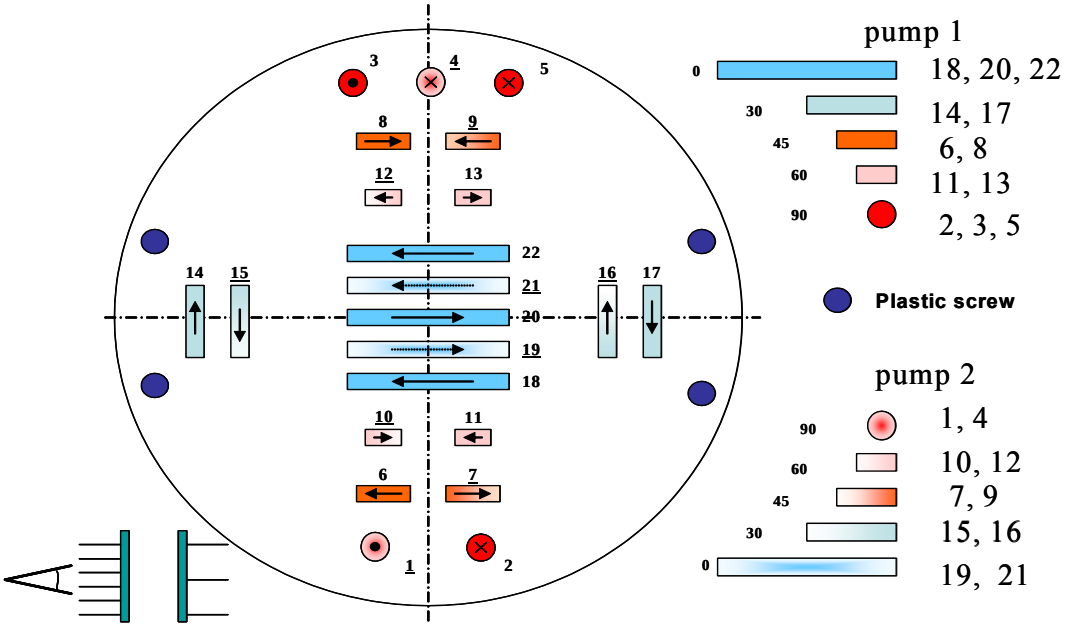

Figure 2.14 Diagram of the vessel code and flow in slice2
(Arrow shows the flow direction)

Generally, the vascular orientation and flow direction is random in tumor tissue. Considering that different orientations of vessels may cause different signal gain, I included specific angles 0 °, 30 °, 45 °, 60 °, and 90° for the vessels in phantom. Ideally, both flow directions should be included in the same angle vessel. The vessel

model consisted of twenty-two different angled “vessels”, which fitted in the MRI coil (Figure 2.12,13).

Each vessel in model was coded as number from 1 to 22 (Figure 2.14). All vessels were divided into two groups, which were controlled by two separate pumps in order to get different flow velocity during experiment (Figure 2.5).

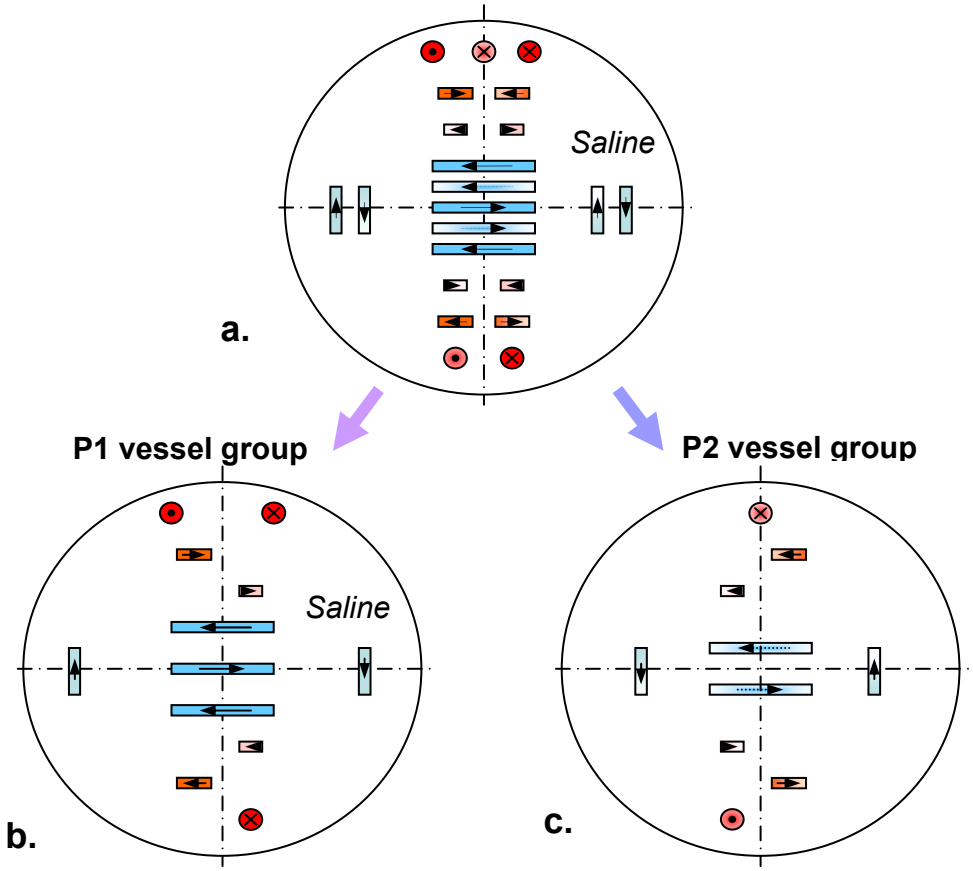

Figure 2.15 Diagrams of the vessels controlled by two pumps
a) all vessels; b) twelve vessels controlled by pump1; c) ten vessels controlled by pump2.

The vessel group which was controlled by each pump included all angles and flow directions (Figure 2.15). Pump1 controlled 12 vessels, which included angles of 0^{o}, 30^{o}, 45^{o}, 60^{o}, and 90^{o} with two flow directions, (P1 vessel group, Figure 2.15b); and pump2 controlled 10 vessels with different angle and flow direction, (P2 vessel

group, Figure 2.15c). All vessels were bathed in stationary saline (Figure.2.15a). Avoiding saline leakage was initially a problem. But finally, phantom could be continuously used over 24 hours without problem.

In my phantom experiment, the blood flow velocity was selected as 24 cm/s, 12 cm/s, 6 cm/s, and 0 cm/s. After calculating the R.N. in the vessel phantom (Blood viscosity =6.29 mPa.s , blood density=1.63 g/cm^3, diameter=1.19 mm.), the value was less than 2,000 providing Laminar flow (Table 2.2).

Table 2.2 the Reynold's number in vessels during phantom experiment

Flow velocity	0 cm/s	6 cm/s	12 cm/s	24 cm/s
Reynolds Number	0	15	30	60

2.4 Blood sample preparation

2.4.1 Blood sample collection

To prepare blood samples I used (CPDA-1) solution (Table. 2.3) as recommended by Dr. W Hang for human blood storage. All blood samples were collected from young cows (<3 years old). During collection, the heparinizing solution was mixed in a gallon container and saved at 4^{o}C .

Table 2.3. CPDA-1 composition

Glucose (g/L)	Sodium Citrate (g/L)	Citric Acid (g/L)	Sodium Phosphate (g/L)	Adenine (mg/L)	pH	Blood usage (ml/L)
25.5	26.3	3.27	2.22	346	5.63	140

All blood samples were purchased from Dallas Meat Company and I thank Mrs. JoAnn Dottie, Vela Gee and Mr. Rene R. Hernandez for help in sample collection.

2.4.2 Blood sample filter

Cleaned blood was required because of the small diameter of "vessels" in the phantom. Blood was pumped at low flow through a commercial filter (Fenwal® 20 μm) (Figure 2.16).

Figure 2.16 The filter for blood sample

2.4.3 Blood sample preparation

Usually blood was kept at room temperature for 1 hour before experiment and the oxygen partial pressure (pO_2) was 20~40 mmHg. Gases (100% N_2, or 100% O_2) were used to achieve different blood oxygenation in the phantom system (Figure 2.5). Although this circulation system was designed as a sealed system, the blood oxygenation on the system could change slightly. Normal parameters of human are shown in (Table 2.4).

Table 2.4 Typical human Blood Gas analysis (55)

parameters	Normal adult arterial	Normal adult venous
pH	7.35 ~ 7.45	7.31 ~ 7.41
pO_2	80 ~ 100 torr	35 ~ 40 torr
pCO_2	35 ~ 45 torr	41 ~ 51 torr
SaO_2	> 95 %	75 %

Reports indicate hypoxia in tumors with pO_2 lower than 10 mmHg (56). In my phantom, I used a range of blood oxygenation between 10 mmHg and 100 mmHg to simulate tumor hypoxia and oxygen inhalation *in vivo*. The long experimental time could cause the red cells to die, so I frequently replaced the "old blood" with fresh.

2.5 Blood flow Measurement

During phantom experiments, blood flow velocity was measured continuously. A Transonic® T201 2-channel ultransonic blood flow meter (Figure 2.17) with two measurement probes (2RB887 and 2RB615) (Figure 2.18) was used to monitor blood flow on-line.

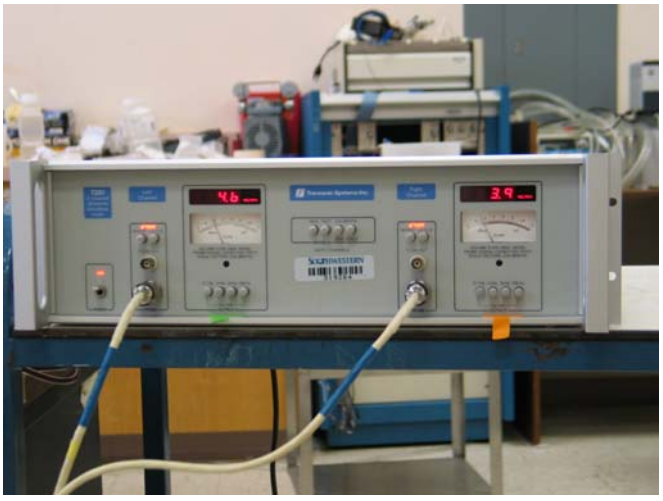

Figure 2.17 The two channel Transonic® Flowmeter

Figure 2.18 The flow probes

2.6 Blood oxygenation measurement

The partial pressure of blood sample (0.4 ml each) was measured using an Instrumentation Laboratory® pH/Blood Gas Analyzer (Figure 2.19).

Figure 2.19 The Laboratory® Blood Gas Analyzer

2.7 The hematocrit measurement

The value of hematocrit of blood sample is very important to the BOLD study because it could directly affect the blood oxygenation capability. The BOLD signal is sensitive to the change of deoxyhemoglobin concentration in the blood. If the concentration of red cells in blood increased or decreased, it could directly affect the BOLD response. I found the concentration of red cells in blood samples from several cows was about 50% and I did not vary this value.

Hematocrit was measured using:

Micro-hematocrit tube: Drummond® 75mm Hematocrit tube (Figure 2.20)

Centrifuge: DAMON®, IEC MB Centrifuge (Figure 2.21)

Hematocrit reader: SPIRACRIT® Micro-hematocrit reader (Figure 2.22)

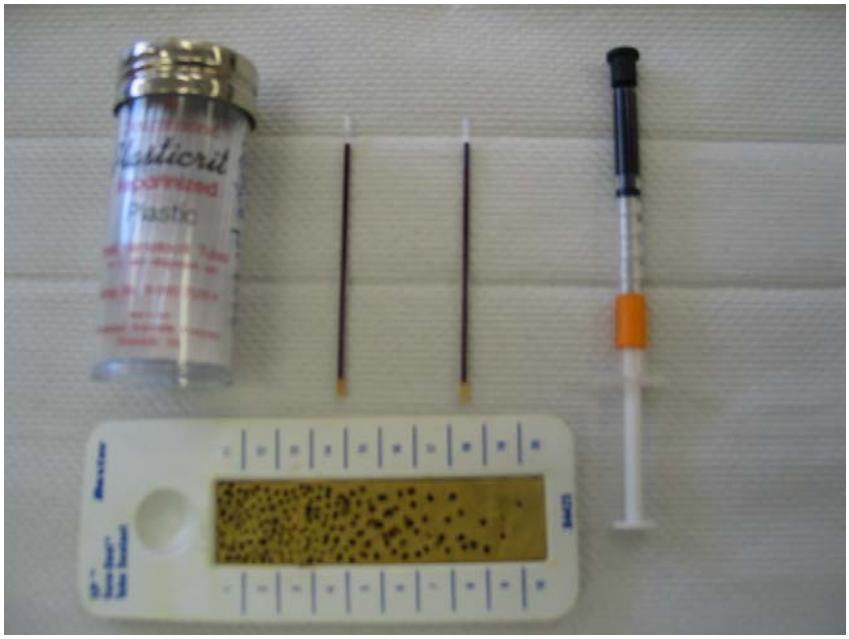

Figure 2.20 The preparation for hematocrit measurement

Figure 2.21 The centrifuge for hematocrit tube

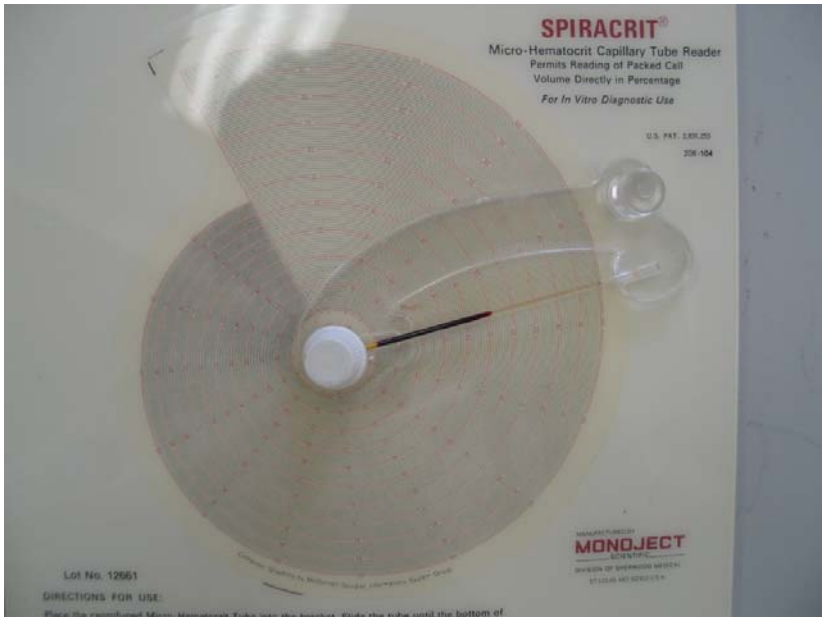

Figure 2.22 The micro-hematocrit tube reader

CHAPTER 3

PHANTOM EXPERIMENT

3.1 Introduction

The previous chapter described the phantom design and implementation for *in vitro* study. This chapter is focused on experiments exploring the relationship between BOLD signal change and variation in blood flow and oxygenation. The BOLD phenomenon involves complex changes in blood volume, blood flow, and deoxyhemoglobin level, that results in altered signal intensity in T2* or T2–weighted MR images. Previous studies also showed that BOLD signal is related to deoxyhemoglobin concentration and magnetic field strength (57). The strength of the static magnetic field (B_0) is an important factor in determining the magnitude of the signal change (58). This is because the Bulk Magnetic Susceptibility (BMS) difference between blood containing paramagnetic deoxyhemoglobin and surrounding diamagnetic tissue increase with main magnetic field strength, creating larger MR signal changes between baseline and activated state. Changes of oxygenation of blood could cause different T2* values (20,21).

The phantom experiment had three aims: i) to measure the T2, T2*, and T1 variation between low and high blood oxygenation level at 4.7T, ii) to explore BOLD signal response to variation in blood flow at constant, blood oxygenation, iii) to explore BOLD signal response to the change of blood oxygenation when the blood flow was constant.

3.2 Measurement of T2* values with different blood oxygenation

3.2.1 Materials and methods

Blood sample

About 40 ml bovine blood was put in a 50 ml polypropylene tube at ambient temperature (69^{o}F) for 30 minutes, and bubbled for 30 minutes with N_2 reducing the oxygen partial pressure (pO_2) from 30 mmHg to 4 mmHg. Air was used to generate samples with pO_2 in the range of 4 mm Hg to 148 mmHg in 5 ml plastic tubes capped and sealed with parafilm. For T2 measurement, blood samples had pO_2= 4, 72, 100, and 148 mmHg, T1 measurements were performed on separate blood samples had pO_2 =12, 70, and 139 mmHg.

MRI experiment

MR experiments were performed using a 4.7 T horizontal bore system with actively shielded gradients (Varian) with a ^{1}H single turn solenoid coil (3 cm in diameter). The special pulse sequence CPMGT2 (Carr-Purcell Meiboom-Gill T2, TR=6s) was used to separately measure the T2 value in each sample. In addition, five differently oxygenated samples (4, 72, 100 and 148 mmHg) were placed in the coil together. A FLASH sequence (TR=400 ms, TE=4, 6, 8, 16, 32, 64, 128, 256 ms, matrix=128×128, flip angle=20^{o}, FOV=45×45 mm) was used to measure blood T2* value.

For T1 measurement, three blood samples with different oxygen level (12, 70, and 139 mmHg) were placed together in the ^{1}H coil. FLASH sequence (TR=10, 12, 15, 18, 20, 25, 30, 40, 60, 80, 100, 500, and 1000 ms, TE=6 ms, matrix=128×128, flip angle=90^{o}, FOV=50×50 mm) was used to measure the T1 values.

Data analysis

The Varian browser (VNMR 6.1c) and SigmaPlot 2000 were used for data fitting. The T2 and T2* fitting was based on:

$$Y = A \cdot \lambda^{-\frac{x}{T_2^*}} \qquad (3\text{-}1)$$

where, Y is the observed MRI signal, x is the echo time, and A is the equilibrium magnetization.

The T1 fitting was based on

$$Y = (M_0 - M) \cdot \lambda^{-\frac{x}{T_1}} \qquad (3\text{-}2)$$

Where, Y is the observed MRI signal, x is the repetition time, M is the magnetization.

3.2.2 Results

The (CPMG-T2) pulse sequence was used to measure the T2 value of each sample. The Varian software (VNMR 6.1c) was used to process original data (Figure 3.1). It showed the increase in T2 value with higher sample oxygenation. The T2* measurement showed positive correlation with oxygenation level (Figure 3.2). The fitting results of T2 and T2* are shown in Table 3.1. The range of the experimental oxygenation could be selected between 4 and 100 mmHg.

The T1 measurement showed that the T1 values of different oxygenation samples had little change (Table 3.2, Figure 3.3).

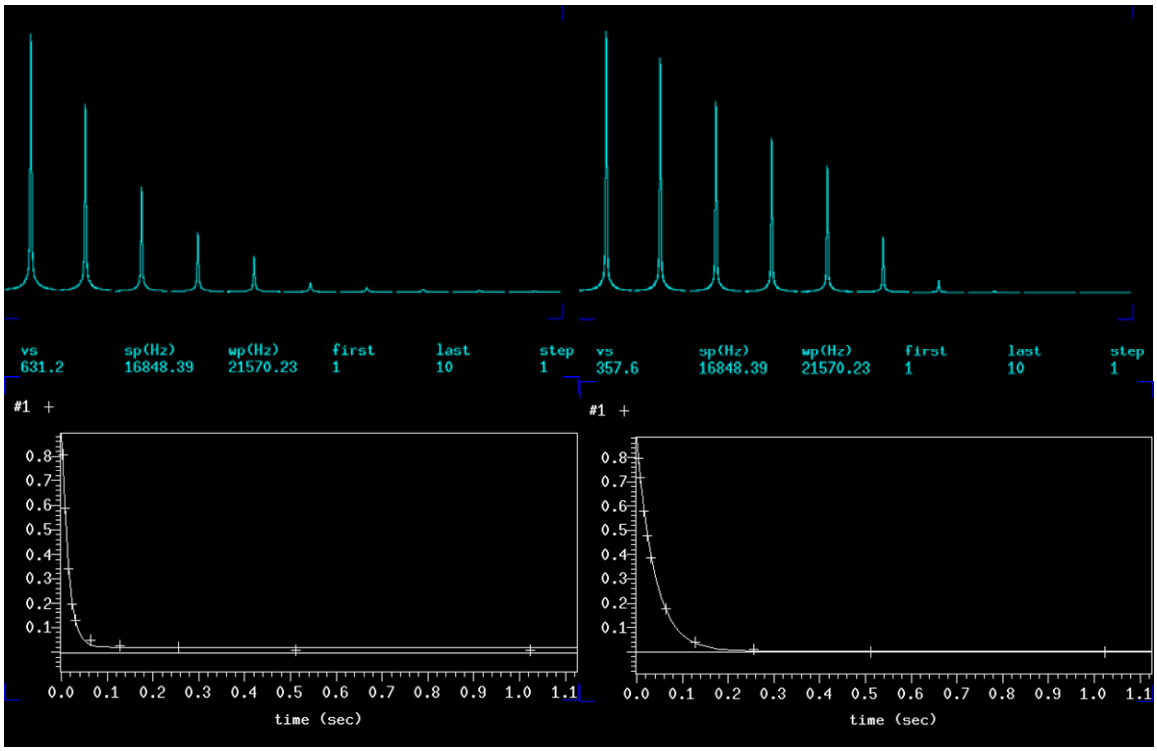

pO_2=4 mmHg pO_2=72 mmHg

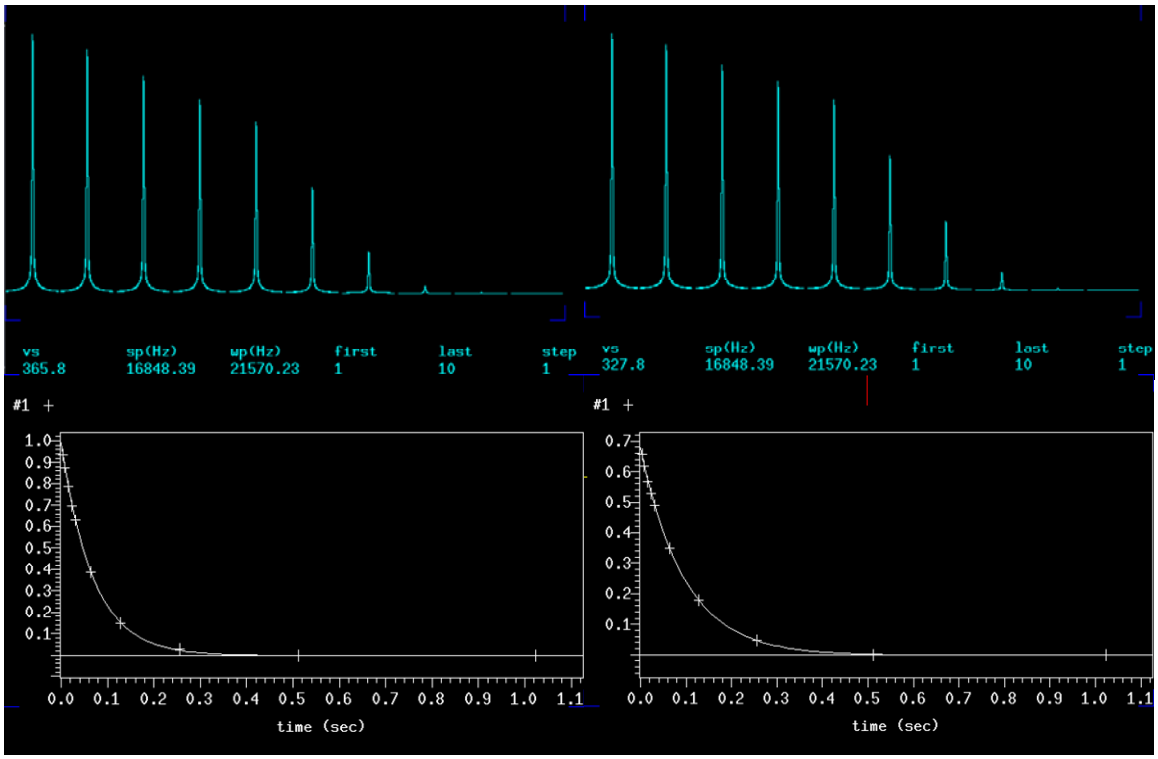

pO_2=100 mmHg pO_2=148 mmHg

Figure 3.1 T2 measurement using CPMG-T2

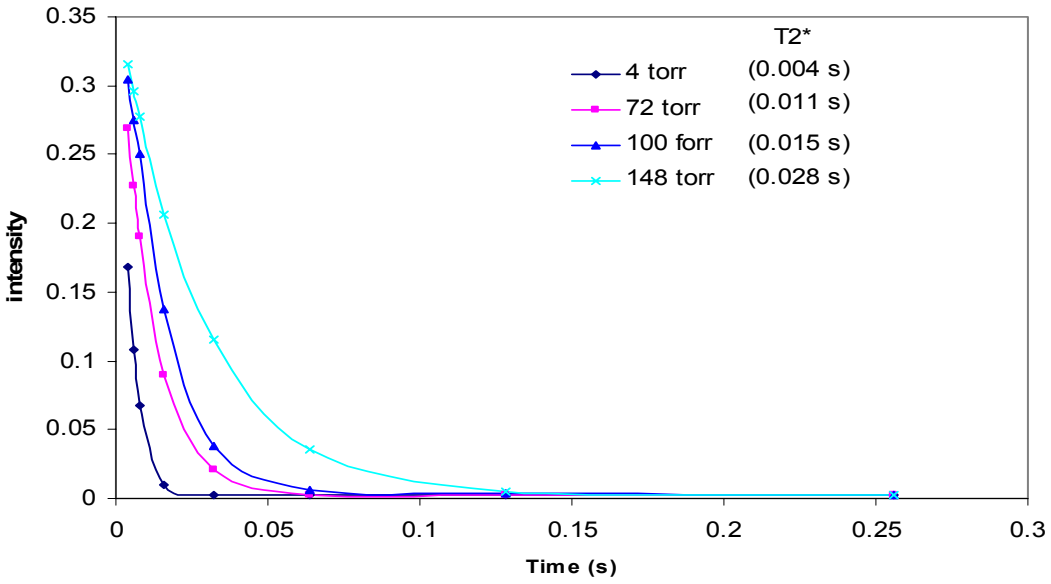

Figure 3.2 T2* fitting result

Table 3.1. T2 and T2* of different blood oxygenation sample

	T2 (s)	T2* (s)
4 mmHg	0.014±0.0004	0.004±0.0001
72 mmHg	0.039±0.0005	0.011±0.0002
100 mmHg	0.069±0.0008	0.015±0.0008
148 mmHg	0.096±0.0015	0.028±0.0003

Table 3.2. T1 values at different oxygenations

Blood oxygenation	T1 (s)
12 mmHg	0.1016 ± 0.0203
70 mmHg	0.1178 ± 0.0078
139 mmHg	0.1009 ± 0.0078

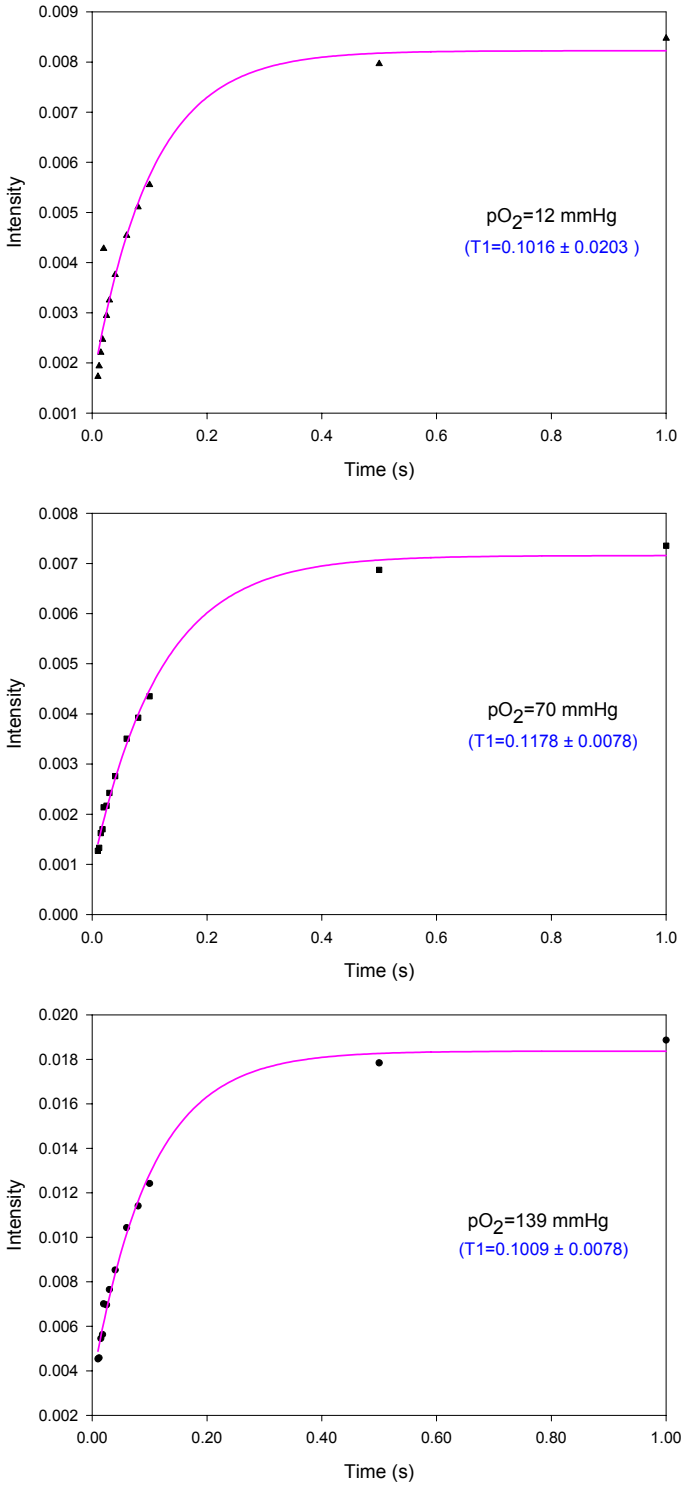

Figure 3.3 T1 fitting result for three blood samples

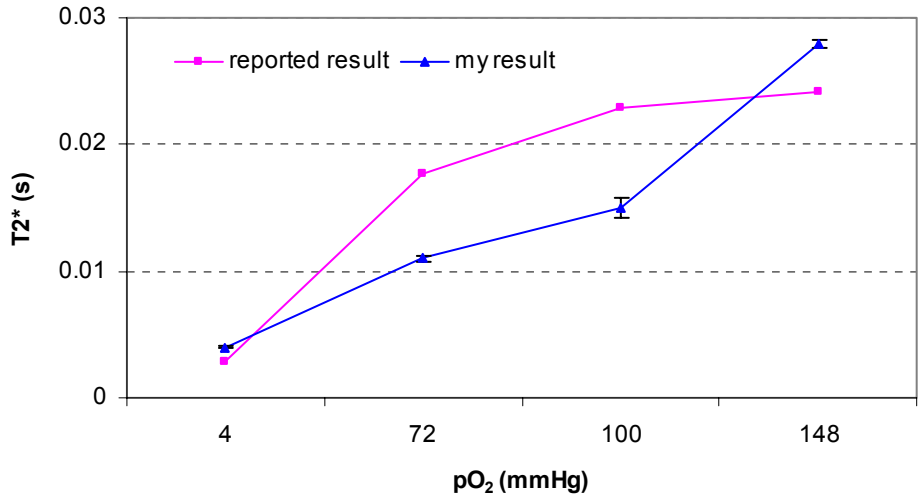

Figure 3.4 Comparison of my T2* values and published results at 4.7T (57)

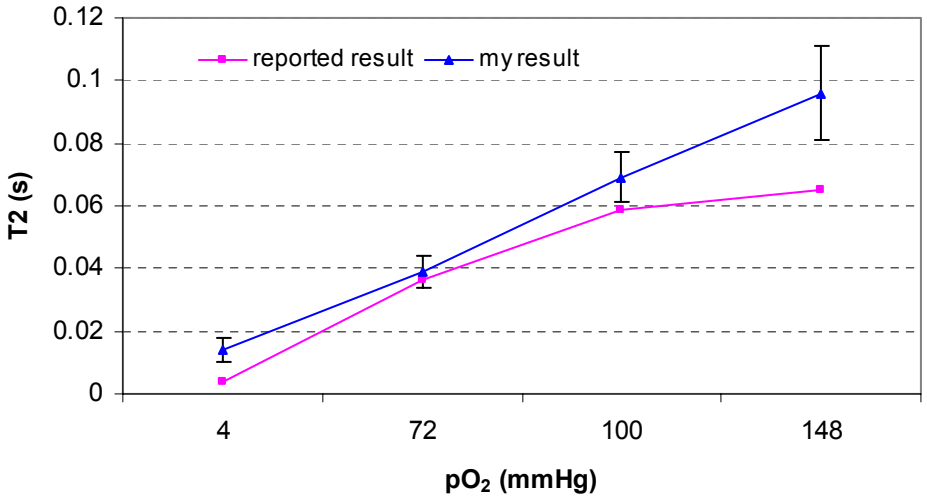

Figure 3.5 Comparison of my T2 results and published results at 4.7T (57)

Using published fitting equation, comparison of my results and published results are shown in Figure 3.4 and 3.5. Blood T2* value shows a significant field dependence (Figure 3.6). When magnetic field strength increased, the T2* value at the same oxygenation decreased.

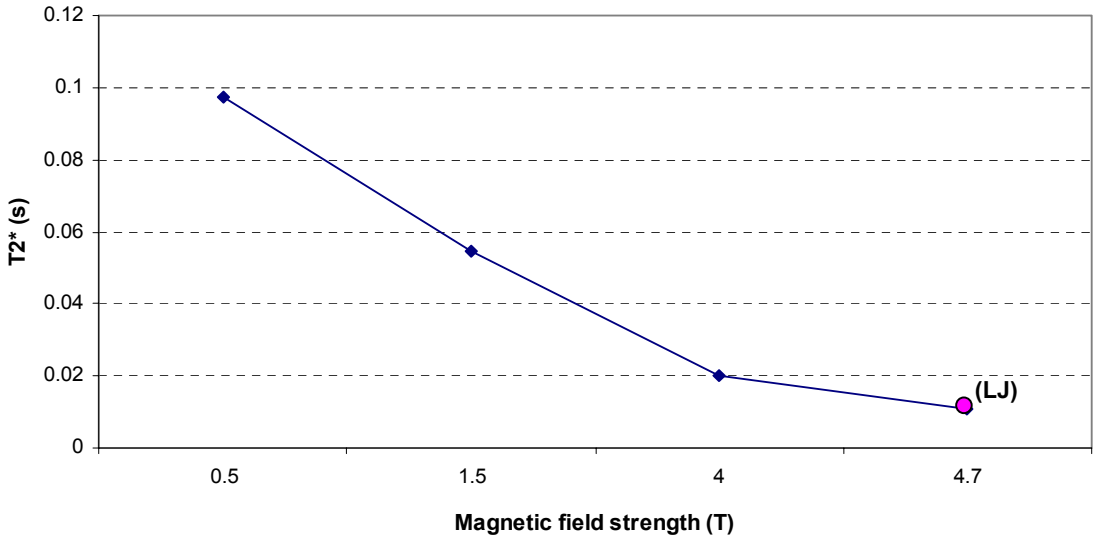

Figure 3.6 Comparison of published T2* *in vivo* and my *in vitro* results (58)

3.2.3 Discussion

T2 variation with blood oxygenation was reported by Ogawa in 1990 (21). This is the foundation of functional MRI in neuroscience and the foundation for BOLD MRI for exploring tumor physiology. T2 and T2* values decrease as magnetic field strength increases (57,58). My results show that T2 and T2* increase as pO_2 increases (Table 3.1). The difference between T2 and T2* in the same oxygenation sample arise from inhomogeneities in the main magnetic field. The results are comparable to the results reported published at 4.7T (Figure 3.4 and 5) (57). My measurements showed that the longitudinal relaxation time (T1) was almost constant for varying oxygenation (Table 3.2), as also reported by other (59). However, it has been reported that T1 of blood does vary with pO_2 when it is greater than 20% (higher than 138 mmHg) (60).

Based on my results, I chose the following experimental parameters TE=10 ms in order to get maximum T2* effect during BOLD imaging, and TR=200 ms.

3.3 BOLD signal related to blood flow variation

3.3.1 Material and methods

1800 ml blood was filtered using the whole blood filter (Fenwal® 20 μm) and allowed to equilibrate for one hour at room temperature (Figure 2.5). Two sets of flow variation were investigated.

1) Simple flow variation. The blood flow in the vessels was separately controlled by pump1 and pump2. First, the flow velocity of all vessels was controlled at 12 cm/s and MRI performed to measure five points as the baseline. By adjusting pump1 or pump2, the blood flow in some vessels was increase to 24 cm/s or decreased to 6 cm/s respectively, and MRI performed three times. Finally, MRI was repeated two times when the velocities returned to baseline (12 cm/s). Each velocity variation experiment was repeated one time (Figure 3.7).

2) Perfusion regulation. Baseline measurement was as above. By adjusting both pump1 and pump2, the blood flow in some vessels was increased to 24 cm/s while others were decreased to 6 cm/s. MRI was performed thrice. Finally, MRI was performed twice when the velocities in the vessels were back to baseline (12 cm/s). Each velocity variation experiment must be repeated one time (Figure 3.7).

Calculation of Reynold's number indicated that there was no turbulent flow in the vessels at these flow velocities (Table 2.3). A Transonic® Flowmeter (model

T210) with two measurement probes was used to monitor blood flow in-line in real time.

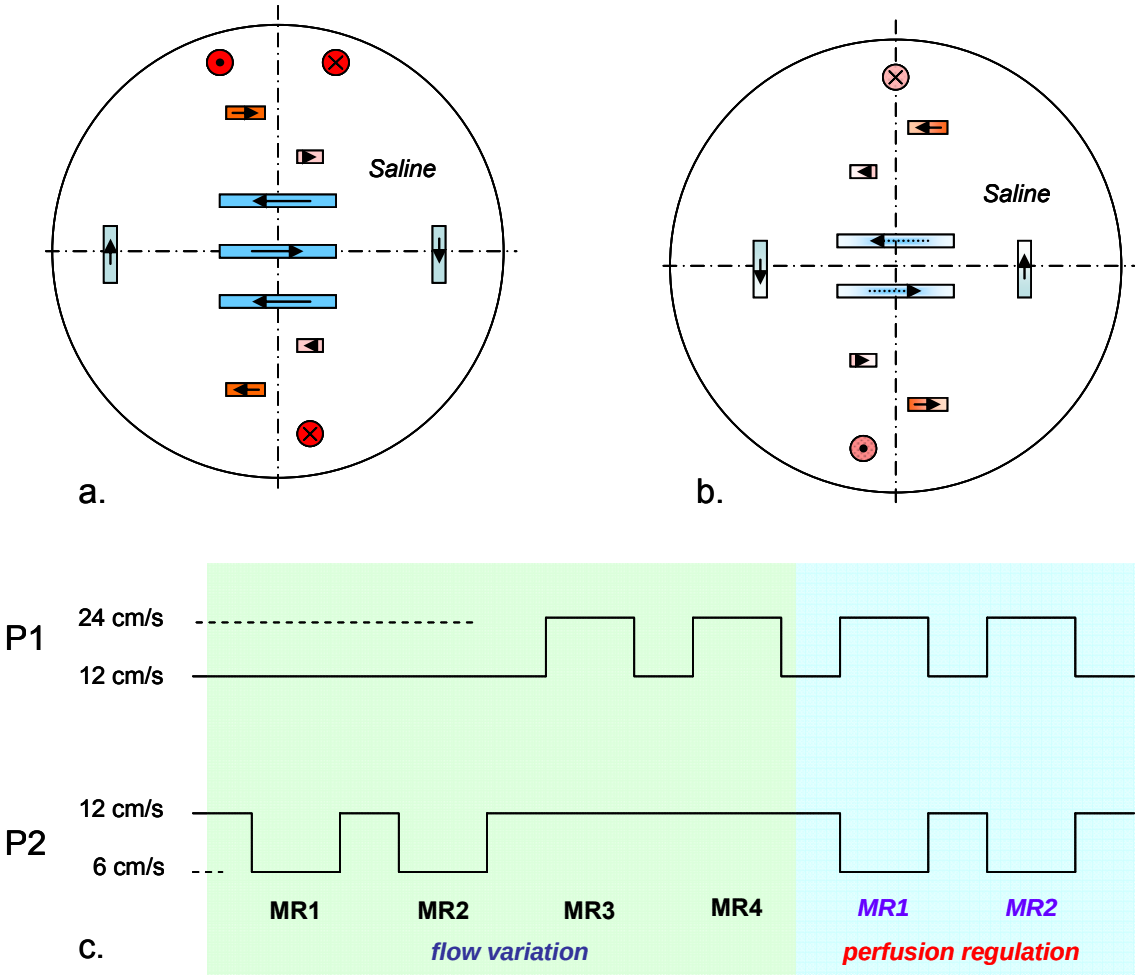

Figure 3.7 the protocol of different flow velocity in vessels.
a) and b) show different vessels controlled by pump1 and 2. c) shows velocities set up by pump1 (P1) and pump2 (P2). Each velocity setting was repeated.

Blood oxygenation was monitored throughout the experiment. While it was expected to remain constant, oxygenation could increase slight because of blood gas exchange on the surface of container1 (Figure 2.5).

Magnetic Resonance Imaging

MR experiments were performed using a 4.7 T horizontal bore system with actively shielded gradients (Varian). The "vessel" phantom was placed in a size-matched ^{1}H single turn solenoid coil (3 cm in diameter), and the volume around the vessels was filled with saline (Figure 3.7a,b). The phantom was kept as room temperature. The FLASH (Fast low angle shot) technique was used in my BOLD study (TR=200 ms, TE=10 ms, flip angle=45^{o}, thickness=1mm, Matrix=128×128, FOV=50×50 mm). For each MRI point, the phase coding direction was swapped and imaged twice in order to minimize possible artifact from the encoding direction (Figure 3.8).

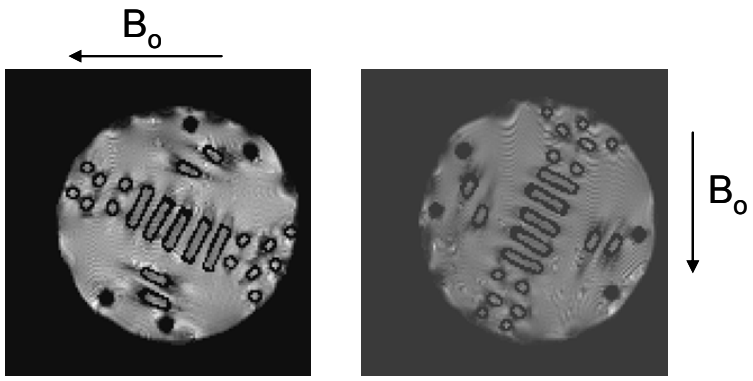

Figure 3.8. The MRI image with different encoding direction

Data analysis

Data analysis was on voxel-by-voxel basis. Since the different vascular orientation with respect to B_0 may cause different BOLD signal gain during experiment, the data processing had two parts. Part one focused on comparison with each angled vessel response to the flow variation. The signal intensity and relative signal intensity of each angled vessel were analyzed. Part two was based on the two vessel groups, including all angles matching the *in vivo* situation. The protocol of each vessel group is shown in Figure 3.7.

The extra-vessel region was also analyzed (Figure 3.9). The same region in different phase encoding images was processed and presented as the mean value in this region during analysis.

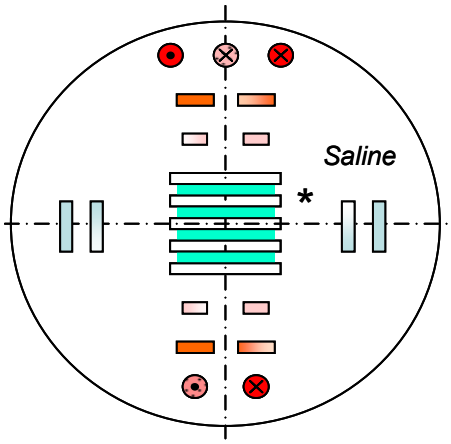

Figure 3.9 the extra-vessel region in vessel model
(marked * region)

The relative signal intensity (ΔSI) of each voxel was analyzed using the equation:

$$(\Delta SI) = \frac{(SI_E - SI_b)}{SI_b} \times 100\% \qquad (3\text{-}3)$$

Where SI_E refers to the enhanced signal intensity in the voxel and SI_b is defined as the average of the baseline images.

3.3.2 Results

1. Aalysis of vessel angle

Original images of the vessels are shown in Figure 3.10, with the control baseline images (flow velocity =12 cm/s, left), changed blood flow (velocity =6

cm/s, middle), and recovery with flow back to control (right). The results show the change of signal intensity of each vessel angle depended upon angle of the vessel. The perpendicular (90^o) vessels had the highest signal intensity and changes were reversible upon return to baseline (Figure 3.11).

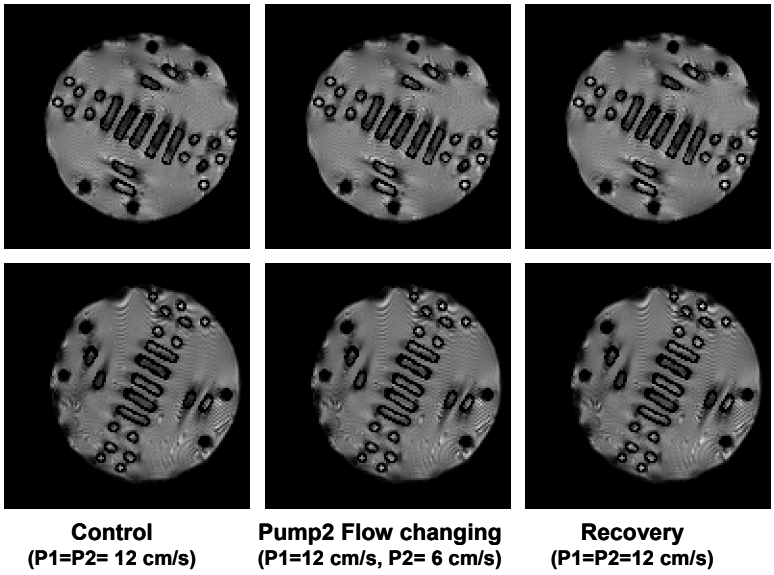

Figure 3.10 the MRI images of vessel phantom with flow variation. Top and bottom showed the image with swapped phase code direction.

The 90^o angled vessel showed the minimum SI variation with flow variation (Figure 3.12). The angles from 0^o to 45^o showed the highest variation. The signal was quite stable for all angles (<10% variation) for constant flow (Figure 3.12). The increase was caused by slight shift in blood oxygenation during the experiment (Figure 3.13c)

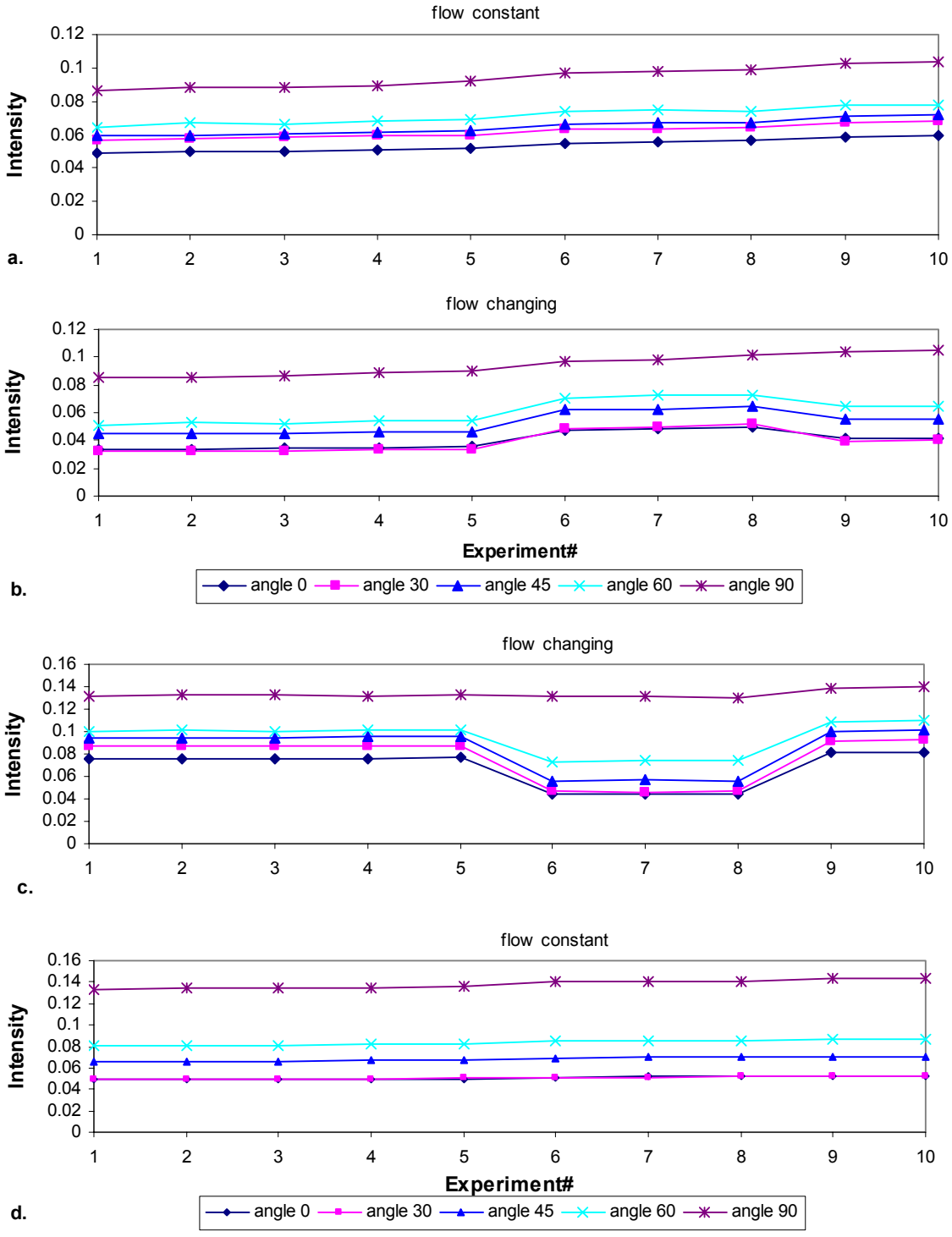

Figure 3.11 The T2* weight image signal of different angled vessels for constant pO_2. a , d.) show constant flow. b.) shows signal intensity when flow was decreased. c.) shows signal intensity when flow was increased.

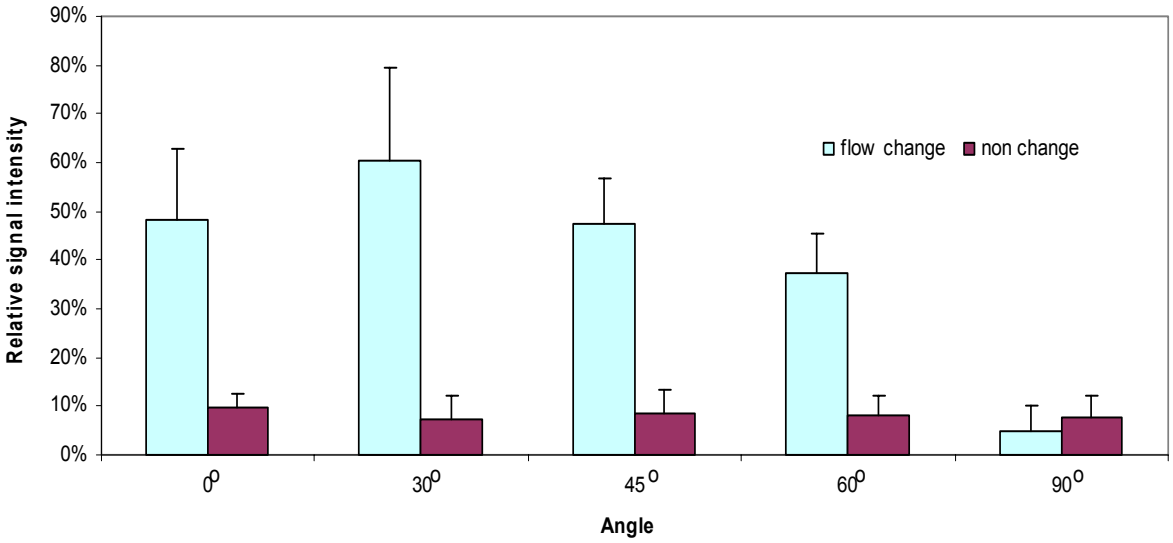

Figure 3.12 Relative signal intensity relative to vessel angle in response to flow variation

2. Vessel group analysis

Since blood vessels have multiple angles in tissues and they are so small in tissue that all angles will be averaged together. I analyzed average data ignoring angle (Figure 3.13). In my phantom experiment, the signal intensity decreased, while flow velocity increased; and the signal intensity increased, while flow velocity decreased. The phenomenon is related to rapid flow velocity as the baseline (12 cm/s) (52,61,62). The Figure 3.14 illustrates one of experiment.

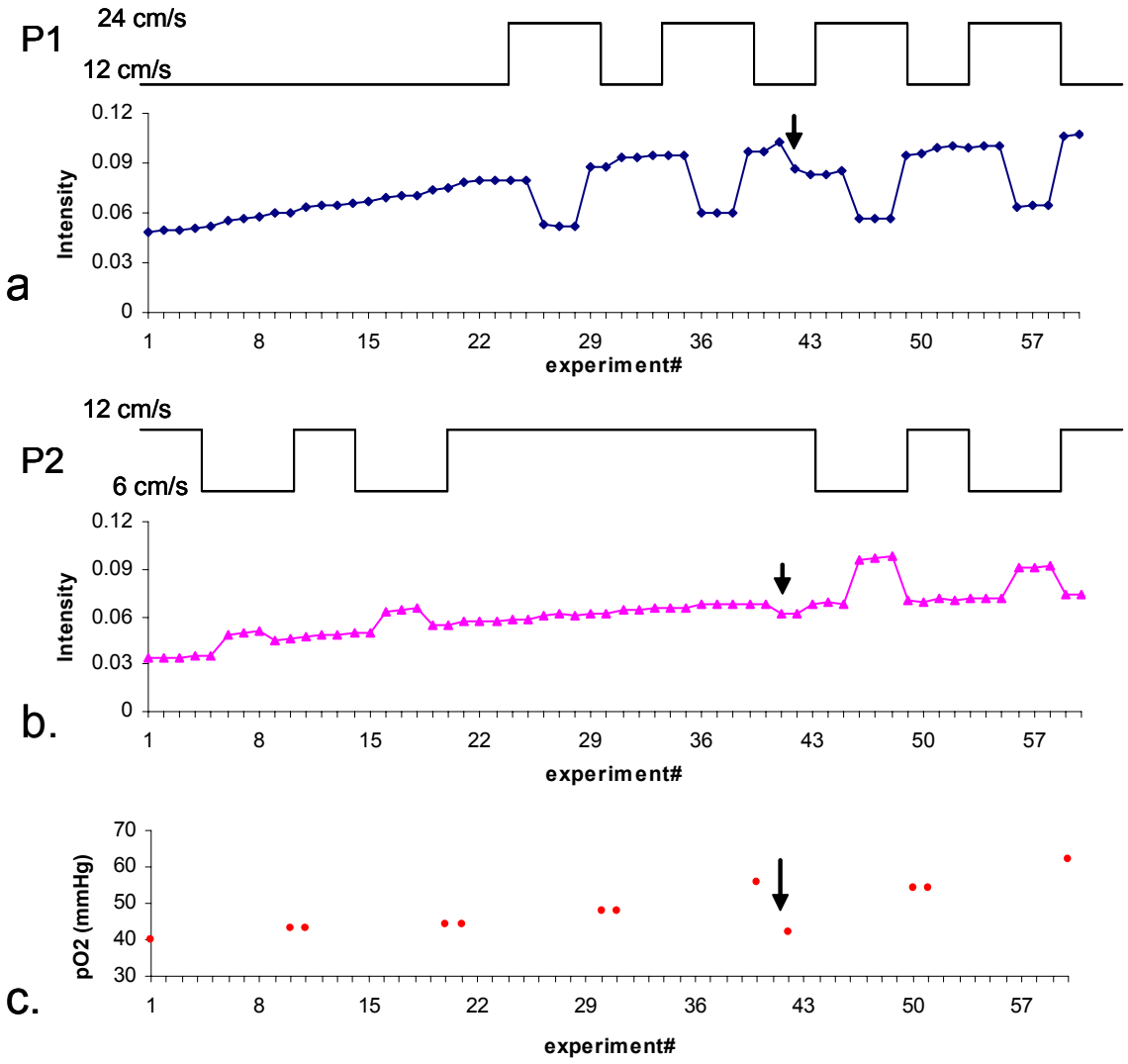

Figure 3.13 Dynamic response to the flow variation in two vascular groups.
a) and b) show the dynamic intra-vessel signal change of during pump1 or/and pump2 change. c) shows the blood oxygen partial pressure variation during experiment. The arrow shows when the partial pressure of blood was adjusted.

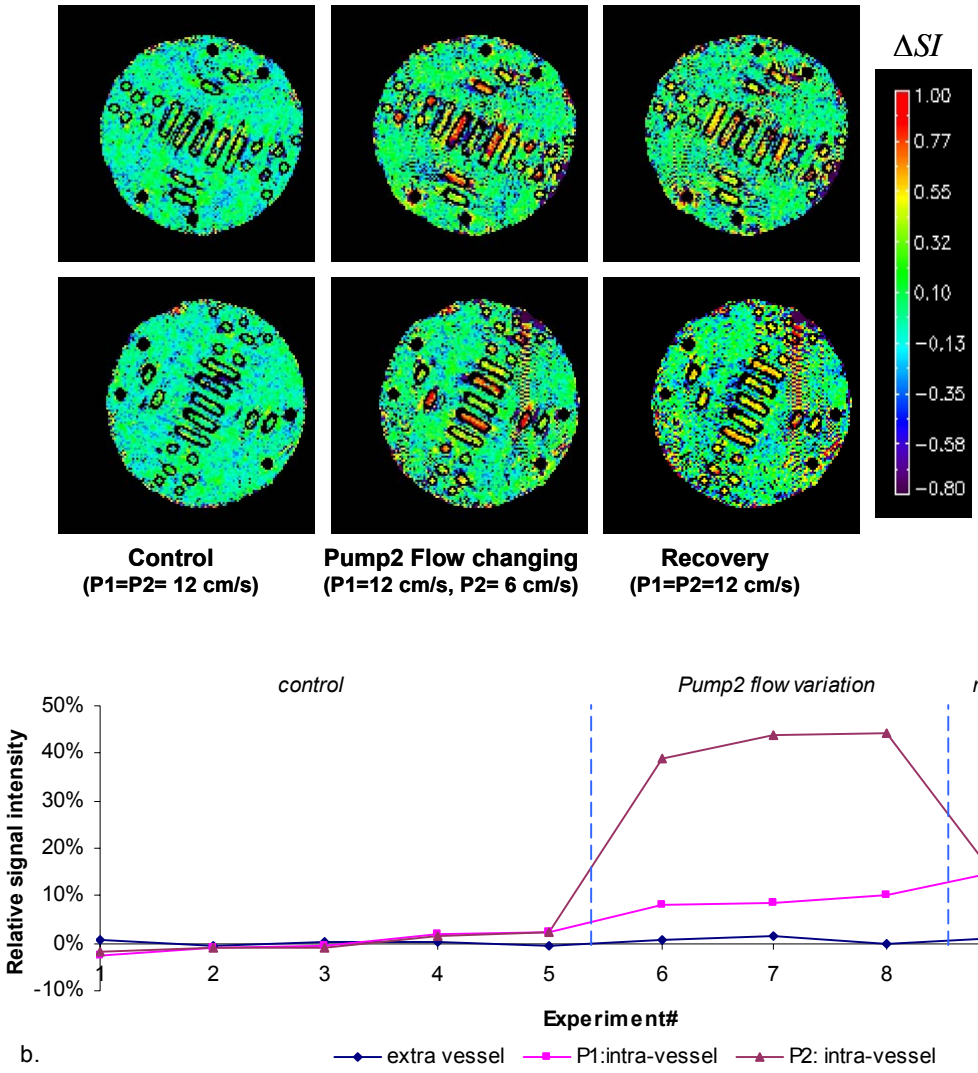

Figure 3.14, The BOLD response contour map and curves for different regions. a) shows the different phase encoding MR imaging between control, intervention and recovery period. b) shows the time curve of different intra-vessel region which controlled by two different pumps.

Overall, increase of blood flow velocity from 12 cm/s to 24 cm/s caused the BOLD signal to decrease about ~40%, while decreasing from 12 cm/s to 6 cm/s caused the BOLD signal to increase ~50%. The BOLD signal was quite stable for constant flow. The signal in the recovery period was a slightly higher than the

baseline, because the blood oxygenation continuously drifted upward (Figure 3.13,15).

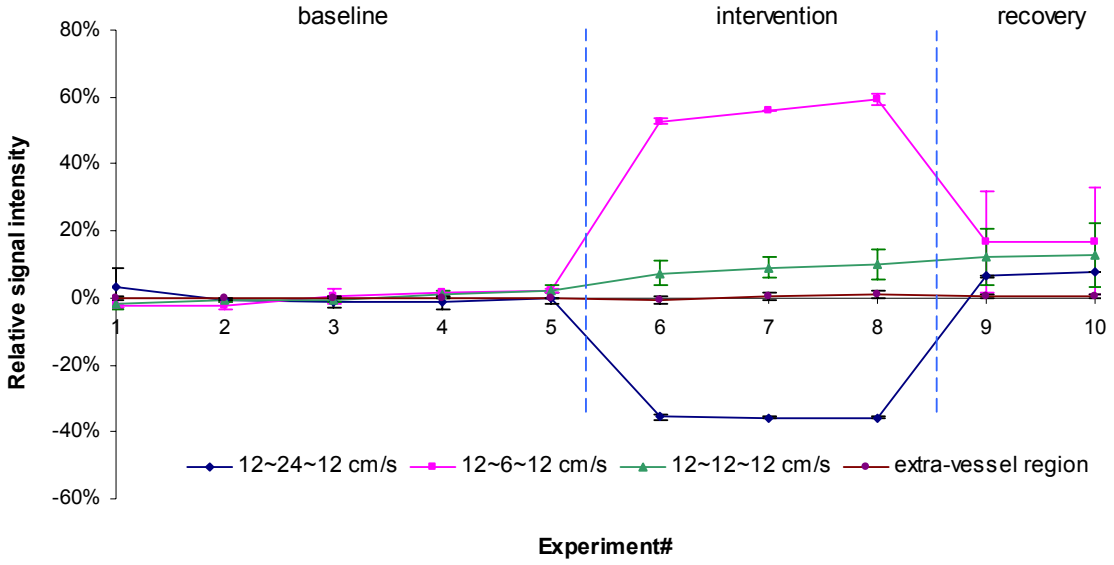

Figure 3.15 The BOLD signal in intra-vessels response to the flow variation

In my phantom study, analysis of (P1 vessel group) and (P2 vessel group) separately showed increase and decrease respectively of approximately 40% signal change (Figure 3.16). If all vessels were counted together as one ROI (Region of Interest), the mean relative signal intensity in all vessels only showed a small enhancement (Figure 3.16). The enhancement was almost the same as the non-flow variation in Figure 3.14, showing that counter acting effect can lead to non-enhancement.

3.3.3 Discussion

The BOLD signal is sensitive to the change of deoxyhemoglobin concentration and the blood flow in the vessel. This study focused on the flow variation effect only.

As we know, the Gradient Echo (GRE) imaging technique can measure BOLD signal via T2* weighted images. The signal intensity (SI) from a gradient recalled echo sequence is given by:

$$SI = S_o \cdot \sin(\alpha) \cdot \exp\left(-\frac{TE}{T_2^*}\right)$$

where, S_0 is proportional to the proton density, α is the flip angle, and TE is the echo time.

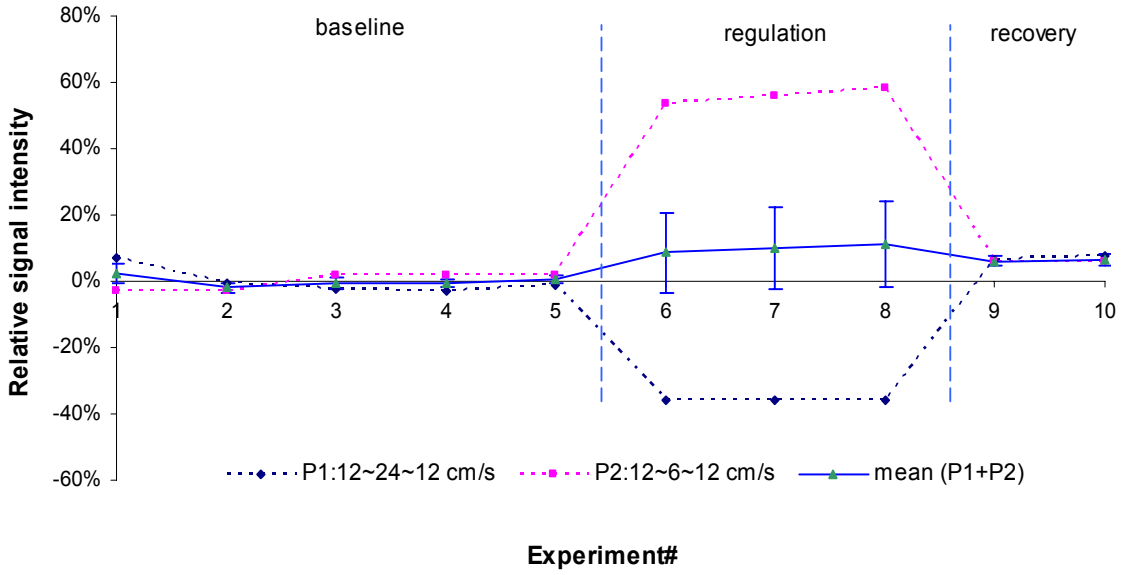

Figure 3.16 The BOLD response due to flow regulation.
The dotted lines were P1 and P2 groups; the blue line was the mean of P1 and P2.

The relations for GRE are further complicated by the short repetition time (TR) and high flip angle (30^o~90^o) making it sensitive to flow in the vessel. The water in blood flowing into the imaging slice produces a changed signal from water in static tissue. The spins in the static tissue will have been partially saturated by previous radiofrequency pulses. There is a signal variation that is generally known as the "in-

flow effect". The steady state signal intensity from a gradient recalled echo sequence is given more generally by:

$$SI = S_o \cdot \sin(\alpha) \cdot \exp\left(-\frac{TE}{T_2^*}\right) \cdot \frac{\left(1-\exp(-\frac{TR}{T_1})\right)}{\left(1-\cos(\alpha)\cdot\exp(-\frac{TR}{T_1})\right)}$$

where, So is proportional to the proton density, α is the flip angle, TE is the echo time and TR is the repetition time. T1 is the apparent longitudinal relaxation time. However, the orientation of each vessel also caused the different signal response during flow variation.

By separately analyzing each angle vessel, my results showed that the different angle vessels with B_0 caused different "in-flow effect" although the flow was equal to all vessels. The signal intensity of 90^o angle vessels showed the highest effect (Figure 3.11), while the 90^o angle vessels showed minimum "in-flow effect" (Figure 3.12). It demonstrated that the "in-flow effect" is also vessel orientation dependent.

However, it is impossible to distinguish every vascular angle during *in vivo* BOLD study. The vascular number and orientation are unknown and random during *in vivo* study. The strategy of analyzing vascular group, which included five different representative angles (0^o, 30^o, 45^o, 60^o, and 90^o) and two flow directions in these vessels could be closer to the *in vivo* situation. My results showed that the relative signal intensity in the intra-vessel could change 40~50% when blood flow velocity increased or decreased (Figure 3.15).

My results show there was no change in extra-vessel region during blood flow variation (Figure 3.14). The technical factors affecting the appearance of the flowing

blood include the type of pulse sequence, repetition time (TR), echo time (TE), flip angle (α). The use of flow compensation, saturation pulses, and cardiac gating also has profound effects. There are many MRI studies for flow vessel imaging, so called MRA (Magnetic Resonance Angiograph). However, to emphasize the importance of "in-flow effect", the term FLOOD (FLOw and Oxygenation Dependent) contrast MRI has been used (50).

There are several techniques available to distinguish the contribution from the in-flow and blood oxygenation to the BOLD signals. The in-flow effects can be eliminated by using low flip angle, centrally ordered k-space trajectories, or inter-image delays. And the multiple gradient-echo imaging sequences can be used instead of using conventional gradient-echo techniques.

Although the flow volume in the organ generally is constant, based on the flow regulation property *in vivo*, the blood flow in some microvessels of the region might increase, while the flow in other microvessels of the same region might decrease. My results show that BOLD signal change could be caused by flow variation. Can normal perfusion regulation affect the BOLD measurement? The answer depends on the data processing strategy.

The analysis of BOLD response couldn't be based on single or several voxels because it could be easily affected by flow regulation. Here, although the data processing was voxel-by-voxel, the analysis focuses on studying the BOLD response in ROI. From my previous *in vivo* BOLD study, when animals breathed air, the whole tumor showed <2% BOLD variation, breathing oxygen generated a 20% enhancement due to breathing oxygen (63). Further analysis showed the some voxels

had big positive enhancement, while some voxels had big negative change during air breathing.

The local oxygenation level depends upon the oxygen consumption of cells and the oxygen transport (microcirculation). The change of blood flow must affect the local oxygenation level. My results could be only one special situation where flow variation doesn't cause any change in oxygenation level. Generally, these two factors depend on each other *in vivo*. In the future tumor *in vivo* experiment, the FLOOD technique, which includes blood flow (microcirculation) effect may be good for evaluation of tumor physiological information. It will provide the way to monitor both changes in microcirculation and oxygenation, which could be very important for the therapeutic response in the clinical.

3.4 BOLD signal related to blood oxygenation level variation

3.4.1 Materials and methods

Blood oxygenation control

The blood sample was prepared as before. Usually, the pO_2 of stored blood was about 20~40 mmHg. Before experiment, the oxygenation of blood sample was lowered to <10 mmHg in order to simulate the hypoxia using N_2. MRI was performed to measure five points as the baseline. Then, oxygen was led to oxygenator to increase pO_2 to >100 mmHg in the system. When pO_2 was > 100 mmHg, the oxygen gas was turned off and MRI repeated three times. The nitrogen was led into the oxygenator to decrease pO_2 from >100 mmHg to <10 mmHg. Finally, MRI was performed again twice.

In some experiments, MRI was performed continuously to measure dynamic change during whole experimental period, while the blood oxygenation increased to >100 mmHg and decreased to <10 mmHg. During this procedure, the blood flow was kept stable. Each experiment was repeated twice (Figure 4.17d). pH value of blood sample was monitored and is shown in Figure 4.18. Although the inside of the circulation system was smooth and the pump ran at low speed, blood cells may still die due to circulation of blood in the phantom system. The old blood was replaced with fresh blood after every two oxygenation cycles.

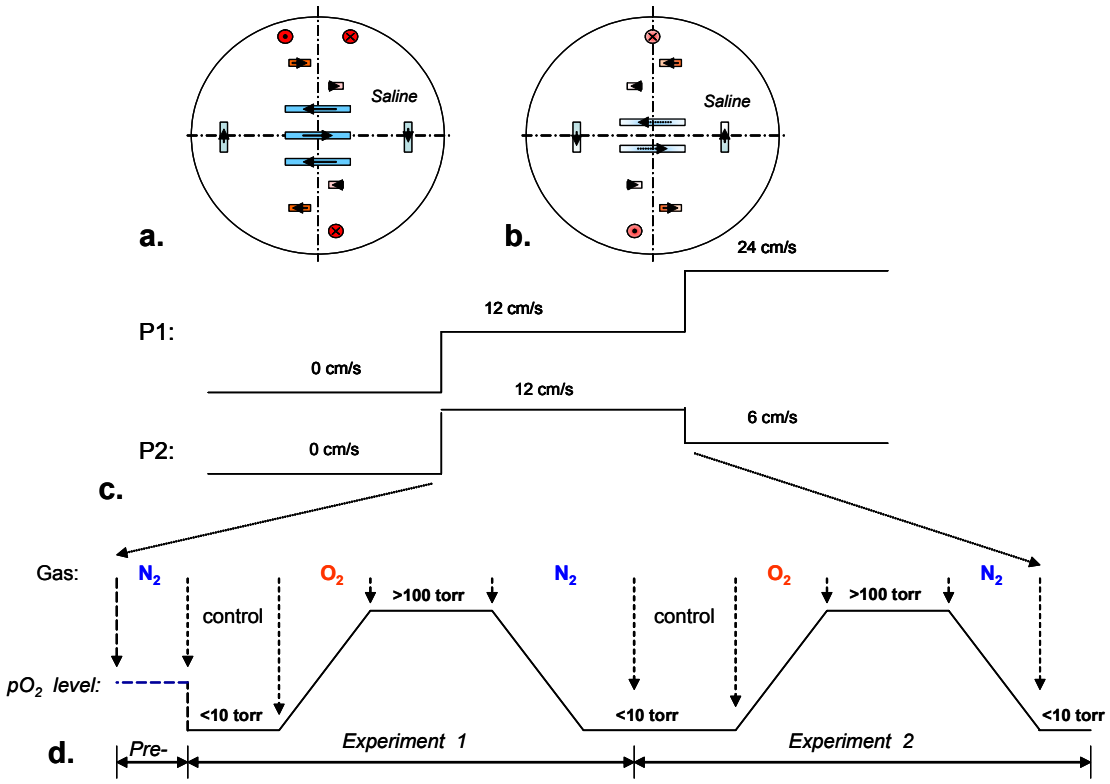

Figure 3.17 The protocol of vessels with flow and oxygenation variation.
a), b) show the vessels which were controlled by pump1 and pump2. c) shows flow velocity set up. d) shows the blood oxygenation. Each experiment was repeated one time under the same flow velocity.

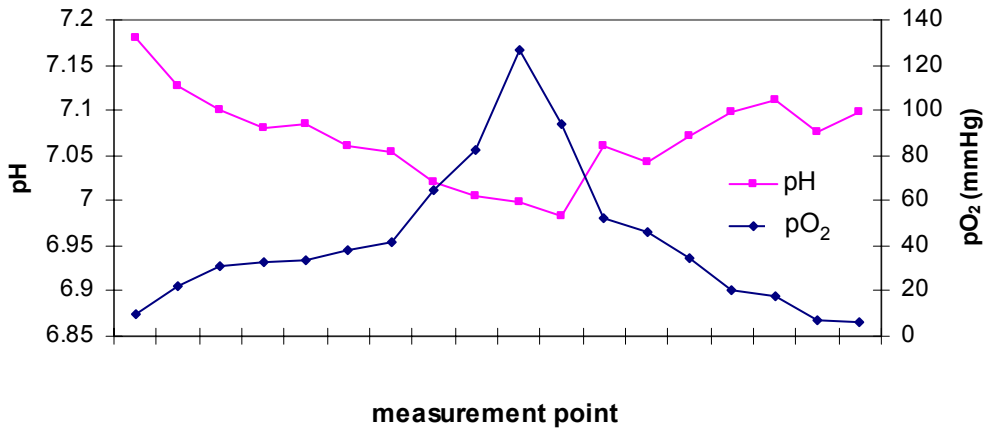

Figure 3.18 The relationship between pO_2 and pH during oxygenation variation.

Flow control

Pump1 and pump2 controlled the blood flow in the 'vessels" at three different paired values, 0 cm/s & 0 cm/s, 12 cm/s & 12 cm/s, and 24 cm/s & 6 cm/s (Figure 3.17c). During each flow setting the experiments were repeated (Figure 3.17d). For 0 cm/s & 0 cm/s experiment, the different oxygenation blood was circulated in the system and then flow stopped in the system, then, MRI to measure the BOLD signal. As before, a Transonic® T210Flowmeter with two channels was used to monitor flow on-line in real time.

Magnetic Resonance Imaging

MR experiments were performed using the 4.7 T horizontal bore system described above. A size-matched $^{1}H/^{19}F$ single turn solenoid coil was placed around the vessel model. The FLASH (Fast low angle shot) technique was used in my BOLD study. MRI parameters were TR=200 ms, TE=10 ms, flip angle=45^{o}, thickness=1mm, Matrix=128×128, FOV=50×50 mm and the oxygenation and blood flow in tubing were varied during experiment. During each MRI measurement, the phase encoding

directions were swapped to get two images with different encoding direction in order to minimize possible artifact from the coding direction. The partial pressure of blood oxygenation was monitored by Instrumentation Laboratory® pH/Blood Gas Analyzer.

Data analysis

Data analysis was on a voxel-by-voxel basis. Similar to the previous experiment analysis, the data processing could include two parts. Part one focused on each vessel angle response to the blood oxygenation variation. The signal intensity and relative signal intensity of each angle vessel were analyzed. Part two was based on vascular group including all vessels at any angle. The protocol of each vascular group is shown in (Figure 3.17a,b). The same region in different phase encoding image was processed and presented as mean value during analysis. The extra-vessel region of the area outside the vessels was analyzed (Figure 3.9). The relative signal intensity (ΔSI) of each tumor voxel was analyzed using the equation:

$$(\Delta SI) = \frac{(SI_E - SI_b)}{SI_b} \times 100\% \qquad (3\text{-}4)$$

where SI_E refers to the enhanced signal intensity in the voxel and SI_b is defined as the average of the baseline images.

3.4.2 Results

1. Each angle of vessel analysis

Raw images of BOLD response are shown in Figure 3.19. When the oxygenation was changed, vessels at different angles showed different response.

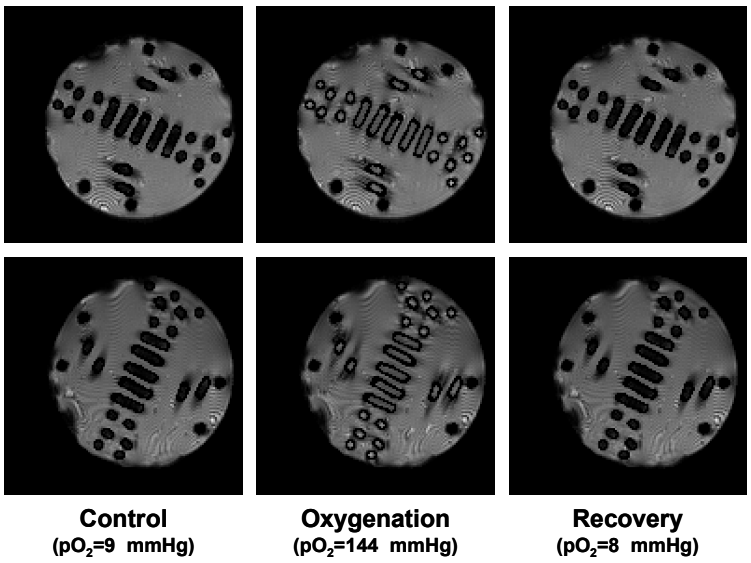

Figure 3.19 The raw images of vessel model with oxygenation variation.

The signal returned to baseline, when oxygenation was returned to baseline. Comparison of the different vessel orientation is shown in Figure 3.20 for one experiment. The highest intensity of vessel showed in 90^{o} angled vessels. All angle vessels showed a recovery of signal intensity when the oxygenation was back to baseline.

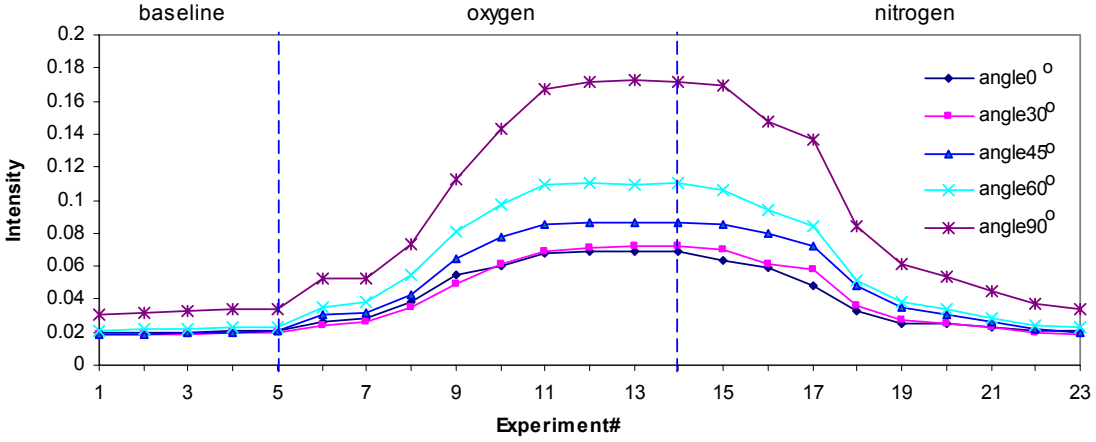

Figure 3.20 The signal intensity of different angle vessels in one experiment. (P1 =24 cm/s and P2=6 cm/s).

The mean intensity of each orientation vessel is shown for three experimental data sets in Figure 3.21. The signal intensity of 90^{o} angled vessels was the highest.

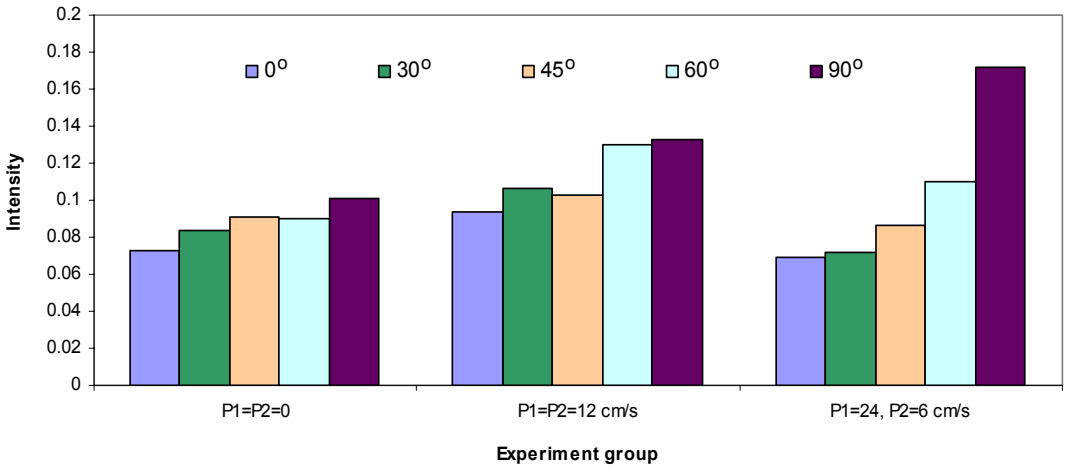

Figure 3.21 The intensity of each experiment group response to intervention

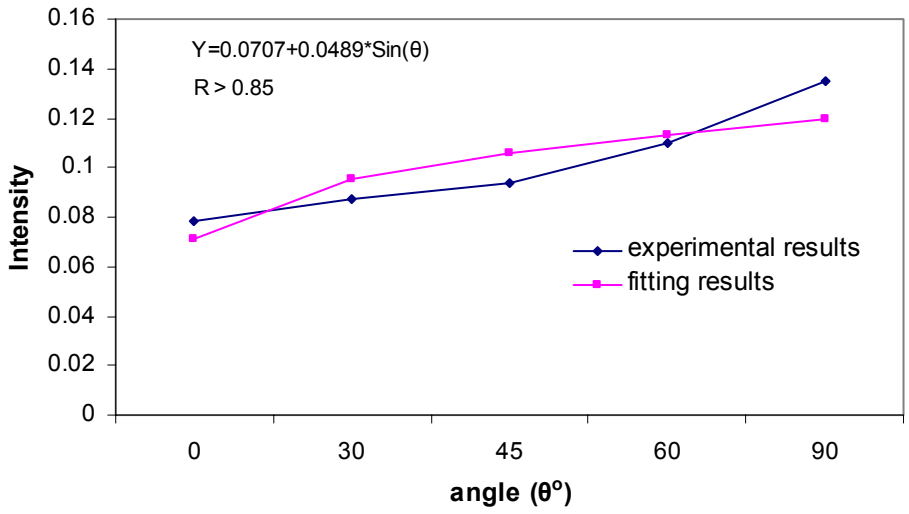

Figure 3.22 Comparison of intensity and each angled vessels

Averaging three experimental groups (six individual experiments), intensity of each angled vessel shows in Figure 3.22. The highest intensity was 90° angled vessel. There was a correlation between signal intensity and each angle (Figure 3.22). The relative signal intensity of BOLD response to oxygenation variation in each angle vessel showed around 500% enhancements, which was much higher than that

response to flow variation. And there was a correlation between relative signal intensity and each angle (Figure 3.23).

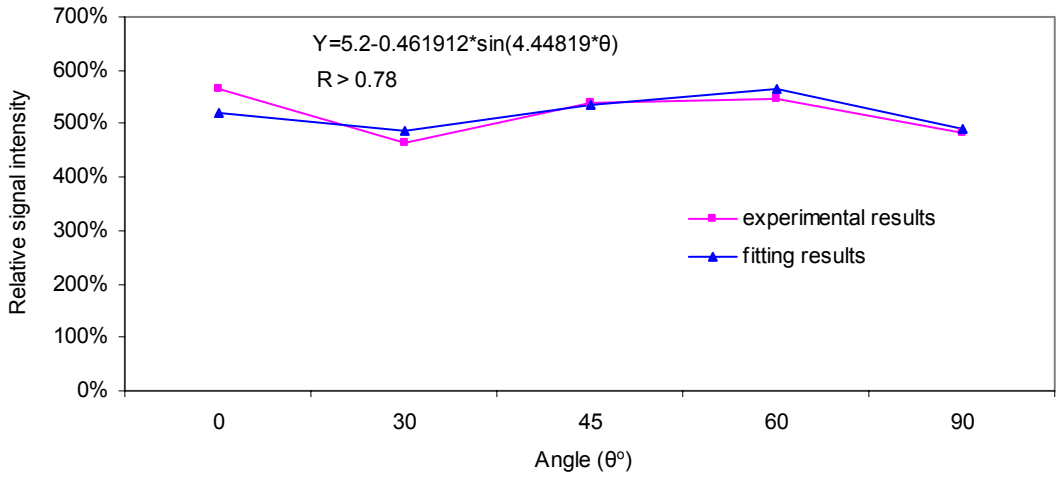

Figure 3.23 Each angle vessels response to oxygenation variation

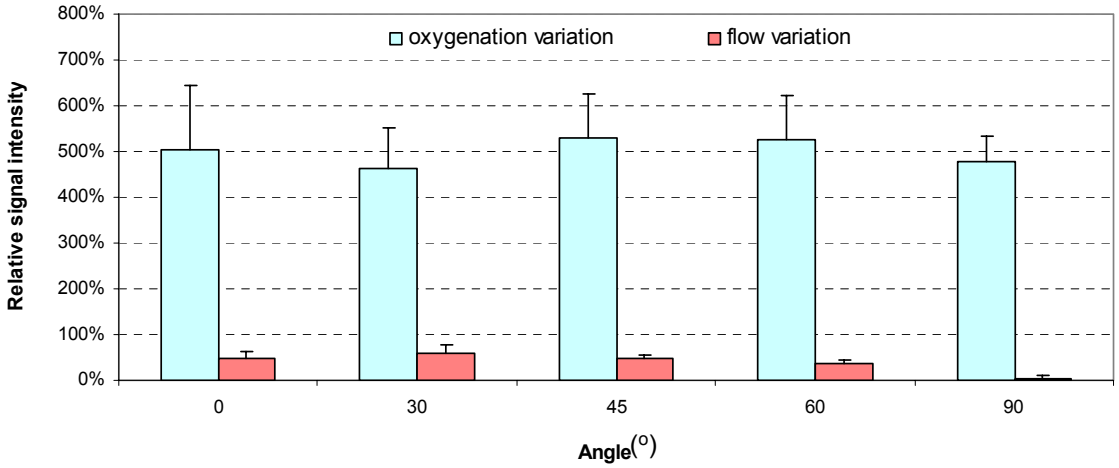

Figure 3.24 Comparison of each angle vessel with intervention

Comparing oxygenation variation with the blood flow variation showed that the relative signal intensity for each angled vessel was much more sensitive to oxygen than flow (Figure 3.24). It suggests that the change of blood oxygenation could be main contribution in each single vessel of BOLD response. The simple flow variation causes a much smaller BOLD signal change than blood oxygenation variation.

2. Vessels group analysis

Including vessels of all angles and flow directions might be a close analogy to the *in vivo* situation since tumor vessels can have random orientation. The relative signal intensity map of one experiment is shown in Figure 3.25. The images on left side were controls (pO_2=9 mmHg), the middle images show intervention (pO_2=144 mmHg), and the right images show recovery (pO_2=9 mmHg) (Figure 3.25a).

The BOLD response within all vessels increased over 700% when blood oxygenation increased 144 mmHg; then the signal was back to baseline when blood oxygenation decreased 8 mmHg (Figure 3.25b). However, the signal in an extra-vessel region also showed an 8% decrease during the intervention. It also recovered after blood oxygenation went back to baseline (Figure 3.25c). These phenomena were observed with respect to oxygenation, whatever the flow velocity in the vessel.

Figure 3.26 shows a 2nd example of the intra- and extra-vessel region response to the blood oxygenation variation. With the blood oxygenation increasing to >100 mmHg, the BOLD response in intra-vessel region increased over 400%, while, the response in extra-vessel region decreased to 5%. When the blood pO_2 was back to the 9 mmHg (same as baseline), the relative signal intensity in intra- and extra-vessel region was back to the baseline level.

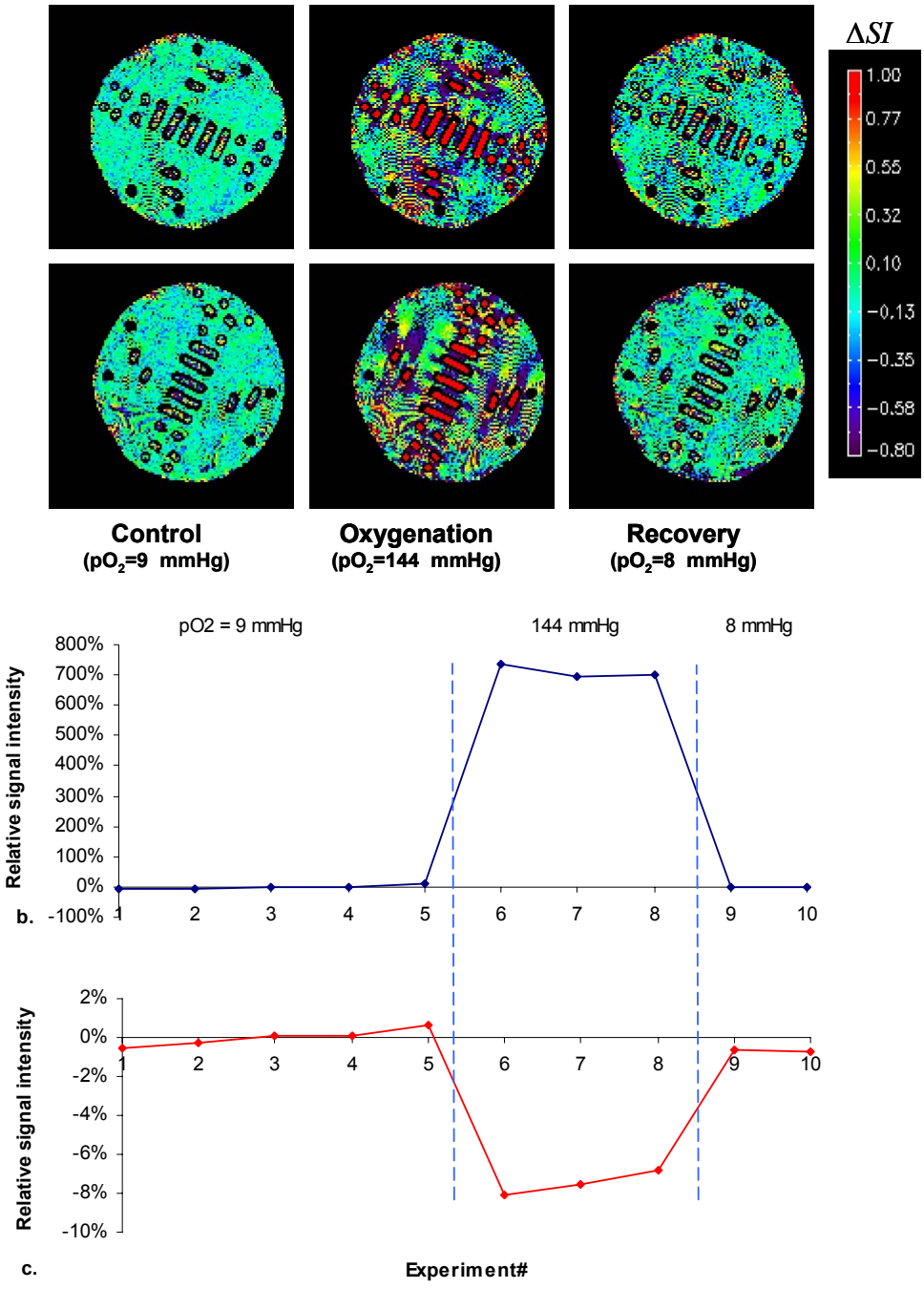

Figure 3.25 BOLD contour map and response curve in different region in one experiment. The relative intra-vessel signal intensity in increased over 700%, while the extra-vessel decreased 8% when oxygenation was altered from 9 mmHg to 144 mmHg. The relative signal intensity was back to baseline when blood oxygenation was back to 8 mmHg

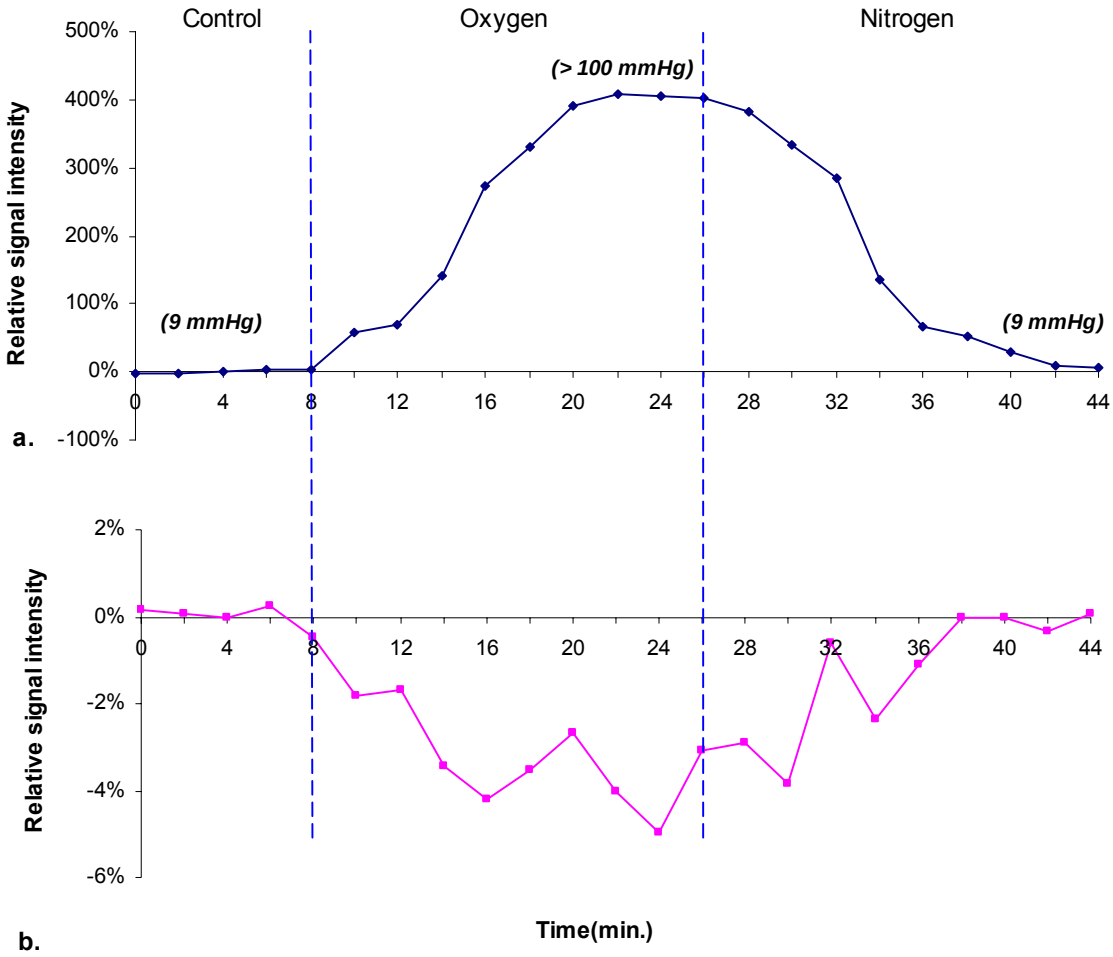

Figure 3.26 Example of response to oxygenation for intra and extra vessel regions. The blood flow velocities were 24 cm/s for pump1 and 6 cm/s for pump2. a) all intra-vessel response to oxygenation increase > 100 mmHg and decrease <10 mmHg. b) extra-vessel region decrease when oxygenation increased >100 mmHg, then signal went back to baseline when oxygenation level decreased to baseline level.

The analysis shows that six individual experiments (three experimental groups) had the same phenomenon during blood oxygenation change, which increased signal in intra-vessels region and decreased signal in extra-vessels region (Figure 3.27). There was a correlation between enhancement in intra-vessels and signal decrease in extra-vessels. The number of voxel in extra-vessel region is 228.

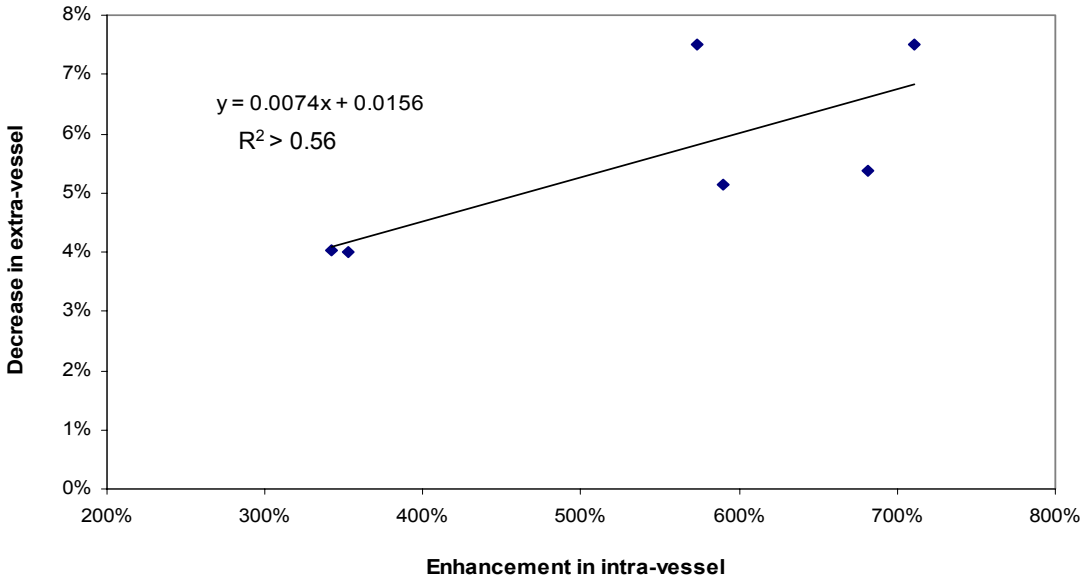

Figure 3.27 comparison of signal change in intra-vessels and extra-vessel

Across all three experiments, the BOLD response of all intra-vessel regions increased over 500% when blood oxygenation increased >100 mmHg; then the signal returned to baseline when blood oxygenation was decreased <10 mmHg a). The BOLD response of the extra-vessel regions decreased 6% when blood oxygenation increased to >100 mmHg; then the signal was back to baseline when blood oxygenation decreased to <10 mmHg (Figure 3.28).

Comparison of my previous experiment with flow velocity variation, the relative signal intensity in the same region (sum: 238 voxels) showed no change. This phenomenon demonstrated that the change of magnetic susceptibility in intra-vessel region could affect the BOLD effect in extra-vessel region (Figure 3.29).

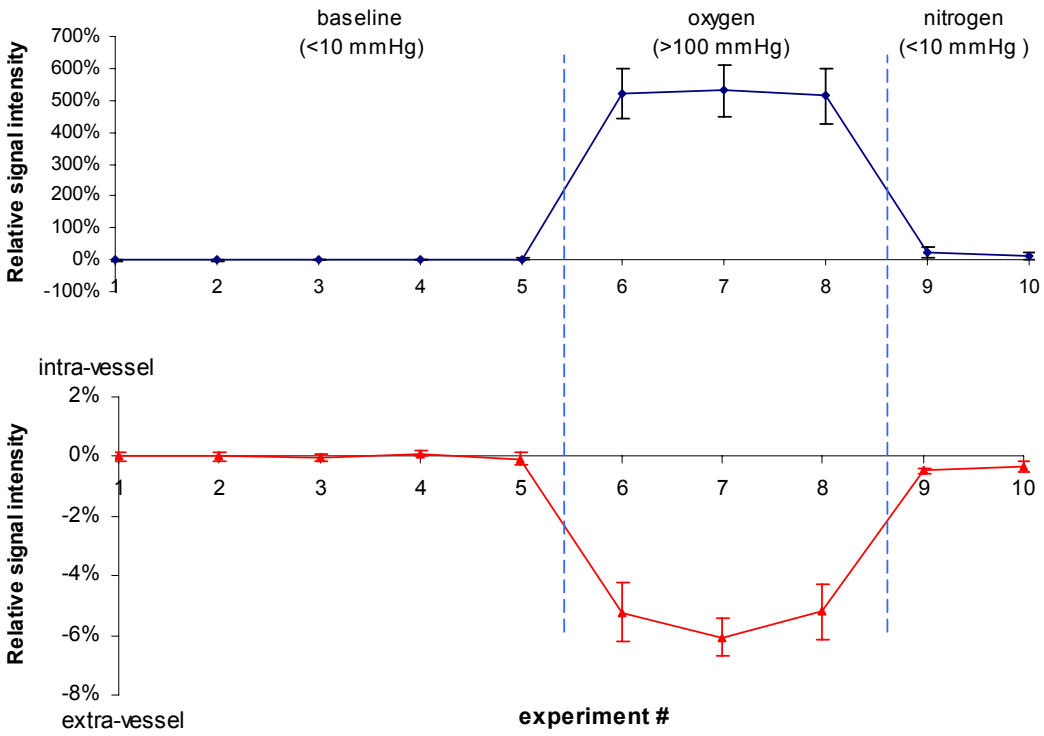

Figure 3.28 comparison of response in intra- and extra-vessel region.

The relative signal intensity in intra-vessel presented over 500% increase when blood oxygenation change from <10 mmHg to > 100 mmHg. Meanwhile, the extra-vessel region showed the 6% decrease when oxygenation change in intra-vessel.

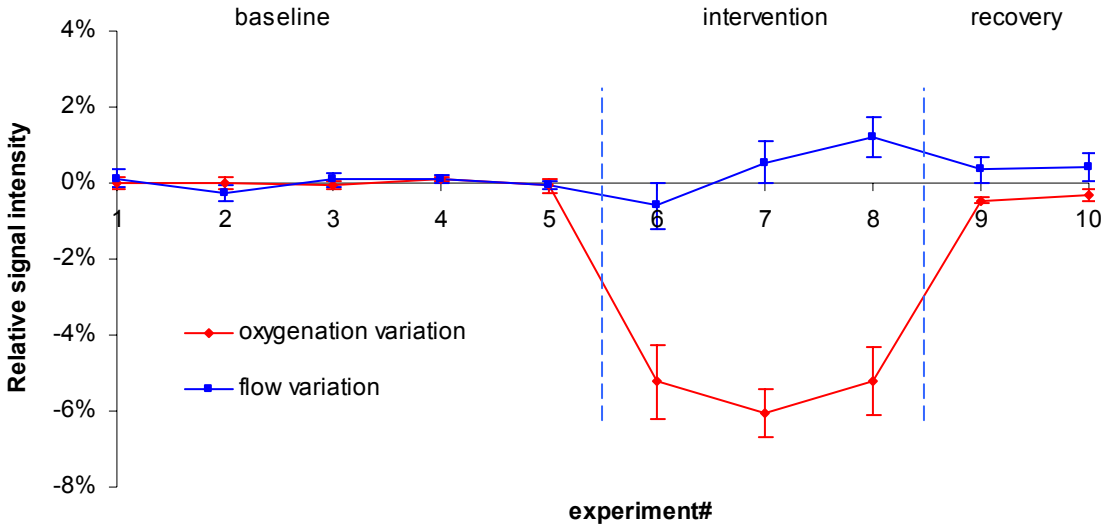

Figure 3.29 The extra-vessel region responded to flow and oxygenation variation. The flow variation showed the BOLD signal change <2%. And variation of oxygenation (from 10 mmHg to 100 mmHg) showed nearly 6% and it was back to baseline when oxygenation returned to 10 mmHg.

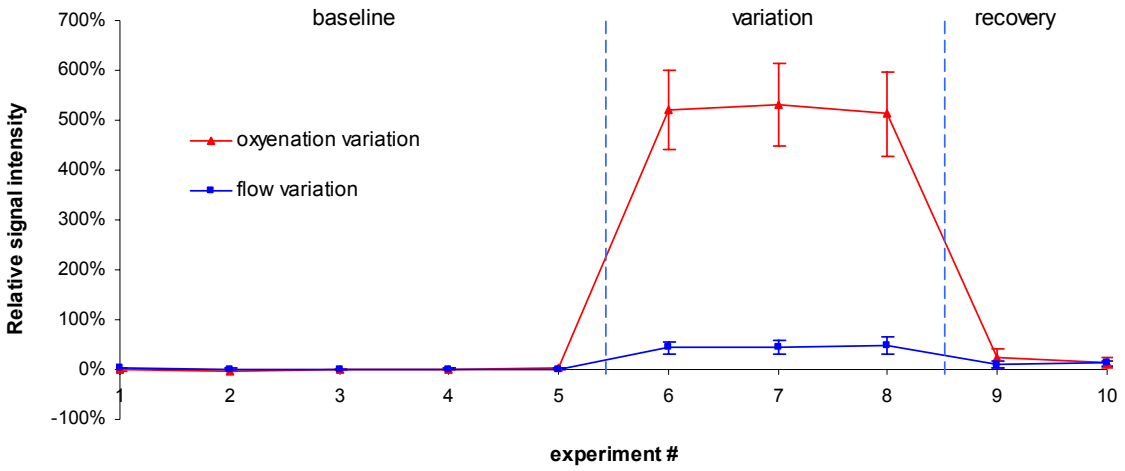

Figure 3.30 The vessel response to oxygenation and flow variation

If the BOLD response with flow variation was assumed as all positive (magnitude), the mean of BOLD response with flow variation was about 50%. Comparison of BOLD response to oxygenation variation and flow variation, it showed that signal change of oxygenation variation (>500%) was much higher than that of flow variation (50%) (Figure 3.30).

3.4.3 Discussion

From analysis of the single angle vessels the 90^{o} angle vessel showed the highest intensity compared with other angled vessels. However, the BOLD signal enhancement was around 500% in each angle vessels, which was much higher than that in flow variation. There was a correlation between signal intensity, relative signal intensity and the angle of vessel (Figure 3.22 and 3.23).

My phantom results suggest that the main contribution of BOLD signal is oxygenation variation. Since the range of tumor oxygenation variation *in vivo* during

inhalation oxygen is < 100 mmHg, the BOLD response of tumor *in vivo* may be lower than 500%. However, it was frequently found in our previous *in vivo* BOLD study that some voxels, which responded to inhalation oxygen were over 100% in human breast cancer and the animal tumor model. It indicates that BOLD response may mainly come from the oxygenation change although the change of flow may vary the relative signal intensity.

Perhaps most important is the observation of significant signal changes in the extra-vessel region (Figure 3.28). While it was $1/100^{th}$ that observed within the vessels, in principle it could lead to specific interpretations with respect to tissue physiology. This phenomenon still occurred in all experiments accompany blood oxygenation change no matter what the flow velocity in the vessels. If the blood oxygenation was not changed, the same extra-vessel region was not changed (Figure 3.29). The contrast mechanism in BOLD MRI techniques for functional or anatomical applications is based on the fact that local magnetic field homogeneity (or inhomogeneity) affects signal intensity in a gradient echo sequence (64,65). Depending on its orientation with respect to the static magnetic field and its magnetic susceptibility, a vessel modifies the magnetic field in its surround region. There is the signal cancellation which occurs within a voxel due to frequency shifts within the vessel comparing to surround tissue. Inhomogeneities of the magnetic field around the vessel cause extravascular spin dephasing affecting the signal intensity (66). This phenomenon may explain the fact that the oxyhemoglobin level variation in intra vessel region, resulting in inhomogeneity of magnetic field between intravessel and extravessel region, and magnetic susceptibility change in extravessel region.

Actually, the flow variation must influence the oxygenation *in vivo* because the local oxygenation is dependent on the oxygen transportation (blood flow or microcirculation) and the oxygen consumption. It was a limitation of my phantom study *in vitro*. According to Fick's relationship, the flow volume is an important factor for controlling the local oxygen supply. Although BOLD MRI cannot distinguish the changes in oxygenation produced by alterations in the supply of oxygen (blood flow) or in its consumption, BOLD signal mainly comes from the change of deoxyhemoglobin concentration associated with local oxygen consumption and oxygen transportation. FLOOD MRI could be a good approach to measure combination of blood flow and oxygenation which can address tumor microenvironment. The information of blood and oxygenation are very important to evaluate tumor physiological status.

Because the local oxygenation is dependent on the oxygen transport and the oxygen consumption, the local oxygenation must decrease if the flow decreases and the metabolism of cancer cells is constant.

3.5 Conclusion

The phantom studies showed that there was the different the BOLD response in different orientation of vessel due to variation of blood flow. The vessels, which were perpendicular to $B_{0,}$ showed less signal "in-flow effect" during flow variation. The sensitivity of BOLD signal to flow variation is dependent on the vessel orientation. My phantom experiment explored the BOLD response to blood flow regulation, which is important physiological mechanism in microcirculation. The phantom results

also demonstrated that our BOLD analysis strategy can minimize the effects of perfusion regulation. The phantom studies showed that the change of the blood oxygenation could be the main part for BOLD response compared with blood flow variation. Of course the change in blood flow must affect the local oxygenation *in vivo*. The "steal effect" in BOLD MRI may be mainly contributed by flow change associating with oxygenation decrease during intervention. The signal of extra-vessel region can be decreased by change of magnetic susceptibility in intra-vessel. These observations may give us an important view in fMRI and BOLD investigations.

CHAPTER 4

Comparison of DCE and BOLD MRI in Animal Experiments

4.1 Introduction

Based on my phantom experiments, animal studies focused on using DCE and BOLD techniques for exploring prostate and breast tumor physiology. Part of research has been published.

4.2 Prostate Tumor Studies

4.2.1 Introductions

Imaging provides the opportunity to non-invasively characterize tumors with three primary goals: identification of tumors, prognosis of potential tumor development, and the longitudinal response to therapy. Tumors comprise heterogeneous populations of stromal and tumor cells that differ in their growth rates and sensitivity to therapeutic agents. Owing to this diversity, marked regional differences are also observed in microenvironmental characteristics, such as oxygenation and microcirculation. Heterogeneity may be spatial and temporal and imaging allows non-invasive repeat assessment. It may be particularly valuable in prostate cancer, which is often a heterogeneous multi-focal disease with the potential development ranging from aggressive metastatic spread to indolent stasis. A major

goal of radiology is to be able to differentiate patients who need immediate aggressive therapy from those better served by watchful waiting.

Proton MRI not only provides non-invasive assessment of detailed tumor anatomy, but specific MRI techniques may give an indication of tumor angiogenesis and pathophysiological state (13,41,67,68). Dynamic Contrast Enhanced MRI based on the transport properties of small paramagnetic contrast agents, such as Gd-DTPA, provides an indication of tumor perfusion and vessel permeability. There have been many semi quantitative reports together with increasingly sophisticated pharmacokinetic models to monitor tumor vascular function (69-72). Another approach exploits intrinsic contrast based on Blood Oxygenation Level Dependent (BOLD) signal in response to inhaling hyperoxic gas, such as oxygen or carbogen (5% CO_2, 95% O_2). The conversion of paramagnetic deoxyhemoglobin to diamagnetic oxyhemoglobin influences the MR signal, particularly in T2 weighted images (20). However, the BOLD effect is also sensitive to changes in blood flow and vascular volume, and hence, the term FLOOD (Flow and oxygen level dependent) has been introduced (50). To date, there have been limited reports of the use of the BOLD effect to characterize tumors (18,25-27,30,31,49,63,73,74). Still fewer reports have examined BOLD and DCE together in the same tumors consecutively or in conjunction with histology (18,75).

I hypothesized that the combined application of BOLD and DCE MRI could provide additional insight into tumor pathophysiology. In this study, I tested this notion in two syngeneic rat prostate tumor sublines noted for their differences in growth rates and vascular maturity. This work was undertaken prior to my

sponsorship by the DOD Breast Cancer. Initiation providing a perfect segues between phantom and pilot clinical study. The animal experiments were undertaken by Dr. Dawen Zhao, but I performed all data analysis.

4.2.2 Materials and Methods

Experiments were approved by the UT-Southwestern Institutional Animal Care and Use Committee.

Animal model

Two sublines of the Dunning prostate R3327 adenocarcinoma were selected: H, a well-differentiated, hormone dependent slow-growing tumor with a volume doubling time (VDT) of 16 days, and the AT1, an anaplastic and faster-growing subline with a VDT of 5 days (76-78). Tumor tissues were originally obtained from Dr. J. T. Isaacs (Johns Hopkins University, Baltimore, MD) and provided to us by Dr. Peter Peschke (Heidelberg, Germany). Eight tumors of each subline were implanted in a skin pedicle surgically created on the foreback of adult male syngeneic Copenhagen-2331 rats, as described in detail previously (79). Tumors were allowed to grow to about 1 cm^3 and were investigated by MRI. The rats were anesthetized with ketamine hydrochloride 200 μl (100 mg/ml) IP, and maintained with air and isoflurane (1.3%; 1 dm^3/min). A heparin tipped catheter (27 G butterfly, Abbott Labs, Chicago, IL) was placed in the right tail vein. The body temperature of rats was maintained with a circulating warm-water blanket. A reference capillary phantom containing saline was placed adjacent to selected tumors.

MRI technique

A size-matched single turn solenoid volume coil was placed around the tumor and MR experiments were performed using a 4.7 T horizontal bore system with actively shielded gradients (GE Omega with Acustar®). Vascular oxygen dynamics were assessed using BOLD contrast ^{1}H MRI in a coronal section parallel to the rat body acquired using a series of spin echo planar images sensitive to both T1 and T2 with a field of view 40×40 mm, matrix 32×32, and thickness 2 mm. This pulse burst saturation recovery MBEST sequence has been used by Mason's lab for both ^{19}F MRI oximetry and ^{1}H contrast studies (63,80). Initial saturation is non-slice selective, thereby saturating signal throughout the tumor and minimizing in-flow effects, while a constant recovery time τ = 500 ms (= TR) and TE = 33.5 ms. Each experiment included a series of fifty-six consecutive echo planar images obtained at 5 s intervals. Baseline stability was measured for up to 5 mins, while the rat breathed air. For BOLD contrast measurements, baseline was assessed for 25 s (images 1 to 5) before respiratory challenge with oxygen (1 dm^3/min) for a period of 255 s (images 6 to 56). Following a re-equilibration period of breathing air (15 minutes), a new baseline was measured for 25 s and then a bolus of Gd-DTPA (125 μl 0.1 mmol/kg, Magnevist™, Berlex) was injected manually via the tail vein catheter in situ over 1 s. A further series of echo planar images was acquired without changing animal position.

Relative signal intensity

Changes in signal intensity and model fitting were assessed on a voxel-by-voxel basis. Initial inspection showed occasional signal spikes, and thus, a pre filter was applied removing any data points, which deviated from the mean signal intensity by more than three standard deviations of the complete curve. The baseline signal

intensity, SI_B, of each voxel was defined as the average of the five initial images under baseline conditions. The relative signal intensity changes of each tumor voxel with respect to each intervention (breathing oxygen or Gd-DTPA injection) were analyzed statistically using the equation:

$$\Delta SI = \frac{\left(SI_E - SI_B\right)}{SI_B} \times 100\ \% \qquad (4\text{-}1)$$

where SI_E refers to the enhanced signal intensity of the voxel. Image normalization yielded voxel-by-voxel signal intensity changes from baseline values expressed as a percentage change. Mean (ΔSI) is directly related to area under the curve (AUC). Each tumor was also divided into peripheral and central regions. The peripheral region occupied the two outermost voxels of the tumor. The boundary occupied a single voxel width and the remaining area was considered to be central.

Regional analysis

Each tumor was divided into the central and peripheral region. Due to distortion in the EPI experiment, the tumor was not a circle or regular shape. It was difficult to classify the tumor periphery and center region. The rule to classify the central and peripheral region of tumor was based on: from outside to tumor inside, the peripheral region was defined as the outside two voxels for each tumor. Then there was one voxel as a boundary. Finally, the remaining voxels were the central region. Since the voxel number of some tumors was small, they did not follow this rule. The classification of tumor region is shown Figure 4-1 and Table 4-1.

Table 4-1 Tumor regions

Tumor group	Volume (cm^3)	Region (%)	
		Periphery	Center
AT1 (n=8)	1.6 ± 0.1	60 ± 2	18 ± 1
H (n=8)	2.4 ± 0.5	55 ± 2	24 ± 2

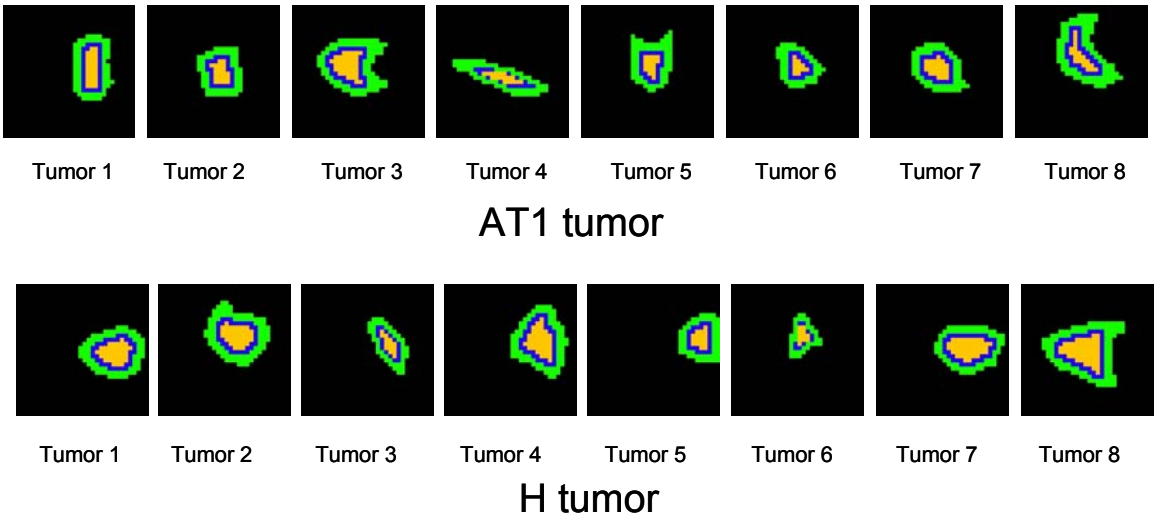

Figure 4.1 The tumor regional definition for AT1 and H tumors
The yellow color regions show the central region, the green color regions are peripheral region. The blue color regions are the middle region.

Pharmacokinetic modeling

Contrast enhancement was quantified using the Brix two-compartment model (81) to assess the vascular permeability, Kep. For a bolus injection:

$$\frac{SI_E}{SI_0} = 1 + A^H \cdot K_{ep}\left(\frac{e^{-K_{ep}\,t} - e^{-K_{el}\,t}}{K_{el} - K_{ep}}\right) \qquad (4\text{-}2)$$

where A^H is a parameter that depends on properties of the tissue, the MR sequence, and the infusion rate; SI_E is signal intensity after injection of contrast agent; SI_0 is the signal intensity before injection; K_{ep} is the rate constant between

extravascular extracellular space (EES) and plasma, which is affected by microvascular permeability; K_{el} is the elimination rate of tracer from the central compartment. I have previously shown that ΔSI is proportional to [Gd-DTPA] using this pulse sequence in gel phantoms at 4.7 T (Figure 4.2) (63).

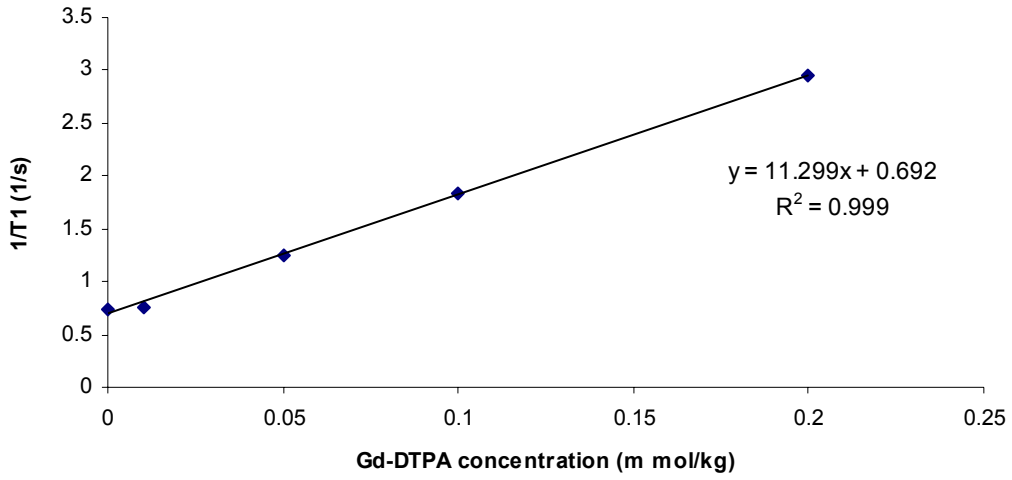

Figure 4.2 Comparison of 1/T1 proportional responses and Gd-DTPA concentration

Histology

Following MR experiment, pimonidazole hydrochloride (Hypoxyprobe-1; NPI, Belmont, MA) was injected into the tail vein at a dose of 60 mg/kg. Ninety minutes later the blue fluorescent dye Hoechst 33342 (Molecular Probes, Eugene, OR) was injected via the tail vein of anesthetized rats at a concentration of 10 mg/kg in 0.9% saline (0.1 ml), and the tumors were excised 1 min later. For immunohistochemistry, the tissues were immediately immersed in liquid nitrogen and stored at -80 ^{o}C.

After cryostat sectioning (6 μm thick), tumor sections were fixed in acetone for 5 min and then re-hydrated in phosphate buffer saline containing 0.1% Tween-20 (PBST) for 10 min. Monoclonal antibody Mab1 (NPI, Inc., Belmont, MA) that detects pimonidazole-protein adducts was diluted 1:100 and added to frozen sections followed by incubation for 2 hr at 37 °C. Slides were then incubated for 1 hr at 37 °C with horseradish peroxidase (HRP)- conjugated goat anti mouse secondary antibody (1: 100 dilution; Serotec, Raleigh, NC). After a PBST wash, sections were immersed in AEC substrate (3-amino-9-ethylcarbazole, Vector Laboratories, Inc., Burlingame, CA) for 15 min at room temperature. Finally, sections were counterstained with hematoxylin and observed under light microscopy. Hypoxic fraction was determined as area positively stained for pimonidazole relative to the total tissue area using Metaview software. Mouse anti rat CD31 monoclonal antibody (1:20; Serotec, Raleigh, NC) and HRP- conjugated goat anti mouse secondary antibody (1:100) were used to detect tumor blood vessels on 6 μm sections immediately adjacent to those used for detection of hypoxia. The whole tumor histology work was completed by Dr. Albert van der Kogel and his colleague Dr. Jan Bussink in University Nijmegen, Netherlands.

Statistics

Data processing used a SUN SPARC workstation and PC with C program and IDL software with programs written by me. Image display used a commercial graph display and analysis package (SigmaPlot 2000). All results are presented as mean ± s.e. Comparisons between the groups were performed using an Analysis of Variance (ANOVA) with significance set at $p < 0.001$ (Statview, SAS, Carey, NC). Data were

assessed in terms of individual voxels, tumor regions, tumors, and the whole tumor group with respect to interventions based on numerical values.

4.2.3 Results

^{1}H MRI showed distinct heterogeneity in signal intensity across tumors of each type (Figure 4.3) with mean signal stability during repeat measurements under baseline conditions (variation <2%, Figure 4.4). Both tumor types showed significant regionally heterogeneous changes in the BOLD signal contrast with respect to oxygen inhalation (Figure 4.3a) or Gd-DTPA infusion (Figure 4.3b). In response to oxygen inhalation, mean signal intensity increased significantly, though there was a delay of about 40 s after switching gases. The mean signal intensity for the groups of tumors increased rapidly to a plateau about 40% (AT1) (Figure 4.4a) and 30% (H) (Figure 4.4b) above baseline. Following Gd-DTPA infusion, signal intensity rapidly increased above baseline to a peak 50% for the AT1 tumors (Figure 4.4a) and 70% for the H tumors (Figure 4.4b) and then settled to equilibrium at values of 30% and 50% above baseline.

To further examine the spatial heterogeneity evident in Figure 4.1, the regional response of each tumor was examined by dividing the tumors into central (mean area 18±1% for AT1 tumors, 24±2% for H tumors) and peripheral regions (60 ±2% for AT1 tumors, 55±3% for H tumors). As a group, the AT1 tumors showed a significantly higher response in the periphery compared to the center with both BOLD and DCE (($p<0.0001$), Table 4.2, Figure 4.5a and b). The group of H tumors showed the opposite effect for both interventions, but with a particularly large DCE in the tumor center (Table 4.2, Figure 4.5c and d). Considering individual tumors five of

eight AT1 tumors showed significantly higher response to oxygen in the peripheral region compared to that in the central region ($p<0.01$).

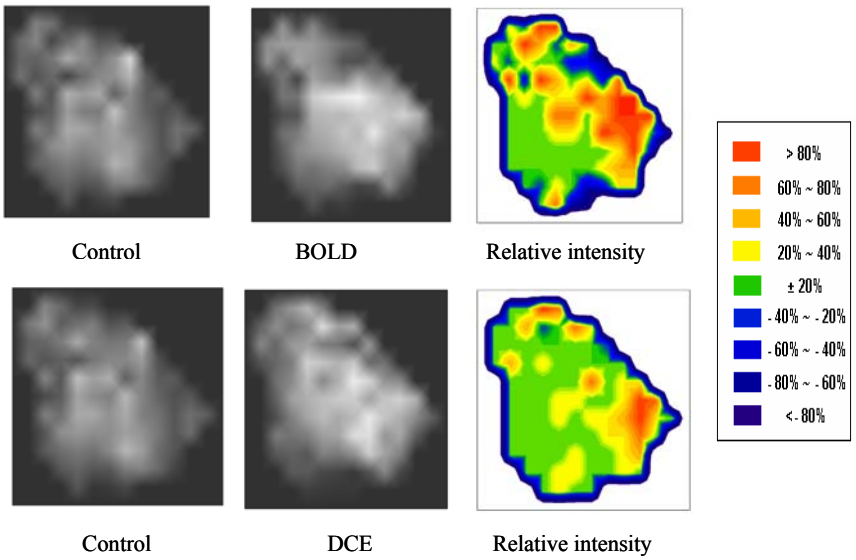

a.

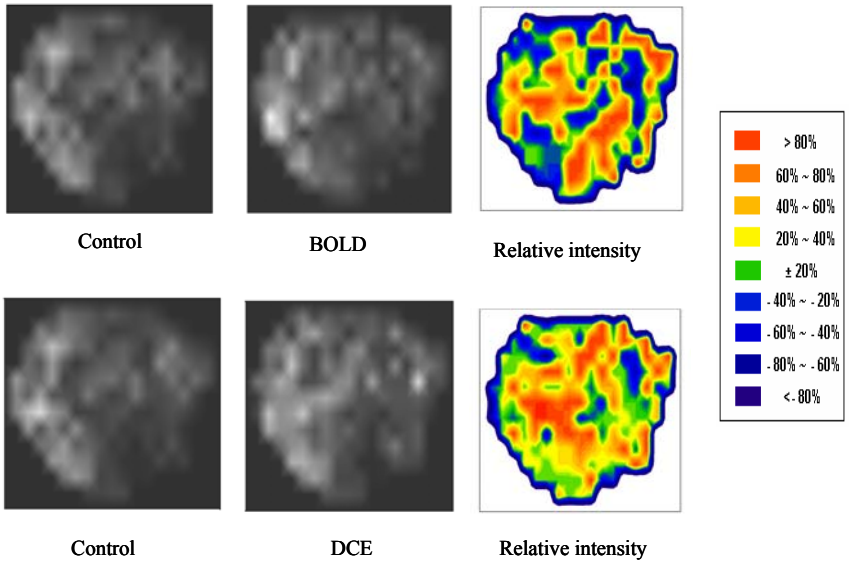

b.

Figure 4.3 ^{1}H MR response of vascular dynamics in AT1 and H tumor

T1-weighted EPI of the representative AT1 (a) and H (b) tumor. Left: control baseline images, Center: images following intervention observed after 200s for BOLD and 40 s for DCE. Right: contour maps showing changes in relative signal intensity. The color scale indicates the magnitude of relative signal intensity (increase or decrease).

Table 4.2 The regional mean signal intensity (ΔSI) of individual tumors after oxygen inhalation or injection of contrast agent and pharmacokinetic analysis

Tumor group	Volume (cm^3)	Region (%)[@]		$(\Delta SI)_{BOLD}$[+]		$(\Delta SI)_{DCE}$[+]		K_{ep} (min^{-1})[++]	
		Periphery	Center	Periphery	Center	Periphery	Center	Periphery	Center
AT1 (#1)	1.5	55	22	20±1	27±2	26±1*	11±1	2.60±0.39	3.68±0.98
AT1 (#2)	2.0	58	19	84±5	69±5	30±3*	-3±1	1.59±0.45	
AT1 (#3)	2.0	55	23	44±3*	4±0	30±1	41±2*	1.88±0.27	2.65±0.59
AT1 (#4)	1.1	67	16	18±1*	1±0	42±1*	-20±1	5.51±0.75	
AT1 (#5)	1.8	64	15	24±2*	-2±0	11±0*	-3±0	3.86±0.51	1.41±0.37
AT1 (#6)	1.2	62	13	30±2	26±2	20±1	17±1	3.26±0.38	0.73
AT1 (#7)	1.7	56	21	98±7*	62±5	160±7	155±4	3.57±0.62	3.62±0.80
AT1 (#8)	14.7	63	13	16±1*	-1±0	23±1*	-7±0	2.57±0.31	3.43±0.51
Mean◆	1.6±0.1	60±2	18±1	42±3*	23±2	43±1*	24±1	3.11±0.44	2.59±0.51
H (#1)	2.1	52	25	19±1	54±4*	13±1	12±1	4.63±0.76	5.57±0.78
H (#2)	3.5	57	23	4±0	56±4*	0±0	7±1*	2.24±0.96	2.19±1.37
H (#3)	1.4	60	18	31±2*	10±1	64±3*	37±2	1.50±0.41	1.56±0.29
H (#4)	1.4	51	25	27±2	20±1	61±2	65±2	3.85±0.56	2.57±0.38
H (#5)	2.4	59	18	0±0	64±4*	29±3	741±46*	2.57±0.45	2.99±0.84
H (#6)	1.5	64	23	28±2	78±6*	15±1	47±3*	5.39±1.25	1.13±0.85
H (#7)	1.3	46	30	33±2	36±3	38±2	65±2*	2.77±0.46	2.72±0.52
H (#8)	5.6	51	28	20±1	14±1	24±1	19±1	3.76±0.48	4.87±0.52
Mean◆	2.4±0.5	55±2	24±2	20±1	42±3*	31±1	124±6*	3.34±0.46	2.95±0.54

[@]: Percentage of whole tumor slice

+: Relative signal change from baseline %, Mean ± s.e.

◆: $\frac{\sum_{T=1}^{n}\sum_{t=1}^{51}\overline{\Delta SI_{T,t}}}{n \cdot 51}$, where $\overline{\Delta SI}$ is the mean for each tumor (T) at each time point post intervention (t) , n is the number of different tumor group.

*: Mean value is significantly greater than that in other region, $p<0.001$.

++: blank Kep means no fitting result

Likewise, five of eight tumors showed significantly greater responses to Gd-DTPA in the peripheral region ($p<0.01$). Conversely, for the H tumors, four of eight showed a significantly higher BOLD response in the central region ($p<0.01$), and only

of eight showed a significantly higher response in the peripheral region ($p<0.01$). For DCE contrast, four H tumors showed significantly higher central response ($p<0.01$).

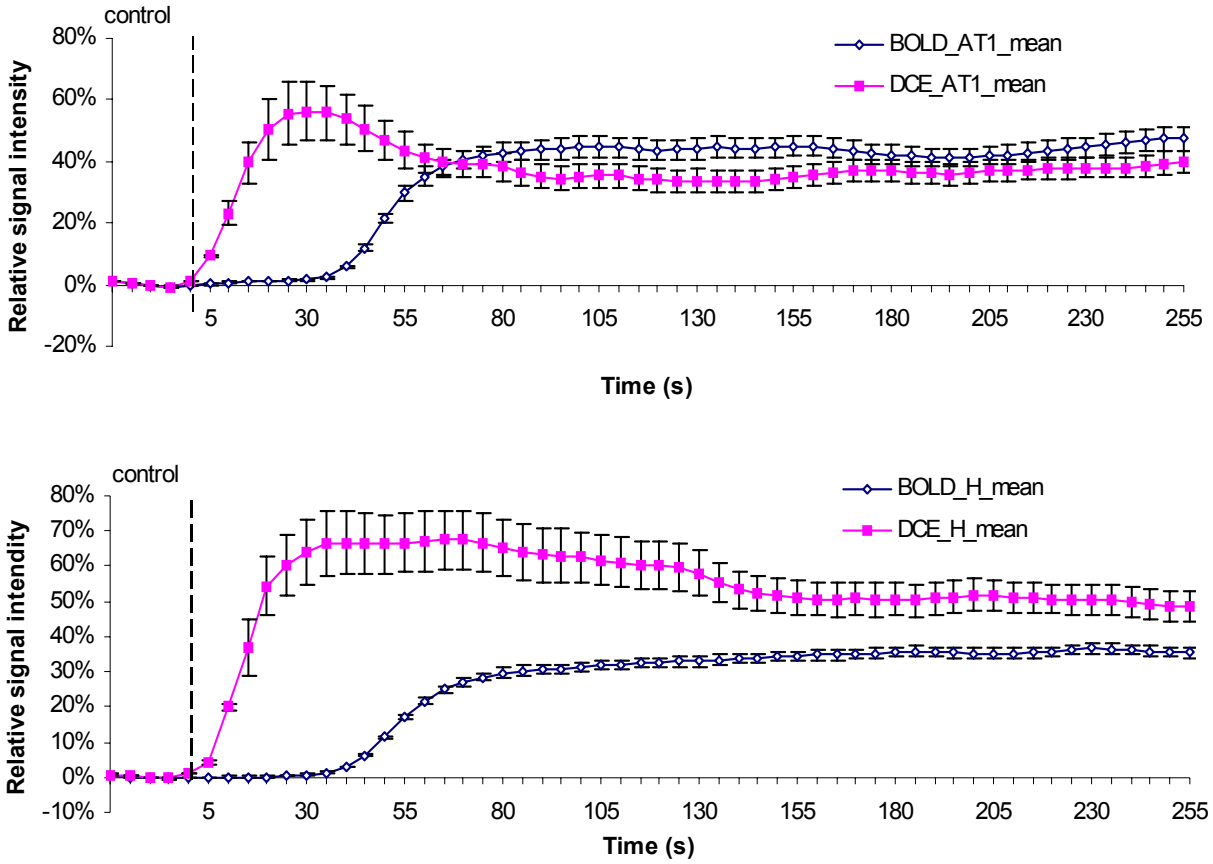

Figure 4.4 Comparison of vascular kinetics of two tumor types

Mean ^{1}H MRI signal intensity in response to oxygen inhalation (BOLD) (■) and Gd-DTPA infusion (◊) for groups of (a) AT1 tumors (n=8) and (b) H tumors (n=8). Lines indicate mean±SE. Dotted vertical lines show start of intervention. An immediate signal response is seen for Gd-DTPA, whereas the BOLD response is somewhat delayed (~ 40 s).

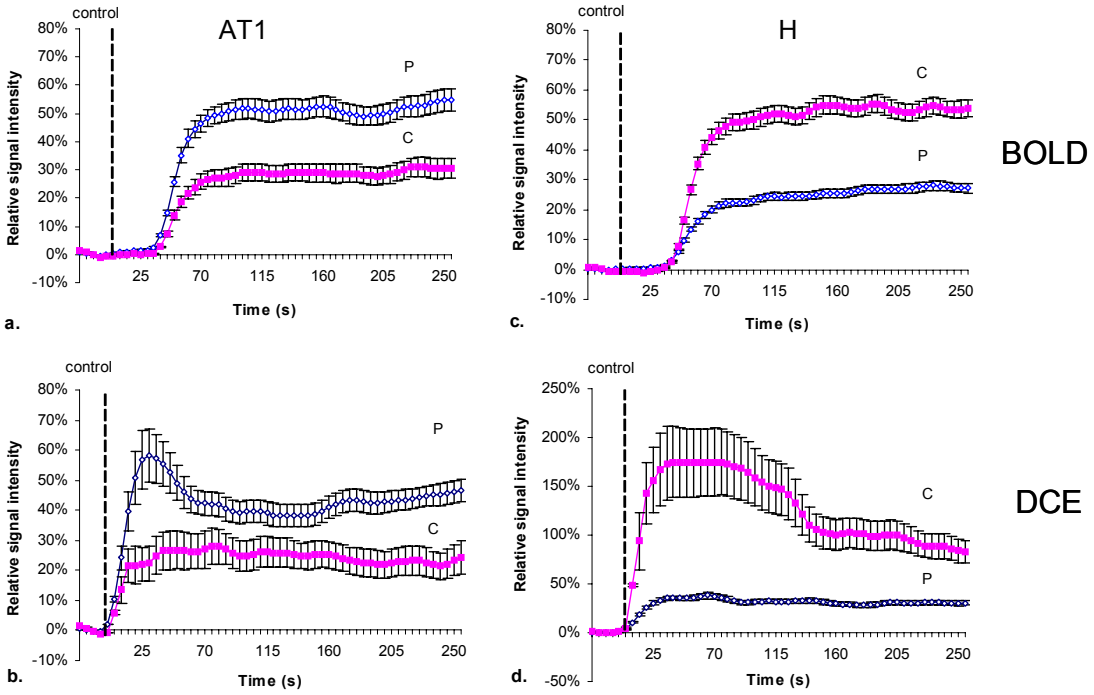

Figure 4.5 Comparison of regional vascular kinetics of AT1 and H tumors

The mean ^{1}H MR signal intensity in central region (C; filled symbols) and peripheral region (P, open symbols) in response to oxygen inhalation (BOLD) (upper) and Gd-DTPA infusion (DCE) (lower). The mean ΔSI of AT1 tumors (n=8) in BOLD and DCE was significantly higher in the peripheral regions than that in the central regions ($p<0.0001$) (a and b). For H tumors (n=8) the mean response to BOLD and DCE in the peripheral regions was significant lower than that in the central regions ($p<0.0001$) (c and d). Lines indicate mean±SE.

Tumors may also be considered in terms of the fate of individual voxels, i.e., spatial heterogeneity. In this case, it was found that the signal had changed by more than 20% in more than 70% of the tumor regions in the AT1 tumors within 20 s of administering Gd-DTPA (Figure 4.6b). More than 30% of the voxels had changed more than 60% within 125 s, though intriguingly about one third showed a signal decline rather than increase. H tumors showed a rather similar time course, but the fraction of responding tumor was larger (~90% showed > 20% change after 20 s).

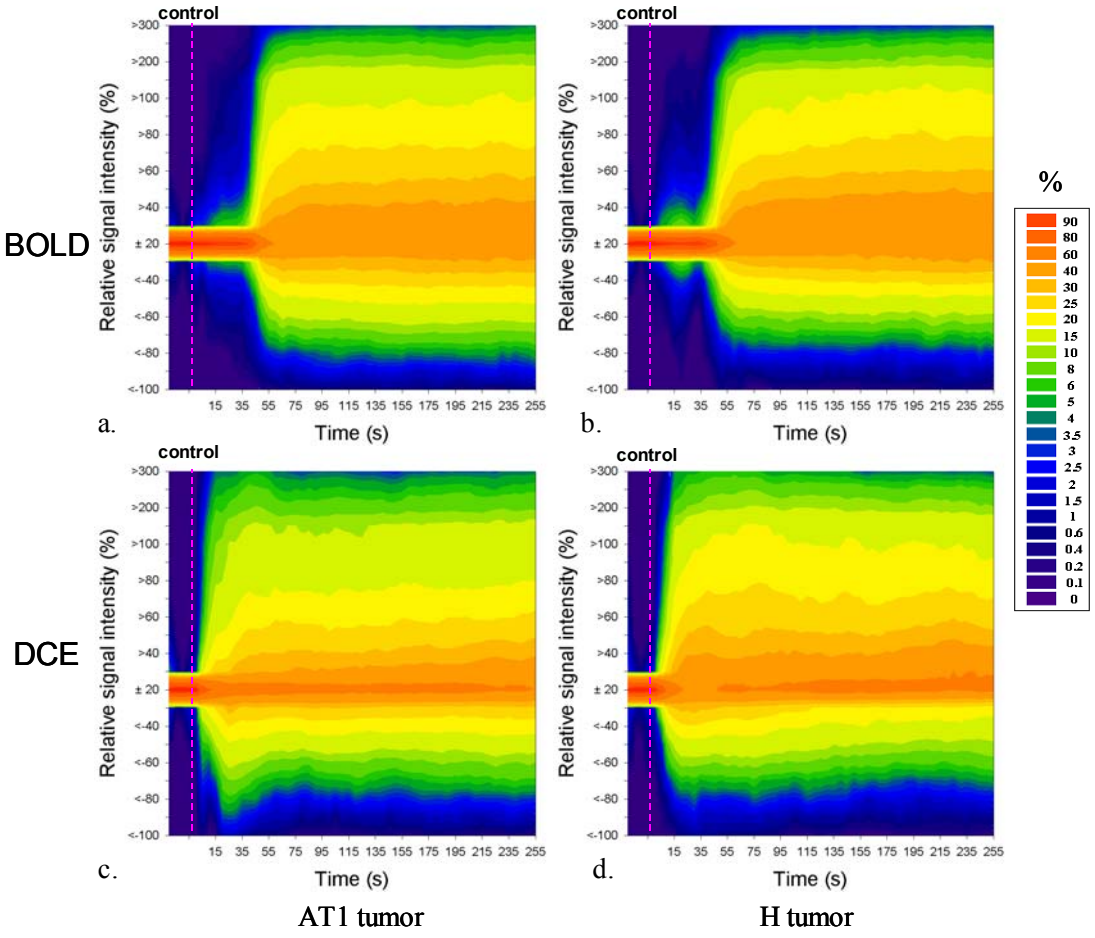

Figure 4.6 Magnitude of dynamic signal response to intervention

Variations in distribution of relative signal intensity in response to intervention for the two tumor sublines. BOLD response to breathing oxygen is shown in a and b for groups of AT1 and H subline tumors respectively. A more rapid response is observed following Gd-DTPA infusion (c and d). Hotter colors represent a larger fractional volume of tumor as shown by scale.

The BOLD response was delayed relative to DCE with minimal change after 20 s, but by 125 s after switching gas about 90% of the AT1 tumor regions had responded by > 20% (Figure 4.6a). H tumors behaved similarly. Intriguingly, about as many voxels showed a signal decrease of >20%, as showed such an increase in response to either intervention in both tumor types. Signal loss was generally restricted to a 20 to 40% range, whereas 20% of voxels showed >80% signal gain in response to either

intervention in both tumor types. The pharmacokinetic parameter mean *Kep* showed no consistent significant regional differences in either individual tumors or between tumor types. (Table 4.2, Figure 4.7).

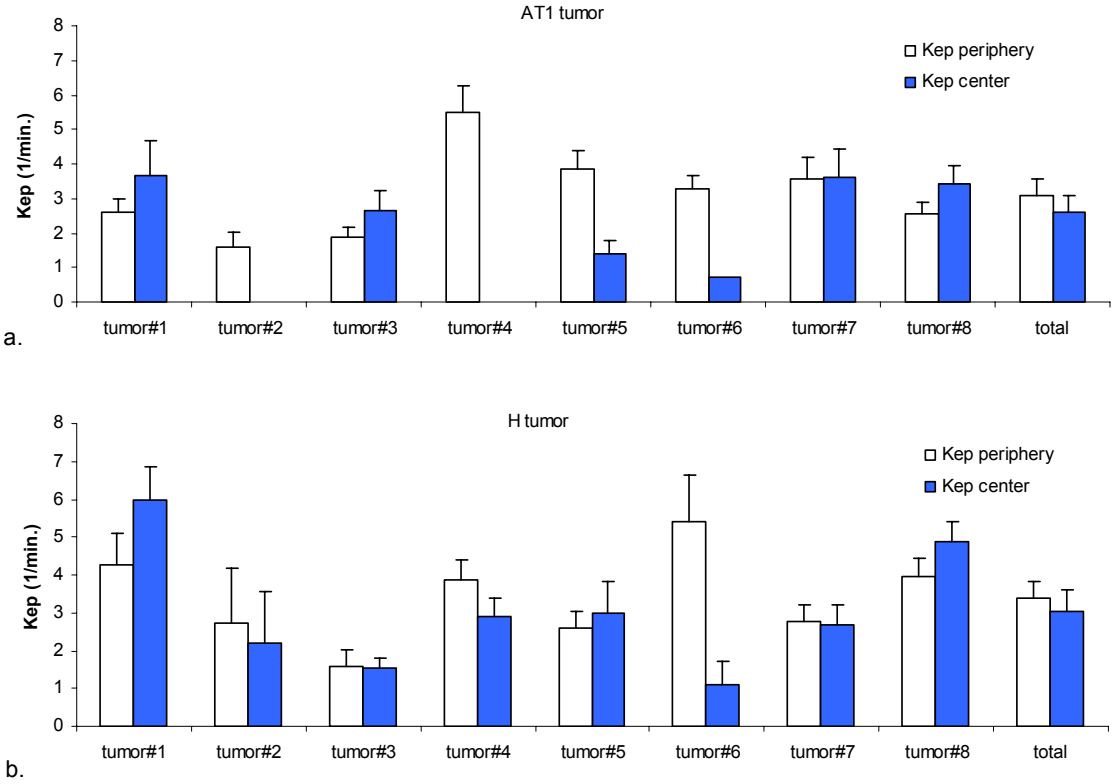

Figure 4.7 Comparison of regional pharmacokinetic Kep of AT1 and H tumors a) AT1 tumors; b) H tumors. Bars indicate mean±SE; open periphery; shaded, center. AT1 #2 and #4 tumors show no Kep results in central region.

Following a single bolus of Gd-DTPA signal enhancement persisted in both tumor sublines for many minutes (Figure 4.5b,d). The BOLD effect can also be made to persist by continuously breathing hyperoxic gas (Figure 4.5a,c). However, if the inhaled gas was returned to air, the signal perturbation rapidly returned to baseline (Figure 4.8b). For Gd-DTPA injection, it took longer to wash out the agent from body (Figure 4.8a).

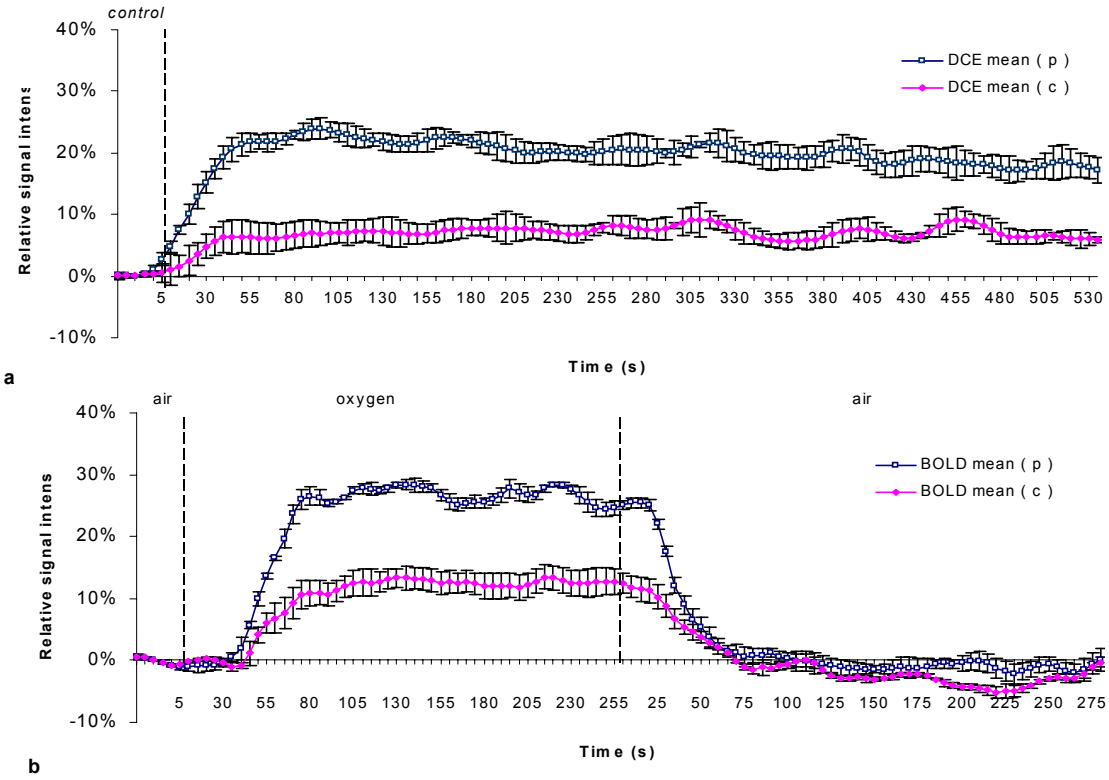

Figure 4.8 Recovery of BOLD and DCE MRI in one AT1 tumor

The mean ^{1}H MR signal intensity in central region (C; filled symbols) and peripheral region (P, open symbols) in response to oxygen inhalation (BOLD) (upper) and Gd-DTPA infusion (DCE) (lower) in one AT1 tumor. It took about 120 s to recover back to baseline after air inhalation in BOLD study.

Histology showed that the undifferentiated AT1 tumor had lower vascular density, less perfusion and more hypoxic regions with more extensive micro-necroses in the center than in peripheral regions (Figure 4.9a). H tumors showed more extensive vasculature, which was generally perfused, less hypoxic and with overall greater homogeneity (Figure 4.9b).

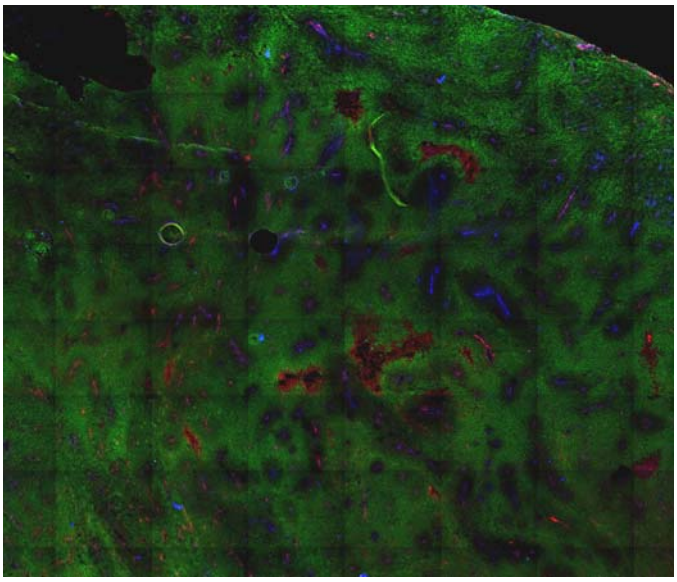

a.

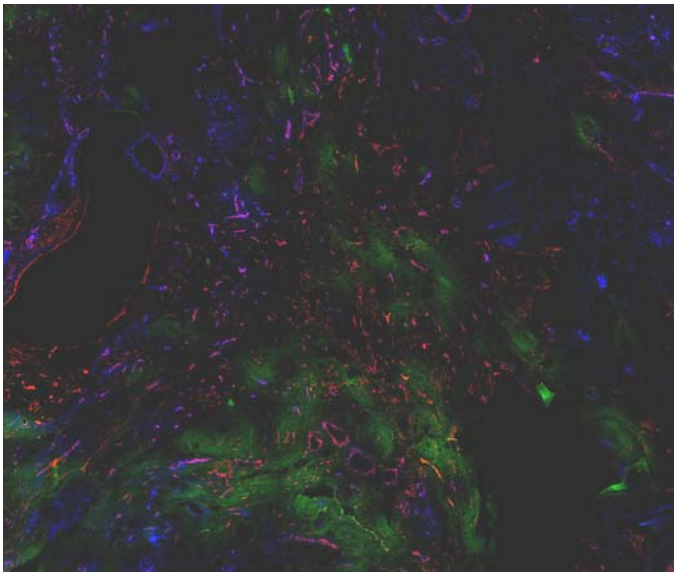

b.

Figure 4-9 Comparison of microvasculature and hypoxia in AT1 and H tumors.

Vascular endothelium marked by CD-31 (red), perfused vessels marked by Hoechst dye 33342 (blue) and hypoxia by pimonidazole hydrochloride (green).

a). The AT1 tumor shows extensive hypoxia and many vessels appeared to be non-perfused. Near the tumor periphery, perfusion is more effective as revealed by the purple appearance of vessels (red overlapping blue). b). The H tumor shows more extensive vascular endothelium, which is well perfused throughout the tumor. Hypoxia occurs distant to perfused vessels and is less extensive.

4.2.4 Discussion

Tumors of both sublines responded to respiratory challenge and Gd-DTPA infusion (Figure 4.3 and 4.4). As expected, the oxygen response was relatively delayed due to transport of oxygen to the rat, then progressively into lungs, blood, and finally tumor. In most cases, the initial kinetic curves for BOLD were similar to DCE after the initial delay, suggesting that each intervention interrogates a similar flow pattern, presumably first-pass through major vessels. After the initial delay, the BOLD response rises to a plateau, whereas DCE peaks and then settles to a lower value.

The peripheral regions of each of these AT1 tumors showed significantly greater and more rapid response to each intervention (Figure 4.5). The marked heterogeneity between center and periphery in AT1 tumors observed here coincides with previous reports based on vascular and metabolic observations (63,82-85). Many H tumors showed the opposite behavior with substantially greater BOLD and DCE response in the center than the periphery, although in some cases there was no significant difference. The magnitude of response is expected to relate to vascular extent and indeed is corroborated by the histology (Figure 4.9). It was previously reported that AT1 tumors are significantly less well oxygenated than size matched H tumors and have significantly greater hypoxic fraction (78). Based on the hot spot method the vascular density of AT1 tumors was significantly lower.

Trying to differentiate tumor types by non-invasive imaging is a goal of many studies. The shape of DCE curves appears valuable in assessing breast cancer (81,86) and response to therapy (87). There appears to be prognostic value for BOLD

response to hyperoxic gas breathing in patients with locally advanced breast cancer undergoing preoperative chemotherapy (chapter 5) (88). Others have shown the feasibility of using a BOLD response to identify chemically induced cholangioma from hepatocellular carcinoma in mice (89). Prostate cancer has often proved a greater challenge due to its multi focal nature. In the clinic Padhani *et al.* (90) found differences using DCE MRI of GD-DTPA between tumor and peripheral zone, but not central gland in patients. There was a weak correlation between tumor stage and vascular permeability assessed, but no significant correlation with Gleason score on PSA levels. Turnbull *et al.* (91) found significant kinetic contrast differences between tumor and fibromuscular benign prostatic hyperplasia. The signal remained modulated for many minutes following Gd-DTPA infusion, whereas the BOLD effect was rapidly reversible. It suggested that the BOLD study could be repeated following a short re-equilibration time.

BOLD MRI can be technically more challenging in the clinical setting, since patients wear a facemask and contrast changes may be much smaller. Nonetheless, Dr. Mason' team has successfully performed studies in normal human volunteers (83), Taylor *et al*.(27) succeeded with four cancer patients and Diergarten *et al*. (92) examined a group of 32 patients finding significantly different signal enhancement between biopsy proven carcinoma of the prostate and the contra lateral normal side.

Meanwhile, several studies have shown differences between prostate tumor types based on dynamic MRI in animal models often noting that macromolecular contrast agents were more effective than small molecules such as Gd-DTPA. Based on the endothelial transfer constant (KPS) Gossman *et al.* (93) could separate the more

aggressive MAT-LyLu from PAP subline of the Dunning prostate R3327 syngeneic rat tumor systems at 1.5 T. Several investigators have worked with tumors in small animals at 4.7 T. Fan *et al.* (94) used spectroscopic imaging to differentiate benign Dunning prostate R3327- AT2.1 from metastatic AT3.1 using the superparamagnetic particulate agent NC100150 (Clariscan), based on image texture, tumor edge morphology and change in T2*. Bhujwalla *et al*. (95) found that metastatic prostate tumors formed vasculature with significantly higher permeability or vascular volume as assessed with albumin-GD-DTPA infusion. Zhao *et al.* have previously investigated the R3327-AT1 and H tumors using NMR oximetry and histology (78). While neither tumor is metastatic, they are characterized by substantially different growth rates (5 vs. 20 days) and levels of cellular differentiation. Both small and large H tumors had significantly higher mean and median pO_2, lower hypoxic fraction (HF_5 and HF_{10}), and better response to breathing hyperoxic gas, as judged by ^{19}F NMR oximetry. Hot spot analysis showed significantly lower vascular density and greater overall pimonidazole uptake in AT1 tumors. This study shows differences in magnitude of both DCE and BOLD responses, but not Kep, provided that tumors were divided into central and peripheral regions (Table 4-2).

It is important to establish tumor characteristics, which can be used to monitor growth and response to therapy. While some authors favor more complex models with three or more compartments, I used a two-compartment model, which is mathematically stable during fitting and for which most clinical experience exists. The quality of the curve-fitting procedure is critical for model-based parametric methods that rely on fitting the data to a complex dynamic curve. For example, the

K_{ep} value is highly influenced by the accuracy of curve fitting algorithm, the blood flow, and the signal intensity curve. If the signal intensity curves of voxels are negative or unstable, the curve fitting fails or results in too high a K_{ep} value. I found that some voxels did not show increased signal during DCE, but the fitting algorithm required that each voxel have a mean value (AUC) greater than zero with DCE contrast. Thus, it was necessary to filter out negative data in calculating K_{ep}. For K_{ep} regression analysis thresh holding criteria were set such that K_{ep} <10 min^{-1}, K_{ep}(error) <5 min^{-1}, and ratio K_{ep}(error)/K_{ep} < 0.8 min^{-1}. Clearly, this issue needs to be further investigated and will markedly depend on the signal/noise ratio and the temporal resolution of the images and also on the model. Here, I found no significant differences between K_{ep} in central and peripheral regions of either tumor type or between tumor types.

Loss of signal accompanying intervention may be rationalized on the basis of a "steal effect" for BOLD investigations, as reported by others (18,28). It is less clear why signal intensity should decrease for extended periods following gadolinium DTPA infusion, though this phenomenon has been reported by Peller *et al*. (18). My MRI pulse sequence was sensitive to both T1 and T2* effects (63). While Gd-DTPA is expected to increase signal by shortening T1, it can reduce the signal by shortening T2*, although I do not believe that local concentrations are sufficient to cause T2* shortening in my investigations. A bolus of Gd-DTPA can cause T2* signal loss, but this would most likely be a transient effect rather than long-term. Magnet or signal drift must be considered, but when a capillary phantom was included it showed

central signal stability better than 5% during Gd-DTPA studies. We also tested infusion of saline and found minimal signal response.

Many investigators have used carbogen rather than oxygen to examine the effects of hyperoxic gas inhalation. Historically, carbogen has been favored in the clinic, since the CO_2 component is vasoactive, minimizing oxygen associated hypotension and potentially increasing blood flow to tumors. Indeed, carbogen is used in the highly successful ARCON clinical trial for head and neck cancer (96). Some investigators reported a differential response to oxygen or carbogen in rodent tumors, notably mouse xenografts (74,97), but studies in Dr. Mason's lab, in general, have shown similar response to either gas on the basis of vascular oxygenation assessed by near infrared (NIR) of ΔHbO_2 (98-100) or *FREDOM* NMR oximetry of pO_2 (101-103). Rates of signal change with BOLD or DCE observed here closely match previous observations using non-localized (global) interrogation of Dunning prostate R3327-AT1 rat tumors by near-infrared spectroscopy with respect to switching gas under similar conditions (104).

Overall, both techniques showed significant differences between the tumor types based on regional analysis and may be relevant to future clinical investigations. Macromolecular contrast agents might prove even more definitive, but they are not yet routinely used in the clinic. BOLD changes were rapidly reversible upon return to air breathing and this could allow rapid assessment of acute response during interventions.

4.3 Breast Cancer Studies

The animal experiment and data analysis were completed by Dr. Dawen Zhao. I helped to develop all data processing software for this research, which has been published.

4.3.1 Introduction

Tumor growth, survival and metastasis depend critically on the development of new blood vessels (105). Therefore, extensive research has focused on developing strategies to attack tumor vasculature (105,106). Tubulin binding agents, e.g., combretastatin A-4-phosphate (CA4P) and ZD6126 represent one kind of vascular targeting agent (VTA) (107,108). Promising preclinical studies have shown that such agents selectively cause tumor vascular shutdown and subsequently trigger a cascade of tumor cell death in experimental tumors (108,109). Although massive necrosis can be induced, tumors usually regrow from a thin viable rim. Thus, a combination of VTAs with additional conventional therapeutic approaches will be required. Indeed, several studies involving the combination of the VTAs with irradiation or chemotherapeutic agents have shown enhanced tumor response (110-114).

To better understand the mode of action, and hence, optimize such combinations, in vivo imaging approaches have been initiated to monitor physiological changes resulting from VTA administration (115-117). Dynamic contrast enhanced (DCE) MRI based on the transport properties of gadolinium-DTPA (Gd-DTPA) is the most commonly used imaging approach to study tumor vascular perfusion and permeability. DCE MRI was included as part of the Phase I clinical trials of CA4P (118,119). Results of preclinical and clinical DCE MRI studies have shown a reversible change in vascular perfusion in the tumor periphery following a single dose

of VTA (120-123). For combination with radiotherapy, measurement of tumor oxygen dynamics will be especially important, since reduced perfusion can induce hypoxia, potentially modulating radiation response. A number of studies have reported improved response when administering VTAs after radiation, while the enhancement was reduced, or lost, if giving VTAs before radiation, implying an increased hypoxia induced by VTAs (110,124). Direct measurements of tissue pO_2 using Eppendorf electrode, conducted by Horsman, *et al*. (125,126), found increased hypoxia 3 h after CA4P or ZD6126. We have developed a method for measuring tumor oxygenation, and dynamics based on ^{19}F NMR echo planar imaging (EPI) following direct intratumoral injection of the reporter molecule hexafluorobenzene (HFB): *FREDOM* (Fluorocarbon Relaxometry using Echo planar imaging for Dynamic Oxygen Mapping) (127,128). This technique provides pO_2 measurements at multiple specific locations simultaneously within a tumor, and reveals dynamic changes at individual locations with respect to interventions. We have previously evaluated tumor oxygen response to various interventions such as hyperoxic gas breathing (80,103). We also had an anecdotal example of pO_2 response to a tumor selective infarcting agent (102). We have now applied both DCE MRI and *FREDOM* to evaluate tumor perfusion/permeability and oxygen dynamics in response to CA4P in conjunction with confirmatory histology.

4.3.2 Methods

Tumor Model

Rat mammary carcinoma 13762NF was implanted syngeneically in a skin pedicle surgically created on the foreback of Fisher 344 adult female rats (n = 25, ~150 g, Harlan), as described in detail previously (129). Nine animals were used for DCE MRI, ten rats for *FREDOM* and six for histological study. Investigations were approved by the Institutional Animal Care and Use Committee.

Drug preparation and dosing

Combretastatin A4 phosphate (CA4P) was provided by OXiGENE, Inc. (Waltham, MA). CA4P was dissolved in 0.9% saline at a concentration of 30 mg/ml before each experiment. A single dose of 30 mg/kg CA4P was chosen in this study because it is considered a clinically relevant dose (120).

MRI experiments

When tumors reached ~ 1 cm diameter (~ 0.6 cm3) MRI was performed using a 4.7 T horizontal bore magnet with a Varian Unity Inova system. Each rat was given ketamine hydrochloride (120 μl; 100 mg/ml, Aveco, Fort Dodge, IA) as a relaxant (i.p.) and maintained under general anesthesia (air and 1% isoflurane (Baxter International Inc., Deerfield, IL)). A 27 G butterfly (Abbott Laboratories, Abbott Park, IL) was placed intraperitoneally for infusion of CA4P or saline alone. For DCE MRI, a tail vein was catheterized using a second 27 G butterfly for contrast agent administration. For oximetry, hexafluorobenzene (50 μl, Lancaster, Gainesville, FL) was injected directly into the tumor along two or three tracks in a single central plane of the tumor, coronal to the rat's body using a Hamilton syringe (Reno, NV) with a custom-made fine sharp needle (32G), as described in detail previously (128). A tunable ($^{1}H/^{19}F$) volume RF coil was placed around the tumor-bearing pedicle. Each

animal was placed on its side in the magnet with no change in position during the whole study, so that individual regions could be tracked. A thermal blanket was used to maintain body temperature.

^{1}H Dynamic contrast enhanced (DCE) MRI

Nine tumor-bearing rats were studied before injection of CA4P (n = 6) or saline alone (n = 3), and 2 and 24 h after treatment. On each occasion, a series of T1-weighted spin echo images (TR= 160 ms, TE= 16 ms, field of view = 40 × 40 mm, matrix = 128 × 128, voxel size = 2.0 × 0.3 × 0.3 mm, total time for 3 slice = 23 s) was acquired before and after a bolus injection of Gd-DTPA-BMA (injection within 1 s; 0.1 mmol/kg, OmniscanTM, Amersham Health Inc., Princeton, NJ) on three 2 mm-thick cross sections parallel to the animal. Data were processed on a voxel-voxel basis using software written by us using IDL 5.6 (Research Systems, Boulder, CO). For each slice, the tumor was separated into regions of center and periphery, respectively. The tumor periphery was taken to be a 1-2 mm thick rim aligned around the whole tumor. Signal intensity versus time curves were plotted and relative signal intensity changes (ΔSI) of each tumor voxel were analyzed using the equation: (ΔSI)=（SI_E-SI_b）/SI_b , where SI_E refers to enhanced signal intensity in the voxel and SI_b is defined as the average of the baseline images. The area under normalized signal intensity-time curve (IAUC) for the first 1.5 min after Gd-DTPA-BMA injection was integrated.

^{19}F Tumor Oximetry - *FREDOM*

A separate cohort of 10 tumors (treated: n = 7; control: n = 3) was used for pO_2 measurements. A single 4 mm slice parallel to the rat body containing the

strongest fluorine signal was chosen for the ^{19}F MRI pO_2 studies. ^{1}H and ^{19}F MR images were acquired using a spin-echo sequence. Overlaying the ^{19}F MR image on the corresponding ^{1}H image revealed the distribution of HFB. Following conventional MRI, tumor oxygenation was estimated on the basis of ^{19}F pulse burst saturation recovery (PBSR) EPI relaxometry of the HFB, as described previously (127). This approach provided pO_2 maps with 1.25 mm in plane resolution and 6-µl voxel size in 6.5 minutes. The spin-lattice relaxation rate [R1 (s-1) = 1/T1] was estimated on a voxel-by-voxel basis using a three-parameter monoexponential function, and pO_2 was estimated using the relationship pO_2 (torr) = (R1 – 0.0835)/0.001876 (127). Prior to CA4P or saline injection, a series of pO_2 maps was acquired with respect to respiratory challenge with oxygen: typically, two baseline measurements, three with oxygen and four upon return to air. Immediately after the last (4th) air measurement, CA4P (30 mg/kg) or saline (0.15 ml) was injected i.p. A further series of pO_2 maps was acquired after 10, 30, 60, 90, and 120 minutes, and then finally another three maps, while breathing oxygen. The 24 h follow-up study comprised two measurements with air and four with oxygen. The oxygen challenge was included to evaluate vascular function.

Markers of vascular perfusion and endothelium

Six animals were used to study the total blood vessels and perfused vessels at pre (n = 2), 2 h (n = 2) and 24 h (n = 2) after CA4P. The blue fluorescent dye Hoechst 33342 (Molecular Probes, Eugene, OR) was injected into the tail vein of anesthetized rats at a concentration of 10 mg/kg in 0.9% saline (0.1 ml) and the tumors were excised 1 min later. Tumor specimens were immediately immersed in liquid nitrogen

and then stored at -80 °C. Immediately after cryostat sectioning (6 μm thick), slices were imaged for Hoechst 33342 under UV wavelength (330-380 nm). Perfused vessels were determined by counting the total number of structures stained by Hoechst 33342 in a minimum of four random fields per section and calculating the mean number of vessels per mm^2. On the following day, the same slices as well as their adjacent slices were immunostained for the endothelial marker, CD31. A primary mouse anti rat CD31 monoclonal antibody (1:20 dilution; Serotec, Raleigh, NC) was added and incubated for 2 h at 37 °C in a humid box. Slides were incubated with Cy3-conjugated goat anti mouse secondary antibody (1:100 dilution; Jackson Immunoresearch Laboratories, West Grove, PA) for 1 h at 37 °C. After mounting with Vectorshield® medium (Vector Laboratories, Burlingame, CA), the slides were observed under red fluorescence (530-550 nm excitation). Image analysis was performed using Metaview software (Universal Imaging Corporation, West Chester, PA). To compare the perfused vessels with the total vessels stained by anti-CD-31, four most vascularized areas in each section (adjacent to the section used day 1) were selected and imaged under red fluorescence. Then, switching to UV wavelength, the perfused vessels stained by Hoechst dye in the same fields were imaged.

Statistical Analysis

Statistical significance was assessed using an Analysis of Variance (ANOVA) on the basis of Fisher's Protected Least Significant Difference (PLSD; Statview, SAS Inst. Inc., Cary, NC) or Student's t-tests.

4.3.3 Results

DCE MRI

Baseline ^{1}H MRI showed stable signal throughout the tumor (not shown). Immediately after a bolus injection of Gd-DTPA-BMA, signal intensity increased significantly, reaching a peak after 23 s ~ 69 s, and then gradually decreasing towards baseline. The maximum signal enhancement averaged over the whole tumor in all 3 slices, ranged from ~ 52% to 85% for the nine tumors.

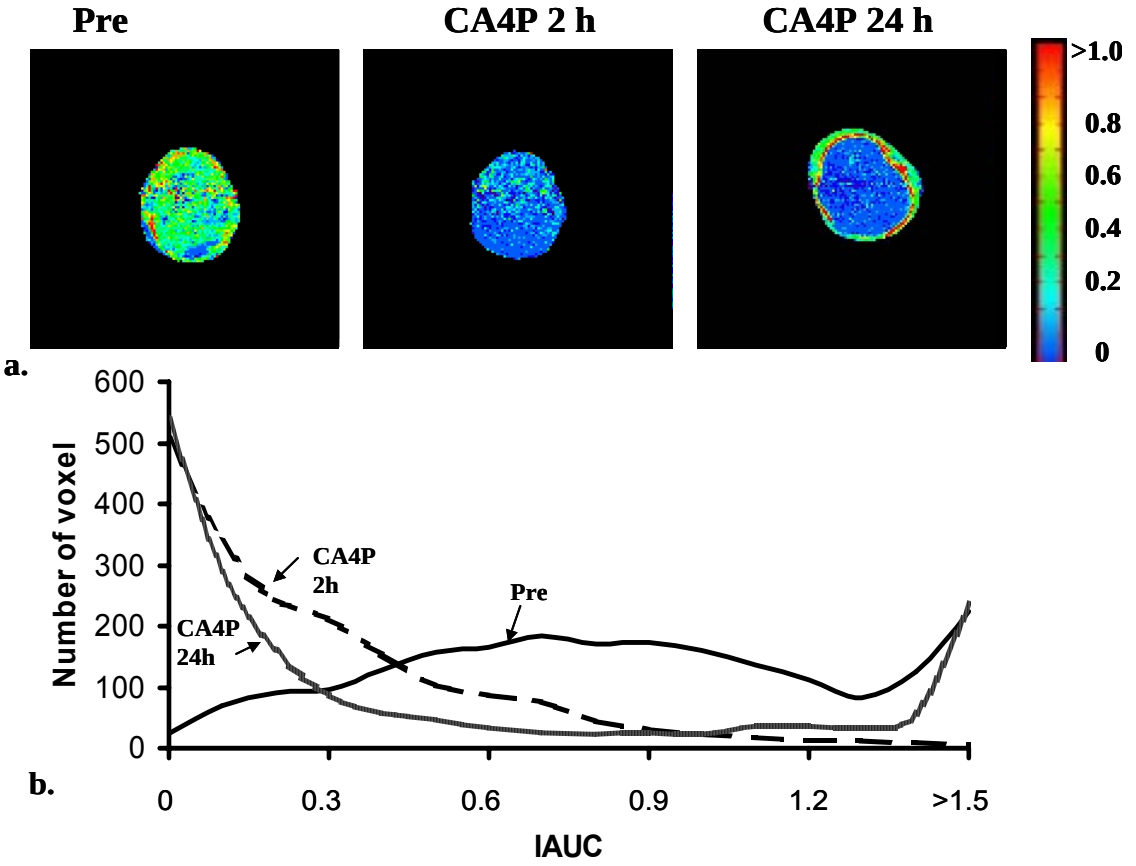

Figure 4.10 DCE MRI with respect to CA4P (30 mg/kg) treatment.
A) Normalized T1-weighted contrast enhanced images were acquired 23 s after a bolus injection of contrast agent pre, and 2 h and 24 h after treatment. Significantly less signal enhancement was observed for the whole tumor region 2 h after treatment. A full recovery was apparent in the tumor rim 24 h post-treatment. B) IAUC frequency of DCE MRI on voxel by voxel basis obtained on the same tumor at pre, 2 h and 24 h after CA4P. Compared with pre, curves of 2 h and 24 h after showed a significant increase in the number of voxels with no signal enhancement (typically IAUC < 0.05). However, the frequency of highly enhancing voxels (IAUC > 1.5) at 24 h recovered to the pre-treatment level

A single dose of CA4P 30 mg/kg caused a dramatic decrease in signal enhancement at the 2 h point, while a 24 h follow-up image showed signal recovery in a thin tumor rim, as shown for a representative tumor (Figure 4.10). Distribution of IAUC frequency showed a distinct shift to the left at both 2 h and 24 h after treatment (Figure 4.10b). The highly enhancing fraction (IAUC > 1.5) at 24 h after CA4P reached the pretreatment level, indicating a complete recovery in the tumor periphery (Figure 4.10b). For all six tumors treated with CA4P, significant decrease in IAUC was observed for the whole tumor region at 2 h: tumor peripheral and central regions reduced by 65% and 70%, respectively ($p < 0.05$; Table 4.3). A complete recovery in IAUC for the tumor periphery was seen 24 h post treatment, while the tumor center remained low (Table 4.3). IAUC frequency data from these 6 tumors also showed a significant increase in the number of non-enhancing voxels (IAUC < 0.05), while the percentage of voxels with IAUC > 0.5 decreased from 55% to 5% 2 h after administration of CA4P ($p < 0.05$, Table 1). In control tumors treated with saline, IAUC was similar at all time points (Table 4.3 and 4.4).

Table 4.3 Normalized IAUC by DCE MRI

Groups		Mean IAUC		
		baseline	2 h	24 h
CA4P (n = 6)	periphery	0.88 ± 0.06	$0.31 \pm 0.08^{*‡}$	0.86 ± 0.06
(30 mg/kg)	center	$0.44 \pm 0.11^{+}$	$0.13 \pm 0.08^{*‡}$	$0.12 \pm 0.05^{*+‡}$
Control (n = 3)	periphery	1.09 ± 0.04	0.93 ± 0.13	0.86 ± 0.05
(saline)	center	$0.52 \pm 0.19^{+}$	$0.46 \pm 0.05^{+}$	$0.44 \pm 0.03^{+}$

IAUC: initial area under signal-intensity curve;

$^{*}p < 0.05$ from baseline; $^{+}p < 0.05$ from periphery; $^{‡}p < 0.05$ from control.

Table 4.4 comparisons of weakly (IAUC<0.05) and strongly (IAUC>0.05) responding voxels with respect to DCE MRI and drug administration

		% of total voxels		
Groups	IAUC	baseline	2 h	24 h
CA4P	< 0.05	16	54^{*+}	41^{*+}
(30 mg/kg)	> 0.5	55	5^{*+}	32^{*+}
Control	< 0.05	14	15	19
(saline)	> 0.5	62	58	51

IAUC: initial area under signal-intensity curve;
Pooled individual voxels (= 10508) from the six tumors were categorized as non-enhancing (IAUC < 0.05) and highly enhancing voxels (IAUV > 0.5).
* $p < 0.01$ from baseline; $^{+}$ $p < 0.05$ from control.

Tumor Oximetry - *FREDOM*

Overlay of ^{19}F on ^{1}H image (Figure 4.11a) confirmed that HFB was distributed in both peripheral and central regions of a central plane of the tumor. In the series of EPI relaxation data sets, typically ~40-100 voxels provided an R1 fit, and potential pO_2 value. Since noise may give an apparent relaxation curve (R1) fit, data were selected by applying thresholds of T1 error < 2.5 s and ratio T1 error/T1 < 50%. Only those voxels, which provided consistently reliable data throughout the time course, were included for further analysis. As an example (Figure 4.11b) 25 voxels qualified for all these prerequisites and could be followed through the 17 measurements from baseline to 2 h post CA4P. At 24 h 31 voxels were traceable through the 6 measurements with respiratory challenge. As expected, based on the distribution of HFB (Figure 4.11a), each pO_2 map (Figure 4.11b) comprised two distinct groups of voxels, representing the peripheral and central locations of HFB, respectively. Variations of mean pO_2 with respect to intervention for these two groups of voxels are presented separately in Figure 4.11c.

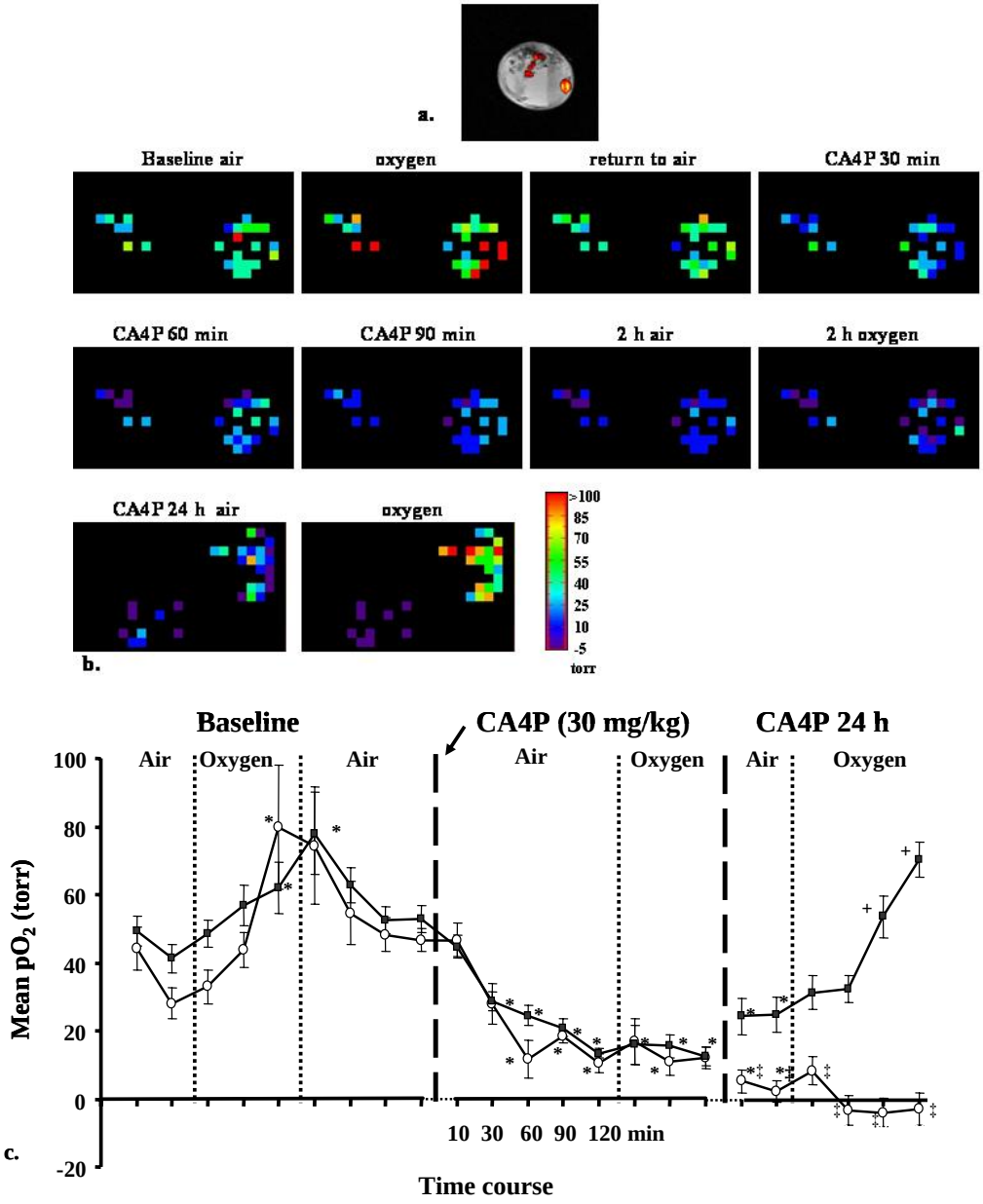

Figure 4.11 tumor oxygenation dynamic measurement

a) Distribution of hexafluorobenzene (HFB) in a representative tumor (no. 4 in Table 2). An overlay of ^{19}F signal density on the anatomic image indicates HFB in both peripheral and central regions. b) pO_2 maps obtained from the same tumor comprise two separated groups of voxels, which correspond to the locations of HFB on the anatomic image. Twenty five individual voxels were traceable from the pretreated baseline to 2 h after CA4P with oxygen breathing. Thirty one voxels could be followed 24 h post-treatment. Significant decrease in pO_2 was evident for all the individual voxels after CA4P, and pO_2 did not respond to oxygen inhalation after 2 h. The 24 h maps showed improved pO_2 and significant response to oxygen breathing in the peripheral region (right), but not in the central region (left). c) Mean pO_2 curves are shown for the peripheral (■) and central (○) voxels of this tumor. * $p < 0.05$ from baseline air, $^{+}p < 0.05$ from 24 h air, $^{‡}p < 0.05$ from periphery.

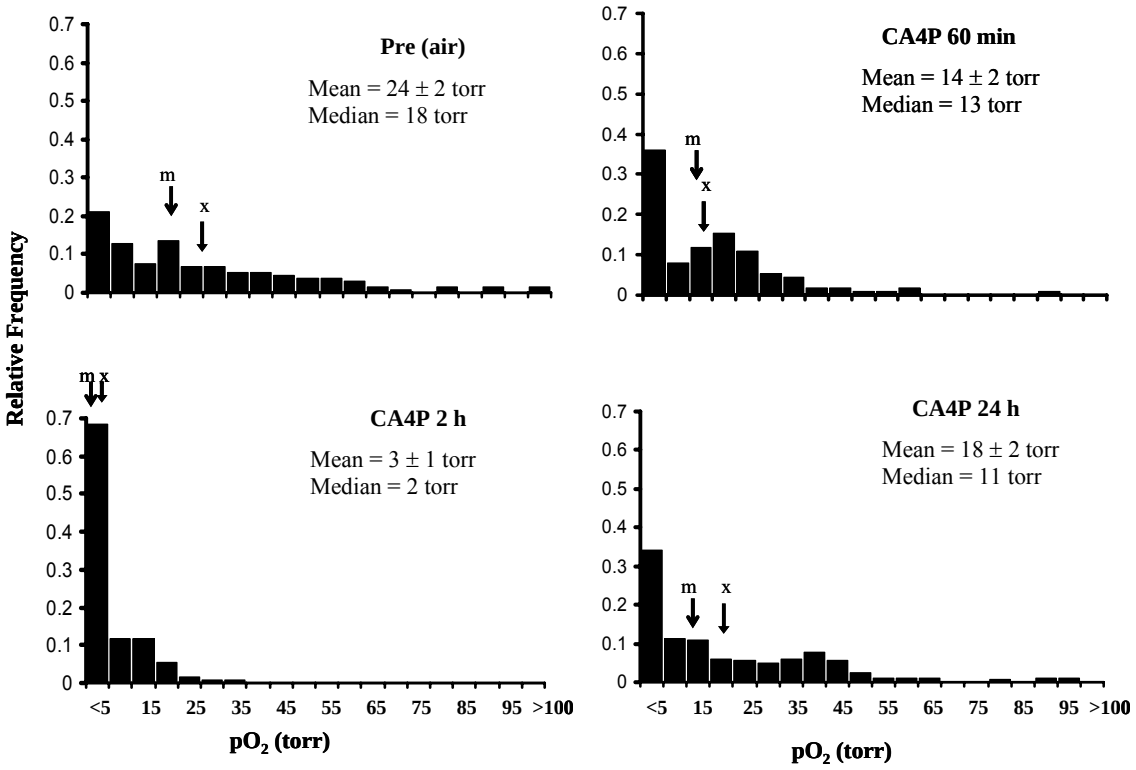

Figure 4.12 pO_2 histograms based on relative numbers of voxels in the seven tumors, showing left shift post CA4P. Ordinate ranges, *e.g.*, 10 refers to 5 torr ≤ pO_2 < 10 torr. x: mean; m: median.

Table 4.5 Tumor oxygen dynamics assessed by ^{19}F MRI with respect to CA4P treatment

Groups	Case no.	Size cm^3	pO_2 (mean ± se torr)							
			baseline	Time course						
			Air	30 min	60 min	90 min	2 h	oxygen	24 h base	oxygen
CA4P (30 mg/kg) (n=7)	1	2.0	36 ± 1	NA	NA	NA	2 ± 3*	5 ± 2*	NA	NA
	2	0.9	12 ± 2	NA	NA	NA	-3 ± 2*	-3 ± 2*	NA	NA
	3	1.2	13 ± 0	35 ± 11	11 ± 3	9 ± 4	1 ± 2*	2 ± 2*	5 ± 0*	30 ± 6+
	4	0.7	43 ± 5	29 ± 3*	21 ± 3*	20 ± 2*	13 ± 1*	16 ± 5*	20 ± 2*	48 ± 7+
	5	0.4	12 ± 2	5 ± 3*	9 ± 3	4 ± 2*	2 ± 1*	7 ± 3*	NA	NA
	6	0.7	15 ± 1	19 ± 3	9 ± 2*	4 ± 2*	1 ± 2*	0 ± 3*	12 ± 1	73 ± 12+
	7	0.3	28 ± 6	29 ± 2	16 ± 4	6 ± 2*	1 ± 1*	7 ± 2*	23 ± 2*	79 ± 6+
	Mean	0.9 ± 0.2	23 ± 5	23 ± 13	13 ± 5	9 ± 3*	2 ± 2*	5 ± 3*	15 ± 4	58 ± 11+
Saline (n=3)	8	0.6	34 ± 2	47 ± 5	40 ± 5	36 ± 10	31 ± 8	88 ± 10*	37 ± 0	86 ± 5+
	9	0.2	47 ± 2	62 ± 8	65 ± 6	64 ± 5	61 ± 4	114 ± 8*	67 ± 1	159 ± 7+
	10	0.6	13 ± 1	16 ± 6	10 ± 4	9 ± 4	12 ± 6	35 ± 10*	14 ± 1	78 ± 15+
	Mean	0.5 ± 0.1	31 ± 10	42 ± 14	38 ± 16	36 ± 16	35 ± 14	79 ± 23*	39 ± 15	108 ± 26+

* $p < 0.05$ from baseline; + $p < 0.05$ from 24 h air (24 h after injection of CA4P); NA: no measurement.

Before CA4P administration, the mean pO_2 was 45 torr in the tumor periphery and 36 torr in the center during air breathing. Both regions responded significantly to oxygen breathing ($p < 0.05$) and this was reversed upon return to air breathing. A significant decrease in pO_2 was detected as early as 30 min after CA4P administration in the tumor periphery, and by 60 min in the center ($p < 0.05$). The decline continued with the lowest pO_2 values (13 torr and 10 torr, respectively) at the 2 h point. At this time, oxygen challenge no longer produced an increase in pO_2 for either region. Twenty-four hours later, the peripheral pO_2 had increased significantly (24 torr), but was still significantly lower than the pretreatment value ($p < 0.05$). After 24 h, pO_2 again responded significantly to breathing oxygen in the tumor periphery ($p<0.01$). However, pO_2 in the central regions (4 torr) was even lower at 24 h than 2 h, and did not respond to oxygen breathing. Histograms of pooled voxels assessed for the 7 tumors showed significantly decreased pO_2 at 1 h, 2 h and 24 h after treatment ($p < 0.01$). The hypoxic fraction less than 5 torr (HF_5) increased significantly from a pretreatment value of 20% to 36% at 1 h and 68% at 2 h, but was only 32% at 24 h (Figure 4.12). For the 7 treated tumors, two tumors showed significant decrease in pO_2 as early as 30 min after treatment ($p < 0.05$). Significant decrease in the mean pO_2 for the group was found at 90 min after CA4P (23 ± 5 vs. 9 ± 3 torr; $p < 0.05$) and a further decrease at 2 h (2 ± 2 torr; Table 2). The mean pO_2 increased significantly to 15 ± 4 torr at 24 h, compared to 2 h ($p < 0.05$). For the control tumors, no significant differences in pO_2 were found between any of the measurements (pre, 2 h or 24 h post).

Histology and Immunohistochemistry

Perfused vessels marked by Hoechst 33342 and correlation with the total vessels labeled by anti-CD31 at pre, 2 h and 24 h after CA4P are shown in Figure 4.13. A significant decrease in the number of perfused vessels was evident at 2 h (21 ± 6/mm2 vs. 145 ± 23/mm2 (pre), $p < 0.01$), followed by recovered perfusion at 24 h (114 ± 19/mm2).

4.3.4 Discussion

In common with previous reports in the literature, combretastatin A4 phosphate caused a significant reduction in tumor perfusion within 2 h. DCE MRI showed that IAUC in the tumor periphery was reduced 70% 2 h after a single dose of CA4P (30 mg/kg), followed by a full recovery by 24 h. However, the drop in IAUC of the tumor center was not reversible (Table 4.3). IAUC reflects tumor blood flow, vascular permeability and a fraction of interstitial space. Histological data using the perfusion marker, Hoechst 33342, confirmed a significant decrease in perfused vessels 2 h after CA4P, while there was recovery evident at 24 h (Figure 4.13).

Vascular shut down induced by VTA is expected to decrease tumor pO_2. Horsman, *et al* (126). recently reported that tumor pO_2, measured by Eppendorf electrode, decreased significantly 3 h after ZD6126. In line with that study, ^{19}F MRI oximetry showed that CA4P caused significant decrease in pO_2 within 90 min and a further reduction within 2 h. As for perfusion, pO_2 recovered towards pretreatment levels after 24 h in the tumor periphery.

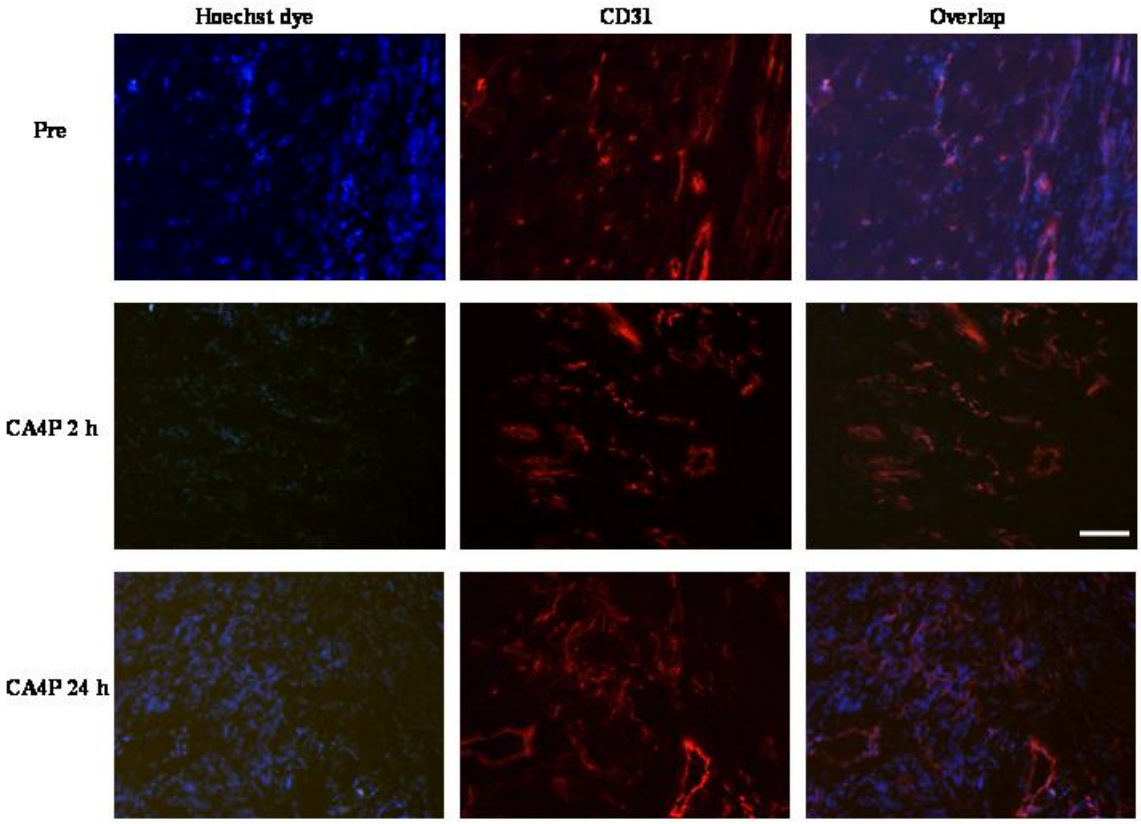

Figure 4.13 comparison of immunohistochemistry results
Perfusion marker Hoechst staining pre, 2 h, and 24 h post CA4P (left). Vascular endothelium of the same field was immunostained by anti-CD31 (red, middle). A good match (right) between Hoechst and anti-CD31 stained vascular endothelium was found in the pretreated tumor. Two hours after treatment, significant reduction in perfused vessels was detected, followed by a recovery at 24 h point. Bar = 100 μm.

Although VTAs cause vascular shut down and lead to extensive hemorrhagic tumor necrosis, rapid tumor regrowth occurs from the surviving rim. Many preclinical studies have shown that a single dose of VTA is associated with very little tumor growth delay (108,109,126). Thus, a combination with other therapeutic modalities, e.g., radiotherapy and conventional chemotherapy will be needed to achieve complete control. The rationale for such combinations is that VTAs target the poorly perfused

and relatively hypoxic regions of the central tumor, while a conventional therapy is applied to attack the relatively better oxygenated, highly proliferating rim. A critical issue regarding such combinations is timing and sequencing of the agents. Thus, a primary goal of this study was to monitor longitudinal pO_2 changes after CA4P, to facilitate and potentially optimize such combinations. Others have demonstrated enhanced therapeutic efficacy by combining CA4P, ZD6126, or 5,6-dimethylxanthenone-4-acetic acid (DMXAA) with radiotherapy (79,124), radioimmunotherapy (130) or chemotherapy (112). In the study of combined ZD6126 with irradiation, Siemann *et al*. (110) reported increased tumor cell kill by administering drug immediately (30 min ~ 1 h) after a single dose of radiation, compared with administering the drug 24 h or 1 h before. This observation coincides with our present findings that tumor pO_2 declined 1 h after drug administration and did not recover fully at 24 h (Figure 4.11c).

Oxygen challenge pre- and post-treatment was used to compare vascular function in this study. In common with our previous observations (131,132), oxygen breathing significantly increased tumor oxygenation in mammary carcinoma 13762NF under control conditions (Figure 4.11, Table 2). The pO_2 response to CA4P was equally effective in peripheral and central regions through 2 h post administration (Figure 4.11c). pO_2 decreased in both regions within 30 min and continued to decrease for 2 h. Differential behavior with respect to oxygen challenge between the peripheral and central tumor regions was observed only after 24 h. At 24 h pO_2 in the tumor center was even lower than the pretreatment baseline or the 2 h level, and showed no response to oxygen inhalation (Figure 4.11). However, oxygen breathing produced a

significant increase in pO_2 of the peripheral region even though the pO_2 was significantly lower than pretreatment (Figure 4.11). These observations provide further evidence that CA4P at 30 mg/kg induced irreversible vascular damage in the tumor center, while peripheral vessels survived and were functional by 24 h. One would expect that hypoxia modifiers, e.g., oxygen breathing, if given 24 h after CA4P, might improve tumor radiosensitivity.

Hypoxia in solid tumors has been widely recognized as a potent factor, which leads to resistance to radiotherapy and some anticancer drugs (133). Recently, there is increasing evidence that tumor malignant progression may be associated with a hypoxic microenvironment (134,135). Given the importance of oxygen, many techniques for monitoring pO_2 have been developed (128,136). While each method has specific attributes, many are highly invasive, and impractical for longitudinal studies of specific regions of interest. The Eppendorf has been considered a 'gold standard' for pO_2 measurement, but it is not suitable for a longitudinal study of the type reported here. In vivo proton MRI, e.g., Dynamic contrast enhanced (DCE) MRI and Blood oxygen level dependent (BOLD) MRI, provide non-invasive approaches to assess tumor vasculature, particularly, useful in response to interventions, but neither DCE nor BOLD MRI provides a straightforward correlation with pO_2 (31,137). *FREDOM* not only provides pO_2 values simultaneously at multiple specific locations within a tumor, but also reveals dynamic changes at individual locations with respect to interventions.

Central necrosis develops in 13762NF tumors even at small size and becomes substantial when tumors become bigger, which has been confirmed previously by

histology (132). In some of the tumors used in this study, a low-intensity central region was observed in T1-weighted images, where there was little enhancement after infusion of contrast agent. After treatment with CA4P, the area of these regions of low signal intensity increased slightly (data not shown). A similar observation was reported by Beauregard, *et al* (138) in human colon carcinoma xenograft. In common with our previous study of 13762NF tumors (131,132), we found considerable intra-tumoral heterogeneity in the distribution of pO_2 values, ranging from hypoxic to well oxygenated. In comparison with our previous data on 13762NF tumors, we found average baseline pO_2 values were lower in the present study (mean 25 torr vs. 63 torr). This difference likely resulted from an altered anesthesia protocol, since we now use a baseline of air/isoflurane, as opposed to 33% oxygen in nitrous oxide with metafane (132). However, oxygen challenge produced remarkably similar extent of increase in pO_2 values observed in both studies (72 torr vs. 73 torr).

Previous studies showed little macroscopic redistribution of HFB over a period of hours (139), but it does clear from the tumors with a typical half-life about 600 min (140). The clearance of HFB normally precludes chronic long term studies of oxygenation, unless further doses of HFB are administered. Indeed, for all the 3 control tumors in this study, additional HFB (50 μl) was required for the 24 h follow-up study. However, no additional HFB was required for studies 24 h following CA4P, presumably due to vascular shutdown.

These results provide the first insight into regional tumor oxygen dynamics in response to CA4P in a syngeneic rat tumor. There is a distinct similarity between the results of the pO_2 measurements and the more traditional DCE, but the quantitative

pO_2 values provide the potential for exploiting synergy with other oxygen dependent therapies. The observations further demonstrate the value of *FREDOM* in assessing dynamic changes in regional tumor pO_2 in vivo in response to intervention. We believe that dynamic measurements are particularly valuable for understanding as mode of action of therapeutic response to VTAs. Most significantly, these measurements lay a foundation to optimize the timing of combination therapy involving fractionated radiotherapy and multiple doses of VTAs.

CHAPTER 5

BOLD for Early Assessment of Breast Cancer Chemotherapy

5.1 Introduction

Tumor microcirculation and oxygenation play critical roles in tumor growth and responsiveness to cytotoxic treatment and radiotherapy, which affect drug delivery, metastatic spread and hypoxia. These characteristics may provide prognostic indicators for cancer therapy and / or early evaluation of tumor therapeutic efficacy. Tumor oxygenation status is determined by oxygen consumption rate of tumor cells and oxygen supply to tumor tissue (7). Previous studies show tumors have highly abnormal, distended capillaries with leaky endothelial linings and sluggish blood flow compared with normal tissue (141). Oxygen supply to the tumor is limited by local structural and functional abnormalities in the tumor microcirculation including the transient nature of perfusion and no-perfusion vessels within a tumor, often resulting in perfusion-limited oxygen supply (6,69,142). The size and geometry of the tumor in relation to its functional microvascular architecture frequently leads to diffusion-limited oxygen delivery to tumor tissue that is distal from the blood vessels (143). Both mechanisms underlying hypoxia contribute to the main characteristics of tumor.

The oxygenation status of cancer cells was shown to affect the outcome of radiotherapy, with more oxygenated cells being more radiosensitive in 1953 (144). Since then, considerable research has been carried out on tumor hypoxia. Studies have shown that tumor hypoxia is associated with resistance to some chemotherapy (141). The measurement of tumor oxygenation is becoming more and more

important. If one could measure the oxygenation status of an individual tumor, it might provide better prognostic information for treatment outcome and be able to match the therapeutic planning to the patient. Dr. Mason's group developed the new approach (*FREDOM*) for measuring oxygen partial pressure using MRI, which has been successfully used to monitor dynamic changes in animal tumor oxygenation (78,80,84,145).

Early assessment of cancer therapeutic response during the treatment is very important in clinical practice. Generally, mammography and ultrasound are used to evaluate chemotherapy showing anatomic information of tumor and surrounding normal tissue. With development of PET, SPECT and MRI techniques, it is possible to image tumor functional information, such as vascular function (permeability), cancer cell metabolic rate, tumor perfusion and hypoxia (146-149). Based on functional changes of tumor, they may provide better evaluation of tumor therapeutic response. However, it remains a major challenge in clinical practice.

As a noninvasive approach, Dynamic Contrast-Enhanced (DCE) MRI has been widely used for cancer diagnosis based on extrinsic agent (Gd-DTPA) leak into EES (Extracellar Extravascular Space) causing local T1 shortening and MRI signal increase (13). Previous studies showed that DCE MRI signal is related to tumor vasculature and its permeability (13,72,150). BOLD MRI has been used to study human tumors with carbogen (conventionally 95%O_2 and 5% CO_2) inhalation (50,75). The studies showed BOLD responses in human tumors (head and neck cancers, breast cancer, prostate cancer, etc.). Deoxyhemoglobin ($dHbO_2$) can serve as an endogenous contrast agent causing signal loss in echo planar MR images.

Interventions improving tumor vascular oxygenation, which convert $dHbO_2$ to HbO_2 are expected to produce signal gain. The BOLD effect is also sensitive to changes in blood flow and vascular volume.

The aim of this work was to investigate and compare the extrinsic contrast agent, Gd-DTPA, and the intrinsic contrast agent, deoxyhemoglobin, for early evaluation of breast cancer chemotherapy in order to explore the potential application of BOLD for evaluating breast cancer therapy in the clinic setting.

5.2 Materials and Methods

Totally eleven patients with locally advanced breast cancer attended this clinical research. One patient failed due to motion on all occasions; one patient gave up study, two patients did not finish their therapy. Seven patients finished all chemotherapy and studies including BOLD and DCE MRI, mammography, and biopsy. My clinical data analysis was based on these seven patients. The mean age of these patients was 50.6 years (range: 40-62); four of them were left side and three were right side. The mean initial tumor size was larger than 3 cm.

Chemotherapy protocols

Locally advanced breast cancer was treated with standard preoperative chemotherapy consisting of doxorubicin and cyclophosphamide for four cycles every 2 or 3 weeks. The patients received i.v. injection dose in each cycle (Figure 5.1).

MRI protocols

MRI was performed on a 1.5 T clinical scanner (Philips Intera). A fat suppressed EPI pulse sequence was used for the BOLD study (Figure 5.2). For BOLD MRI

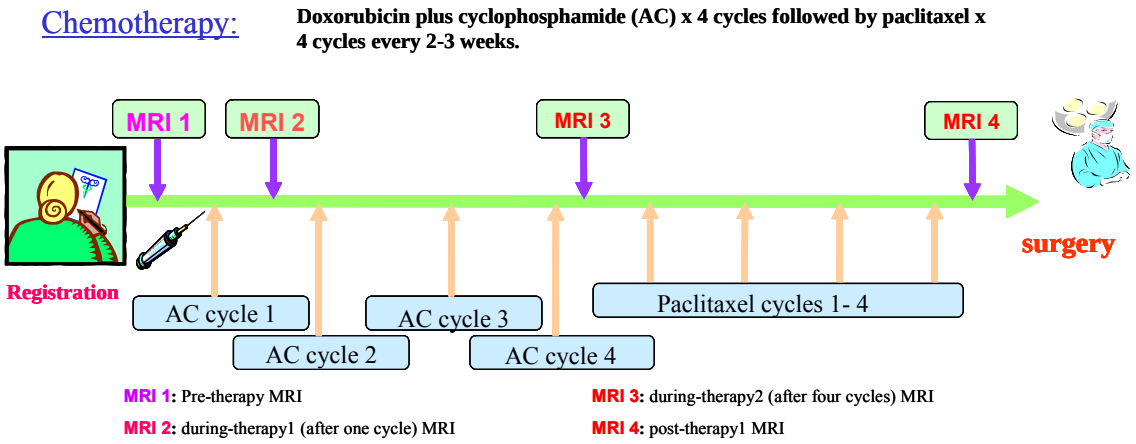

Figure 5.1 The protocol of patient chemotherapy and MRI study

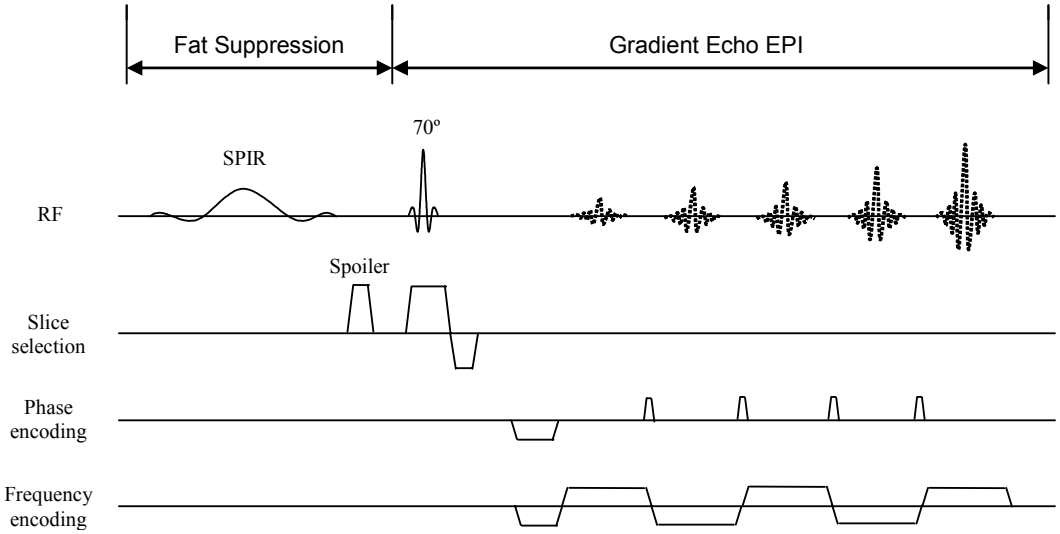

Figure 5.2 The diagram of BOLD pulse sequence

(TR/TE = 500/41.4 ms; FOV 20 cm; acquisition matrix size= 256×256; thickness 5mm) patients breathed room air via a face mask for 45 s, to establish a baseline value, then oxygen (8 liters/min.) for 6 min and finally room air again. The fat suppressed pulse sequence was used in DCE study. For DCE (TR/TE =32.9/6.5 ms; FOV 20 cm; reconstruction matrix size= 256×256; thickness 2 mm) the patient

breathed room air with imaging performed prior to and every 2 mins after bolus IV Gd-DTPA (Omniscan™, 0.1 mmol/kg) (Figure 5.3).

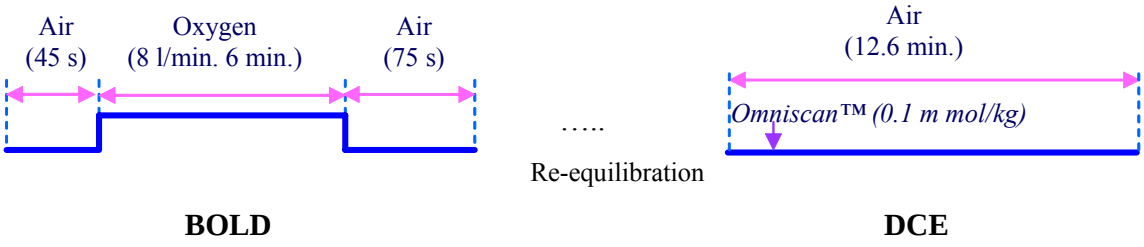

Figure 5.3 Diagram of the BOLD and DCE measurement

MRI exams were performed three or four times with the same parameters and the same position and named MRI 1, MRI 2, MRI 3 and MRI 4, respectively. MRI 1 was before chemotherapy; MRI 2 was after one cycle of chemotherapy; MRI 3 after four cycles of chemotherapy. Generally, after the first four cycles' chemotherapy each patient was evaluated clinically to determine whether they continue for another four cycles of chemotherapy or undergo surgery. If patient continued for another round of chemotherapy, the patient was measured by MRI again (MRI 4) (Figure 5.1). This study was approved by IRB.

Monitor SaO_2 and heart pulse rate

Figure 5.4 The MRI compatible pulse oximeter (Nonin® 8604FO)

Patient blood oxygenation saturation and pulse rate were monitored using a Nonin® 8604FO MRI Compatible Pulse Oximeter (Figure 5.4). Measurements were performed 2 or 3 times during initial air breathing, 3 or 4 during oxygen and again twice upon return to air. The data were analyzed and presented as the mean ± S.D.

Data analysis

Data analysis was performed on a voxel-by-voxel basis with the tumor region selected by intensity threshold.

The relative signal intensity (ΔSI) of each tumor voxel was analyzed using the equation:

$$(\Delta SI) = \frac{(SI_E - SI_b)}{SI_b} \times 100\% \qquad (5\text{-}1)$$

where SI_E refers to the enhanced signal intensity in the voxel and SI_b is defined as the average of the baseline images. The area under the normalized signal intensity-time curve (AUC) for the BOLD and DCE intervention was integrated. Each voxel was used for histogram analysis.

A region of interest (ROI) was used to do permeability K_{ep} analysis for DCE data. Contrast enhancement was quantified using the Brix two-compartment model (81) to assess the vascular permeability, K_{ep}. For a bolus injection:

$$\frac{SI_E}{SI_0} = 1 + A^H \cdot K_{ep}\left(\frac{e^{-K_{ep}\,t} - e^{-K_{el}\,t}}{K_{el} - K_{ep}}\right) \qquad (5\text{-}2)$$

where A^H is a parameter that depends on properties of the tissue, the MR sequence, and the infusion rate; SI_E is signal intensity after injection of contrast agent; SI_0 is the signal intensity before injection; K_{ep} is the rate constant between

extravascular extracellular space (EES) and plasma, which is effected by microvascular permeability; K_{el} is the elimination rate of tracer from the central compartment. The fitting result was filtered by requiring Kep<10 $min^{-1}$and Kep error <5 min^{-1}.

Statistics

All results are presented as mean ± s.d. Comparisons between the groups were performed using an Analysis of Variance (ANOVA) with significance set at p< 0.001 (Statview, SAS, Carey, NC). Chi-square testing was used compare the therapeutic response & enhancement with significance set at p<0.05 (Statview, SAS, Carey, NC).

5.3 Results

1. Tumor region identification

By using the fat suppressed technique both the DCE and BOLD showed the same bright region (tumor) (Figure 5.5). The tumor region showed high intensity (bright) and the normal tissue showed relative low intensity (dark) in the original images.

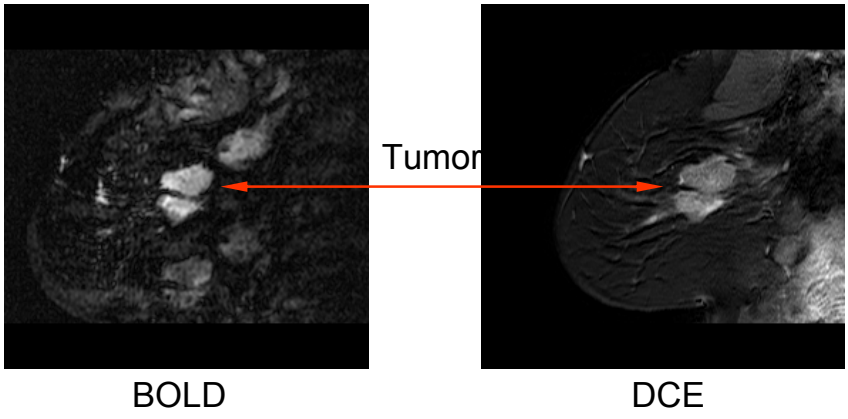

Figure 5.5 Breast cancer BOLD and DCE images

Based on the signal intensity of the whole dynamic scan, the intensity curve of tumor and normal tissue showed very different behavior (Figure 5.6 and 5.7). In the raw BOLD image, the intensity of tumor region was three times higher than that in normal tissue (160 v 40) (Figure 5.6). After oxygen inhalation, there were a big change in the tumor region (~20) and a small change in normal tissue (<5). It indicated that the change of blood oxygenation in tumor region was higher than that in normal tissue. The DCE images showed the range of enhancement in tumor region was about190, while the range of enhancement in normal tissue region was 6 (Figure 5.7). The big enhancement in tumor region demonstrated the high vascular permeability in this region. Both images showed the enhancement in the same region.

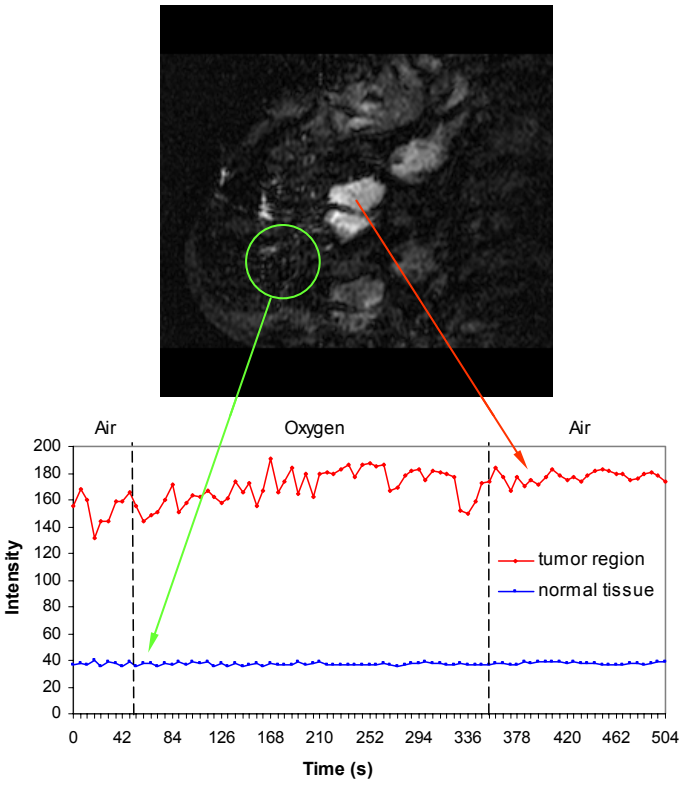

Figure 5.6 The BOLD intensity dynamic change in tumor and normal regions

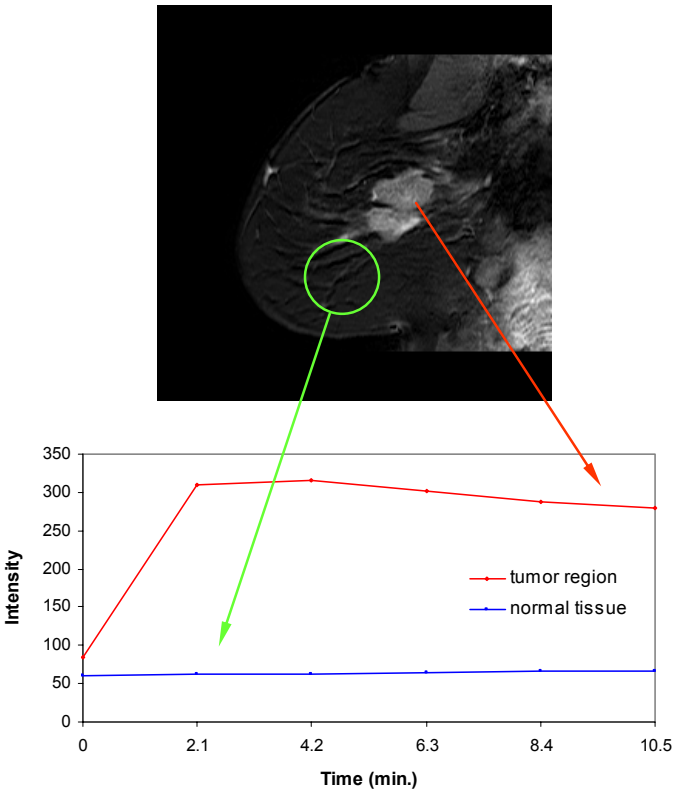

Figure 5.7 The DCE intensity dynamic changes in the tumor and normal regions

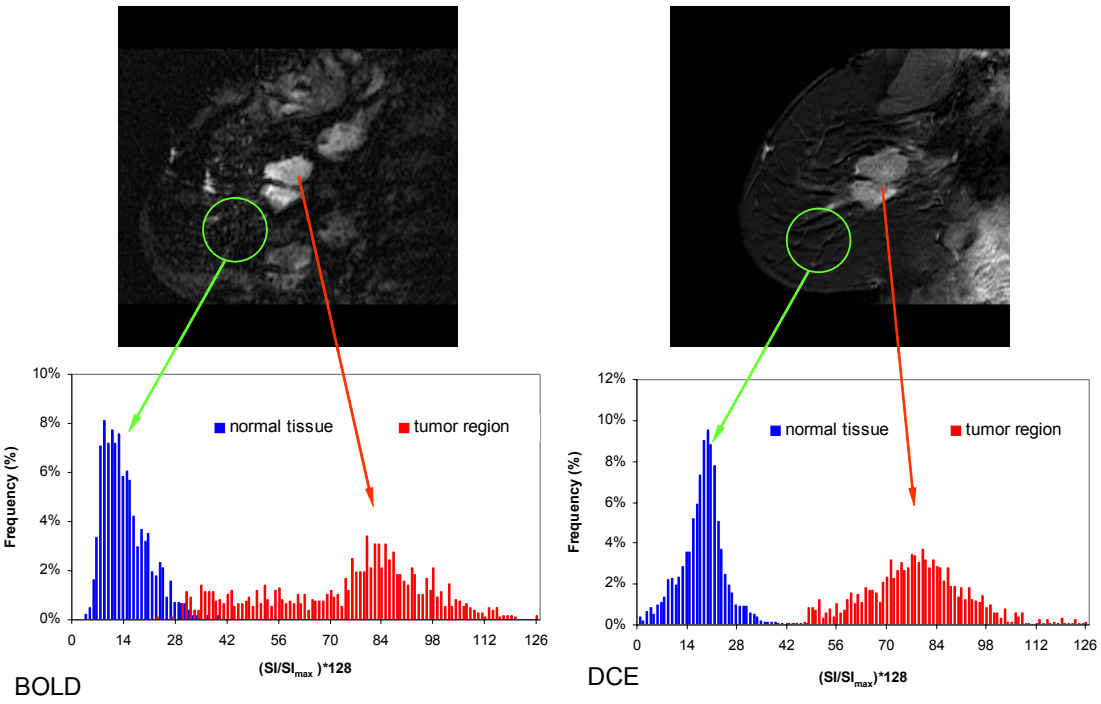

Figure 5.8 The histogram of cancer region and normal tissue for classification

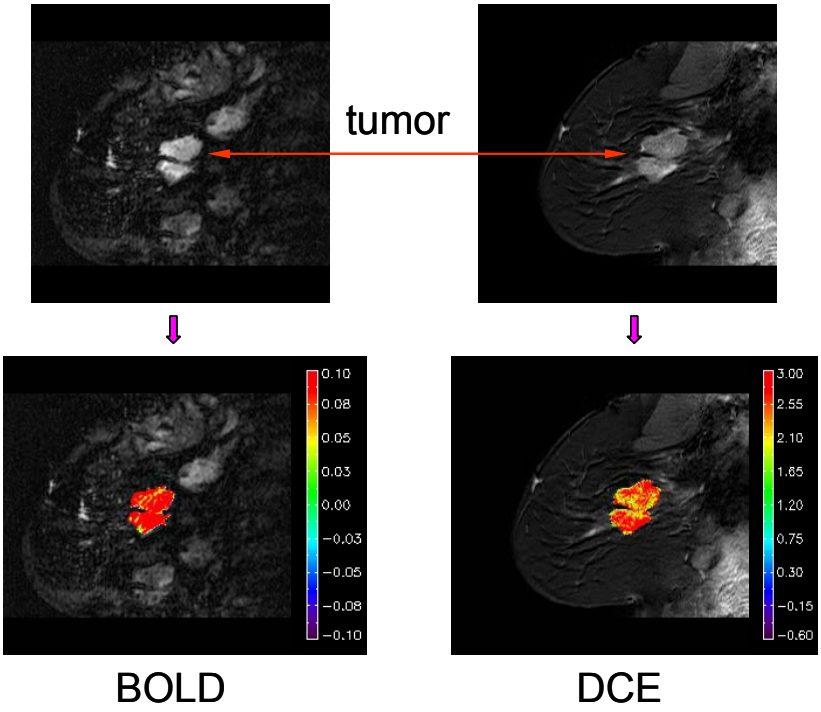

Figure 5.9 The identified tumor region from BOLD and DCE images

Dr. Weatherall, a clinical radiologist, confirmed the tumor location in images. During analysis, a small variation in normal tissue might cause a big change of relative signal intensity and false information. It was necessary to identify and only analyze the tumor region during data processing. The histogram analysis showed a clear line between tumor region and normal tissue for classification (Figure 5.8). By threshold processing, it was easy to define the tumor region in BOLD and DCE images (Figure 5.9). Further data processing was only based on the tumor region.

2. DCE MRI response to chemotherapy

DCE MRI showed a greater contrast enhancement in the tumor region (Figure 5.10). These contour images show the DCE response to chemotherapy. The high enhancement region decreased with the therapy.

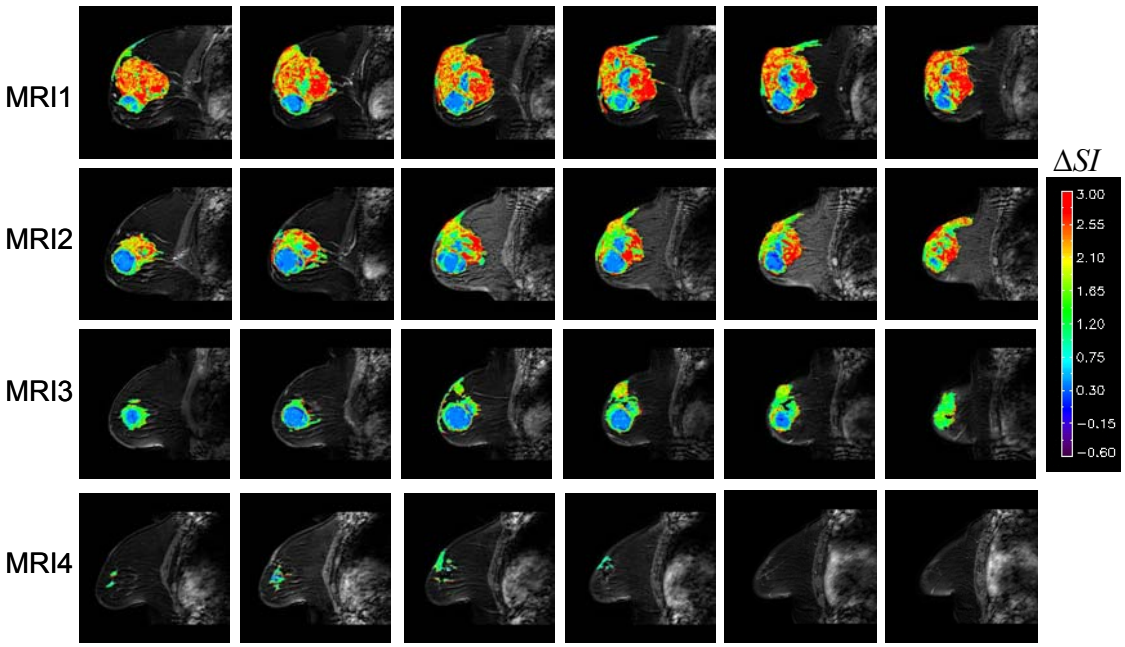

Figure 5.10 DCE MRI response to chemotherapy in one patient (#7)

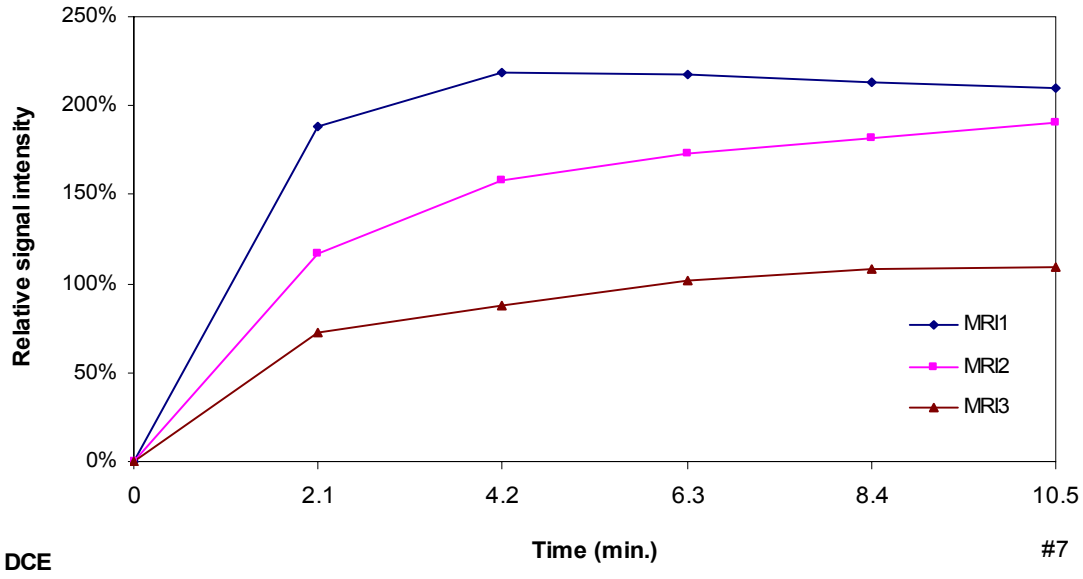

Figure 5.11 Comparison of DCE enhancement with treatment in patient #7

With treatment, the DCE enhancement of this patient decreased (Figure 5.11). Comparison of differential chemotherapy response to DCE enhancement, showed

no obvious correlation between high DCE enhancement and good treatment outcome (Table 5.1).

Table 5.1 The relationship between DCE enhancement and therapeutic efficacy

Patient	Age (yr)	Tumor Size(cm)	Initial response *ΔSI (%)*				chemotherapy response
			MRI 1	MRI 2	MRI 3	MRI 4	
1	61	11	432	308	161	112	5.3 cm, PR
2	62	5	333	429	77	27	Non-palpable, CR
4	51	5	282	376			Non-palpable, CR
5	47	8	206	174	184	76	6.0 cm, stable
6	44	4.5	73	54		17	4.5 cm, stable
7	39	8	210	164	96	133	2.5 cm, PR
8	49	7	143	140	24	19	Non-palpable, CR

Stable = less that 30% decrease in tumor size
PR = partial response (greater than 30% decrease in tumor size)
CR= complete response

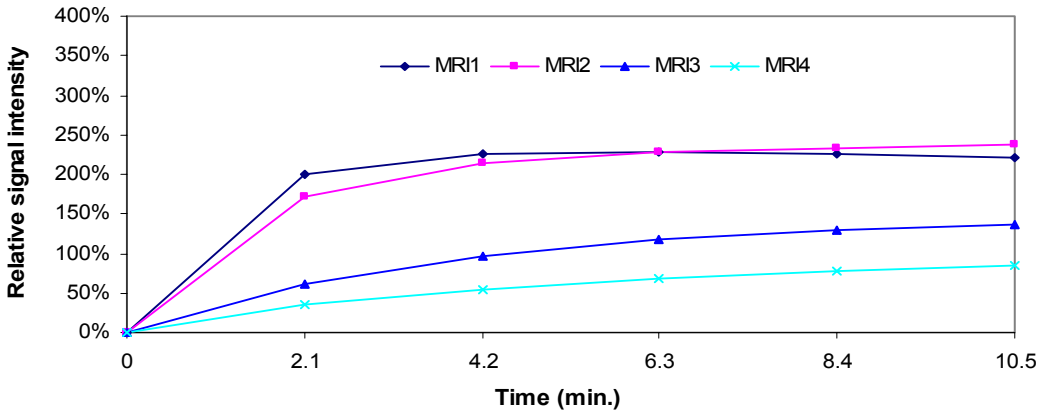

Figure 5.12 DCE responses to treatment in seven patients

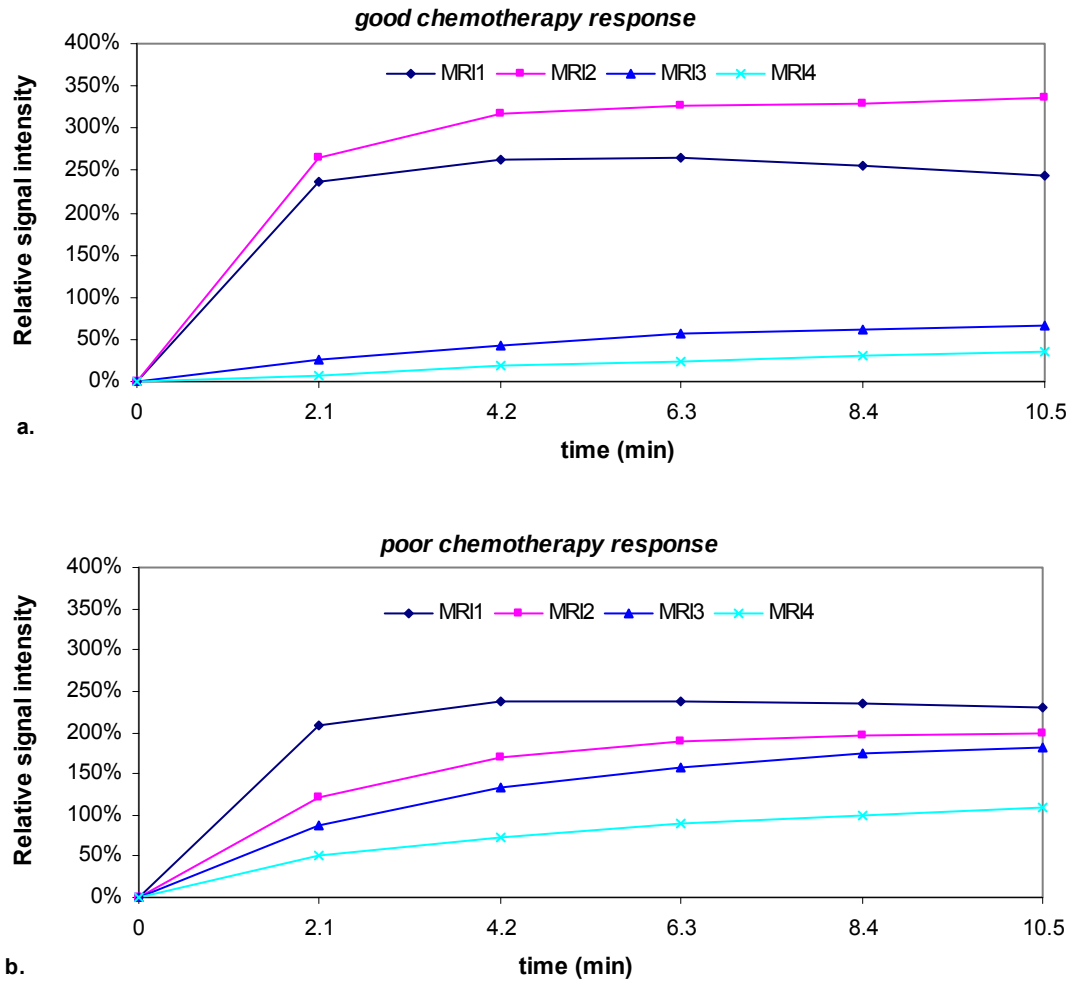

Figure 5.13 Comparison of DCE response of each outcome group
a) shows patients with good chemotherapy (n=3), b) poor chemotherapy response (n=4)

DCE showed decrease relative signal intensity response following chemotherapy (Figure 5.12). The good response group showed greater decrease of relative signal intensity than the poor response group, but no significant difference (Figure 5.13).

ROI analysis showed that the *Kep* value decreased with treatment (Figure 5.14). It indicated that the tumor vascular permeability decreased after therapy, and the good response group was lower than poor response group in MRI 3 and MRI 4.

Based on the different chemotherapy response group, the histogram showed the different behavior with treatment (Figure 5.15). Pre-therapy (MRI 1), the frequency of low-enhancement (<40%) in poor response group was higher than that in good response group, meanwhile, the frequency of high-enhancement (>200%) in poor response group was lower than that in good response group (Figure 5.15a).

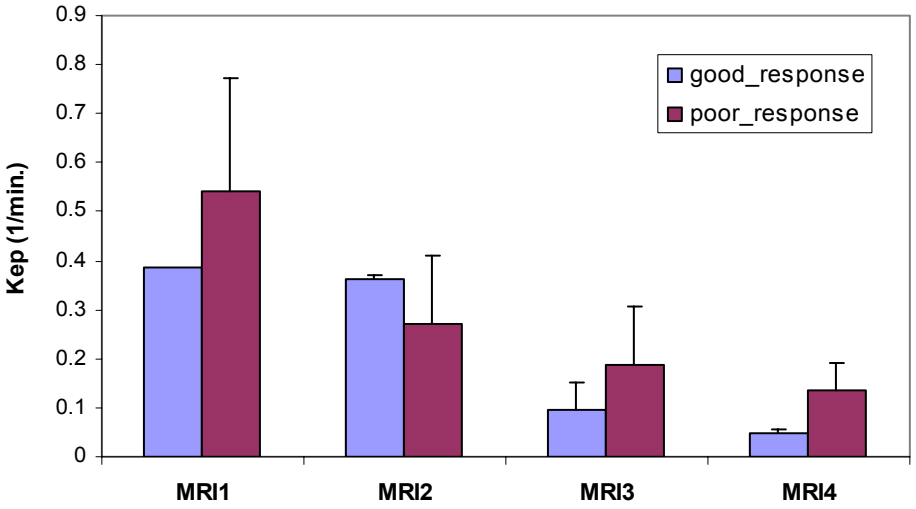

Figure 5.14. the *Kep* value of each chemotherapy response group

After therapy (MRI 4), the situation was reversed. In the good response group low-enhancement (<40%) was over 75 %, while, the frequency of high-enhancement (>200%) in good response group was lower than that in poor response group (Figure 5.15d). The low-enhancement may be caused by poor perfusion and vascular density and the change of vascular function in tumor region. It indicated that relative frequency of low-enhancement and high-enhancement DCE before therapy may be related to the chemotherapy response.

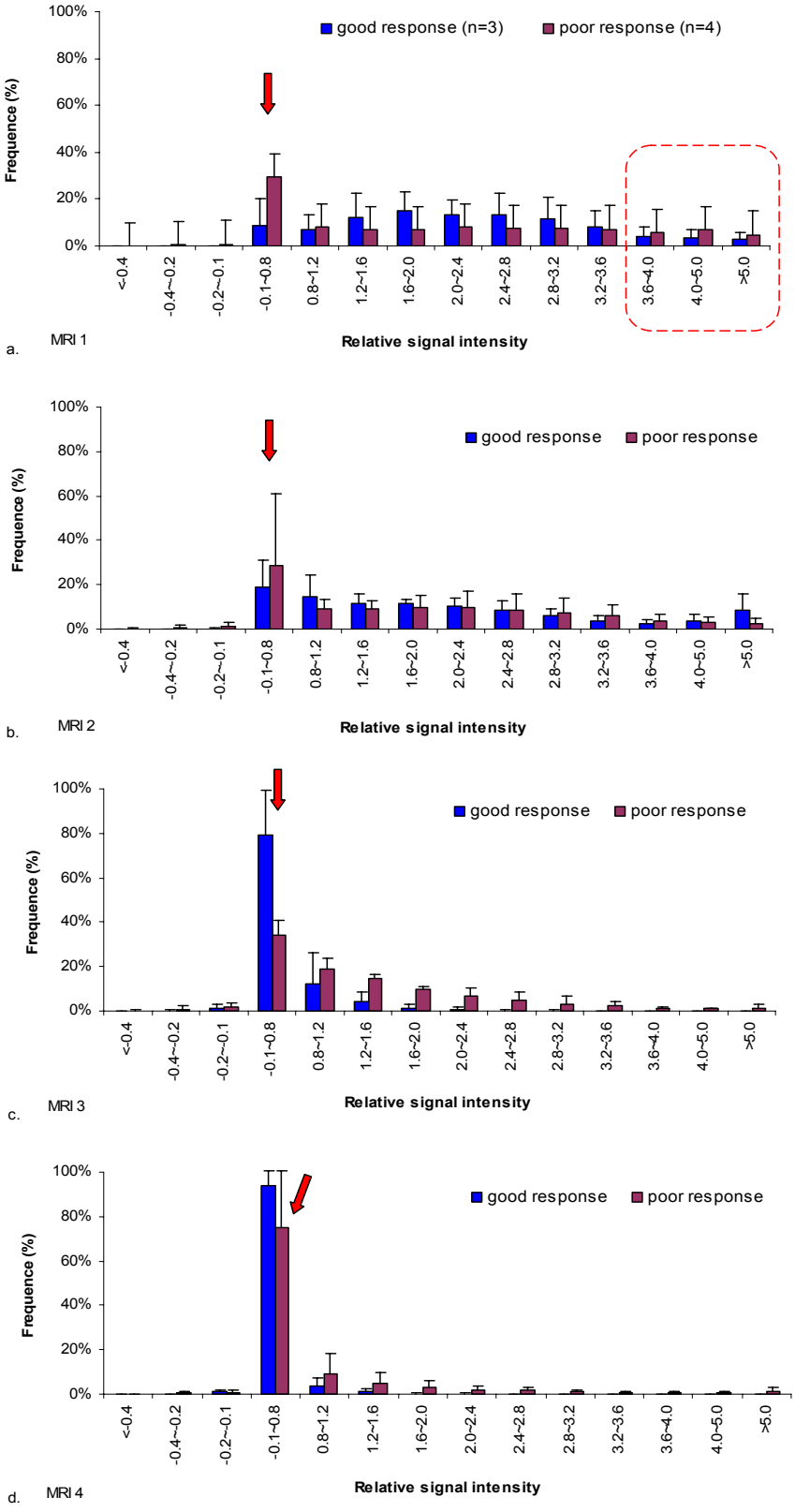

Figure 5.15 Histogram analysis of DCE response to treatment

Comparing the AUC of each response group, the DCE enhancement decreased with treatment. The change in DCE enhancement in good response group was greater than in poor response group at MRI 3 and MRI 4 (Figure 5.16).

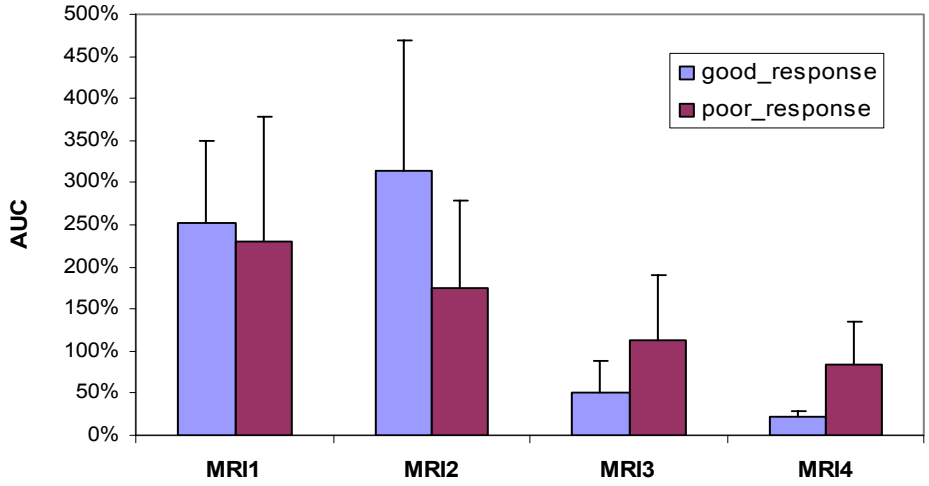

Figure 5.16. Comparison of the AUC of each clinical response group

3. BOLD MRI response to chemotherapy

There was a significant increase in SaO_2 during oxygen inhalation ($p<0.0001$), which recovered to normal after inhalation air (Figure 5.17). The change of oxyhemoglobin is the key for BOLD MRI to generate an intrinsic contrast agent for monitoring patient response. Heart rate showed no significant difference during inhalation oxygen (Figure 5.18).

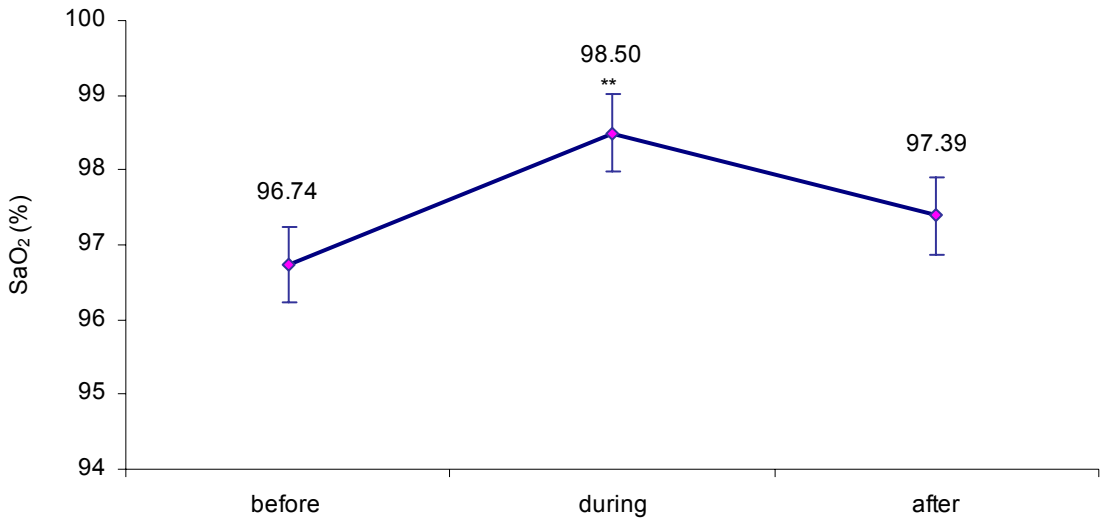

Figure 5.17. Patient oxygen saturation response to oxygen inhalation (n=7)
The (**) showed the significant difference between breathing oxygen ($p<0.0001$). There was no significant difference between before and after breathing oxygen

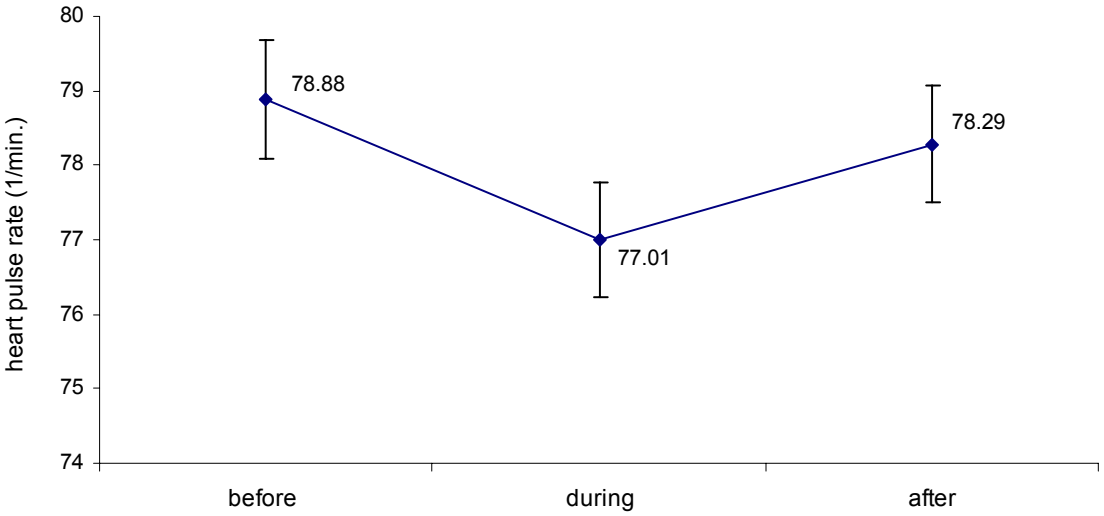

Figure 5.18. Patient heart rate response to inhalation oxygen (n=7)

^{1}H MRI showed there was a region of BOLD contrast enhancement (relative signal intensity gain of 2 to 20%) in all patients, which corresponded to DCE enhancement. Interestingly, a high BOLD response related to good treatment outcome.

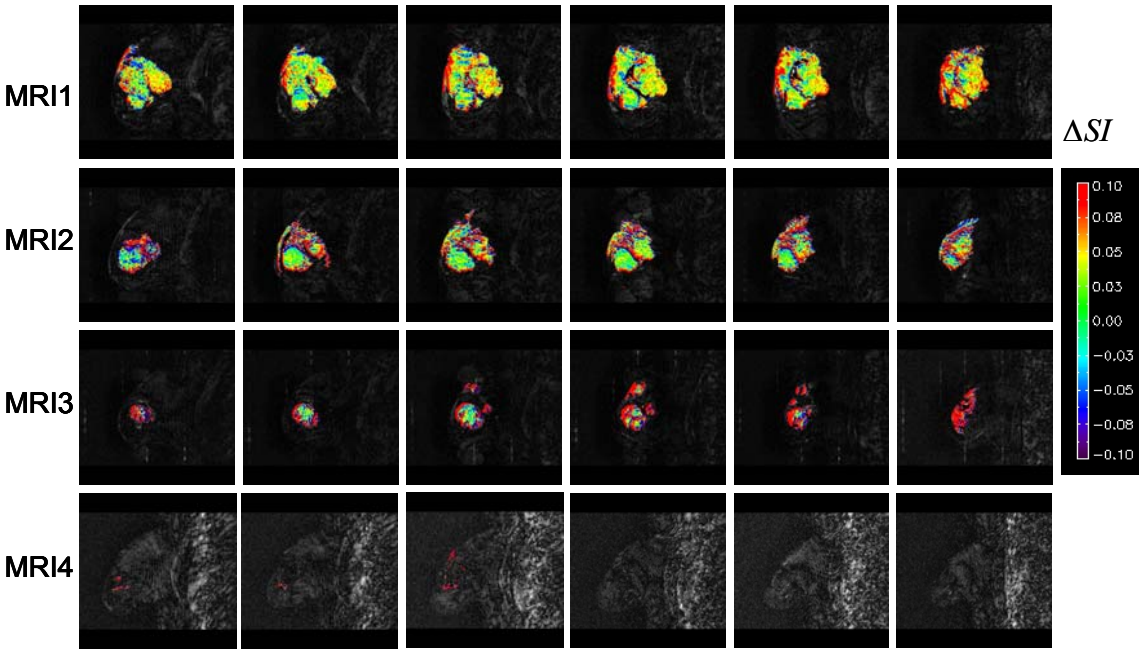

Figure 5.19. BOLD MRI response to chemotherapy in one patient (#7)
it shows six slices and the analyzed tumor regions were overlaid on their raw images

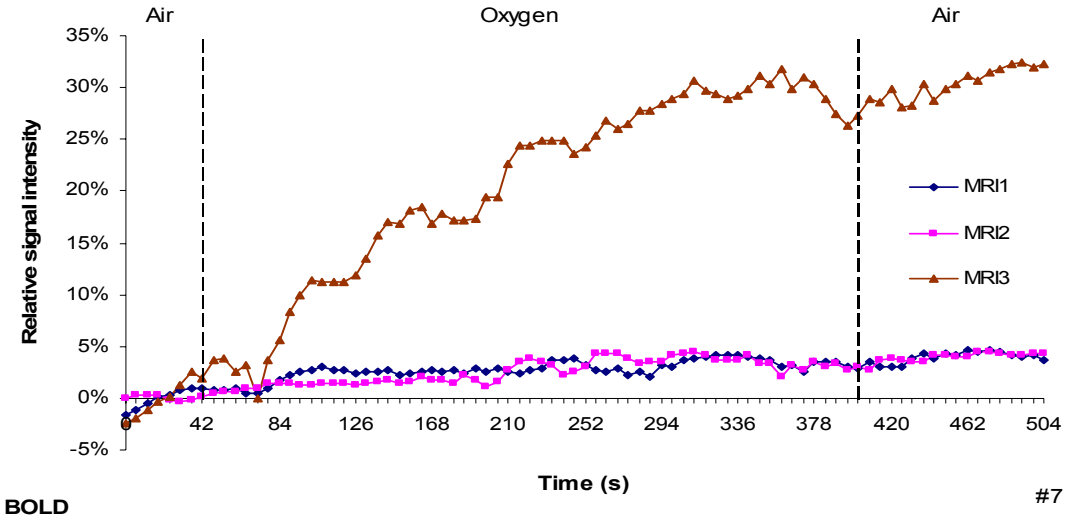

Figure 5.20 BOLD response change in one patient (#7)

One patient showed 3% BOLD response pre-therapy (MRI 1) and during therapy1 (MRI 2), but a 20% BOLD response in MRI 3, and showed significant treatment outcome (Figure 5.19, 5.20).

Comparison of the different chemotherapy response group with BOLD enhancement showed a correlation between a high BOLD response and good treatment outcome. Two patients showed a high BOLD response (>7%) before therapy, and they were all found to have complete or near complete pathological response upon subsequent resection ($p<0.05$) (Table 5.2).

Table 5.2 the relationship between BOLD response and therapeutic efficiency

Patient #	Age (yr)	Tumor Size(cm)	Initial response *ΔSI(%)*				chemotherapy response
			MRI 1	MRI 2	MRI 3	MRI 4	
1	61	11	2	2	2	motion	5.3 cm, PR
2	62	5	12	3	8	motion	Non-palpable, CR
4	51	5	12	5	-		Non-palpable, CR
5	47	8	2	motion	3	motion	6.0 cm, stable
6	44	4.5	3	motion	motion	motion	4.5 cm, stable
7	39	8	3	3	20	9	2.5 cm, PR
8	49	7	3	7	5	12	Non-palpable, CR

stable = less that 30% decrease in tumor size
PR = partial response (greater than 30% decrease in tumor size)
CR= complete response

Figure 5.21 shows the BOLD histogram of each response group before therapy (MRI 1). The results show the frequency of BOLD low-enhancement (<5%) in poor response group was over 50%, which was higher than that in good response group. This result showed the same correlation in DCE enhancement histogram (Figure 5.15a). Comparison of high-enhancement ranges (>5%), there was a significant difference between good and poor response groups ($p<0.05$) (Figure 5.21).

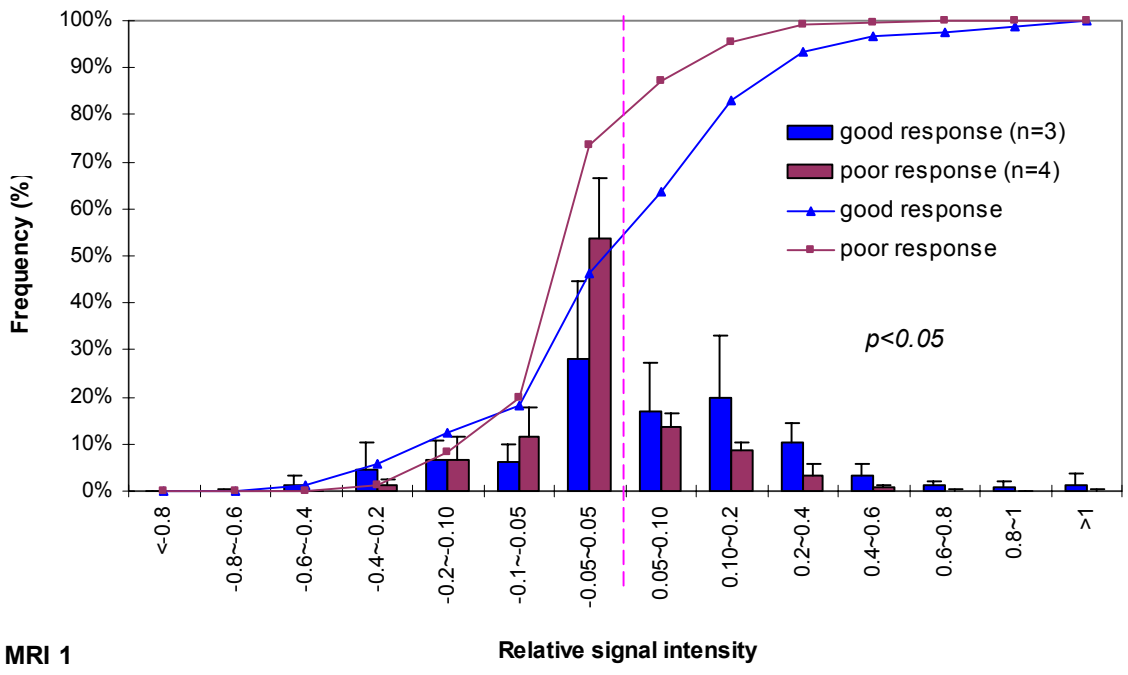

Figure 5.21 Histogram of seven patients' BOLD response before therapy (MRI 1)

4. Prognosis evaluation

How to evaluate the prognostic value of DCE and BOLD MRI is critical. From the histogram analysis, it was clear that both techniques showed some intrinsic prognostic relationship between percentages of non-response and outcome. Which one could be the better prognostic parameter? I consider patients #4 and #5 whose therapeutic response was different from each other. Figure 5.22 shows the DCE enhancement in MRI 1. AUC was quite similar, but histogram showed that the non-enhancing (<80%) in the poor responder was much higher than that in the good responder (Figure 5.22c).

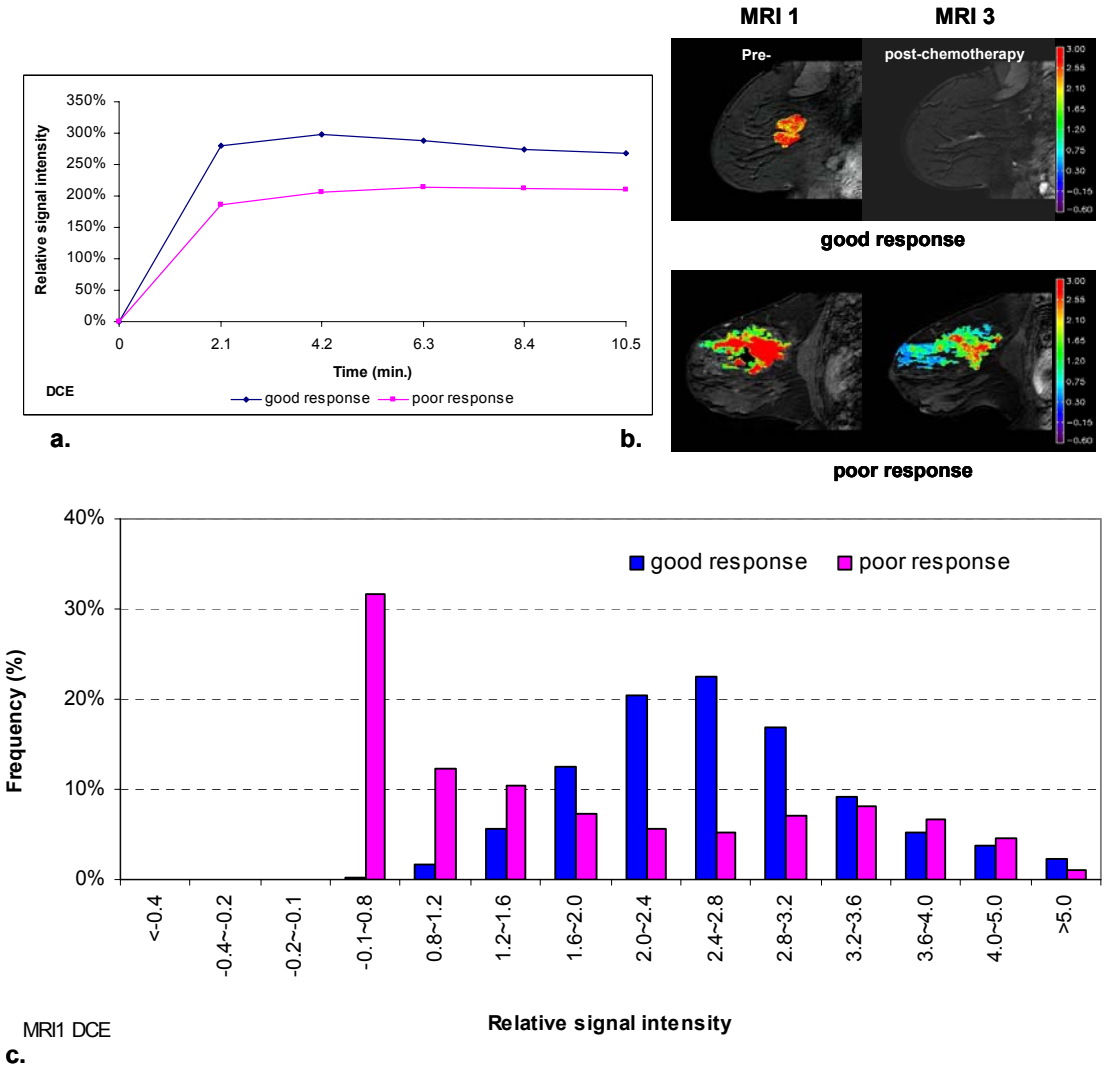

Figure 5. 22. Comparison of two patients DCE enhancement in MRI 1

The same two patients showed BOLD enhancement in MRI 1 (Figure 5.23). The dynamic curve showed a high BOLD enhancement for the good response patient. The AUC showed over 12% in good response patient and 2% in poor response patient (Table 5-2). From the histogram analysis, the non-enhancement (<5%) in poor response patient was also much higher than that in good response patient (Figure 5.23 c).

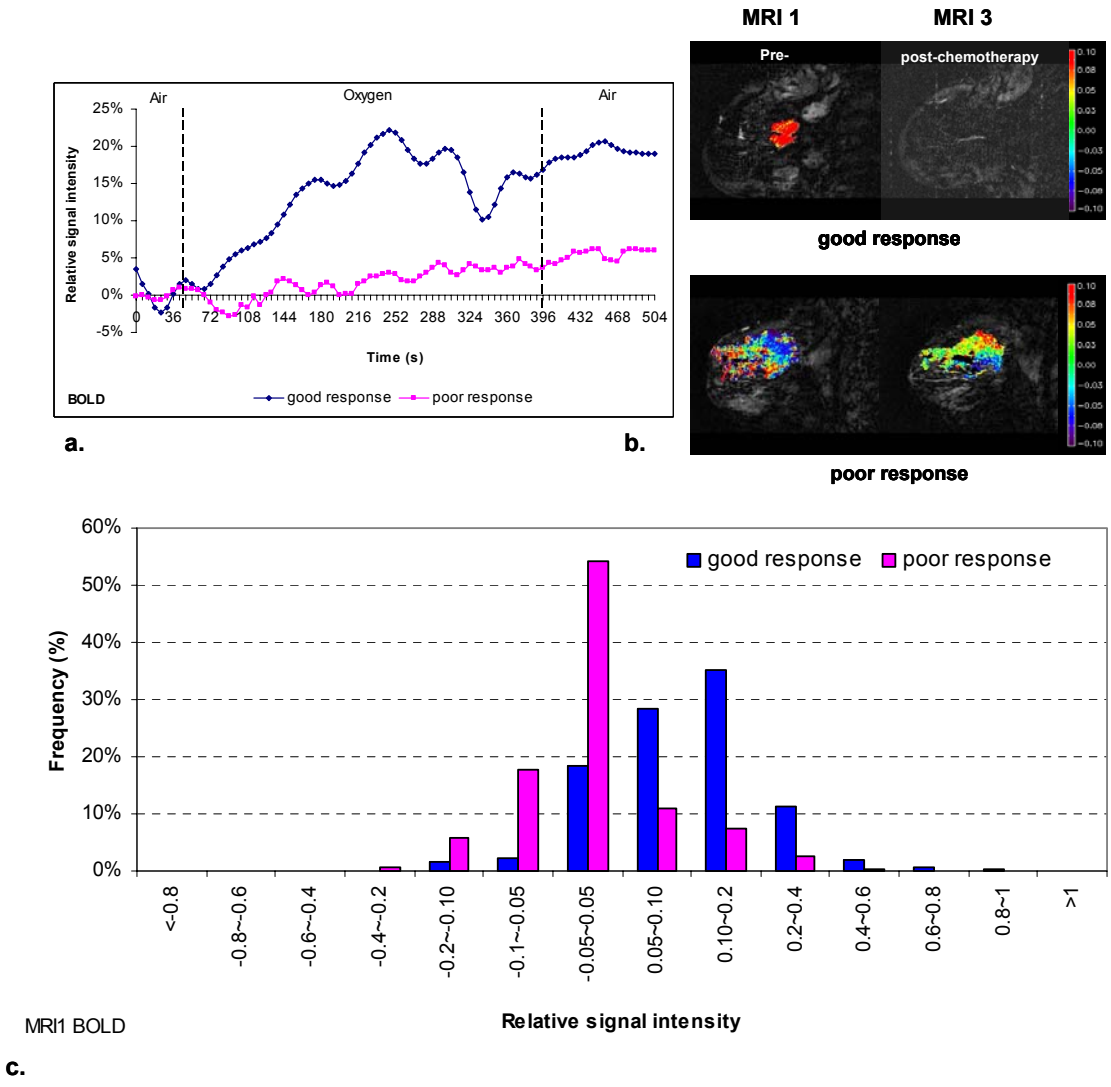

Figure 5.23 comparison of two patient's BOLD enhancement in MRI 1

Following poor response patient#5, it showed there was no big change in DCE and BOLD AUC analysis (Table 5-1, 2). Figure 5.24 shows the comparison of MRI 1 and MRI 3 in histogram analysis. The DCE low-enhancement (<80%) and BOLD low-enhancement (<5%) of MRI 3 were still relative high (Figure 5.24).

The analysis showed some correlation between the frequencies of DCE low-enhancement and BOLD high-enhancement before therapy and treatment outcome.

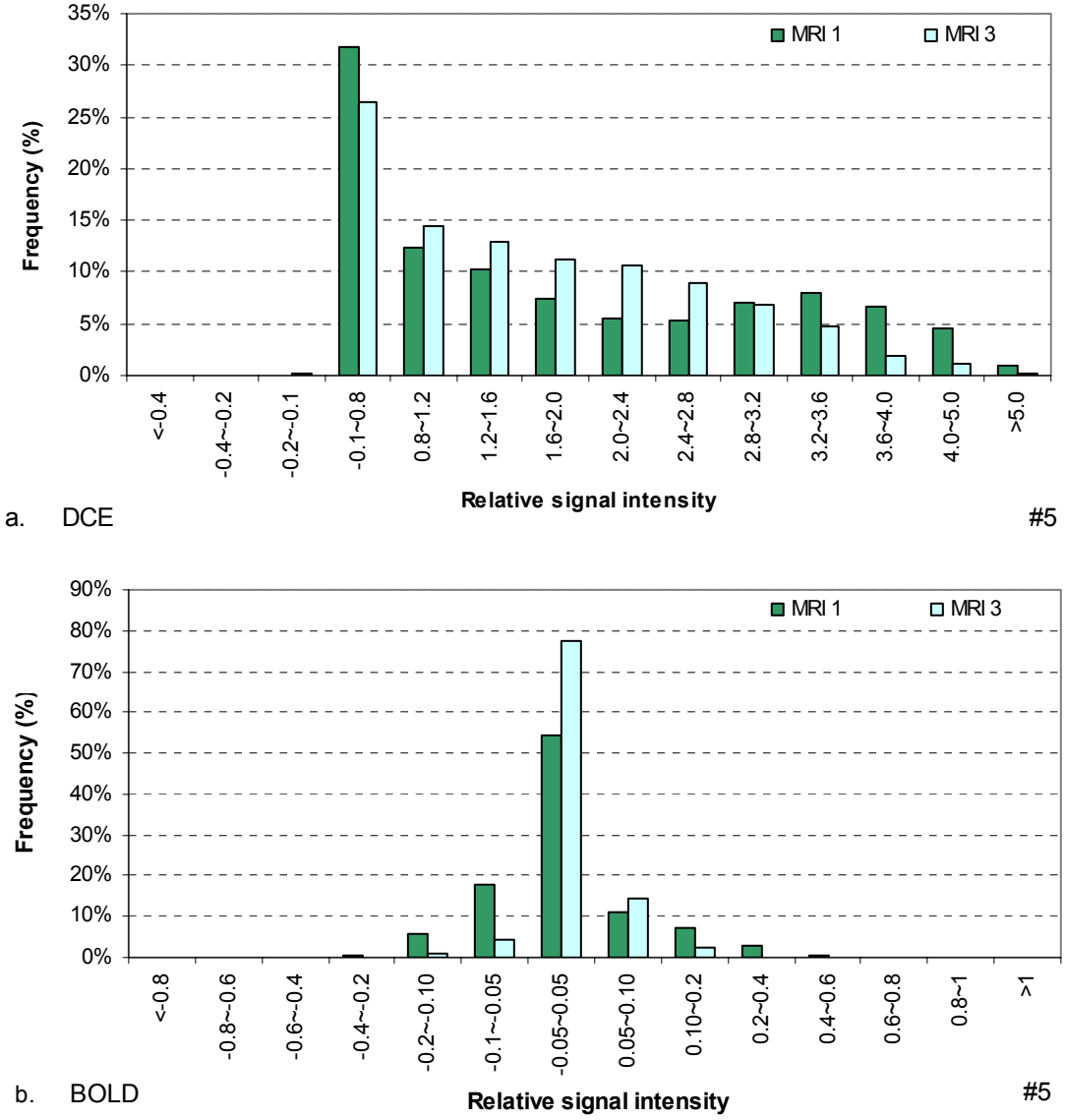

Figure 5.24 comparison of patient #5 DCE and BOLD in MRI 1 and MRI 3

If these two prognostic parameters changed during therapy, what was the patient's treatment outcome? Another example, patient#7 showed low BOLD enhancement 3% in MRI 1 and MRI 2 (Table 5.2), and DCE enhancement decreased from 210% to 164% during MRI 1 and MRI 2 (Table 5.1, Figure 5.25). The frequency of low-enhancement increased with treatment (Figure 5.25a). The DCE enhancement decreased to 96% in MRI 3. The BOLD enhancement showed a big increase (20%) in tumor region in MRI3, and the frequency of low-BOLD-

enhancement was decreased with treatment. Actually, this patient showed significant chemotherapy response after continuing treatment. This case showed that BOLD response can be a prognostic parameter during patient treatment.

Based on the results, the DCE enhancement and BOLD enhancement both showed prognostic value in the breast cancer for assessing chemotherapy. The BOLD enhancement was more sensitive to therapeutic response than AUC and histogram analysis. The disadvantage of BOLD enhancement is the low contrast-to-noise ratio. BOLD imaging requires patient cooperation during scanning. Next, the unsuccessful cases in the clinical study will be discussed.

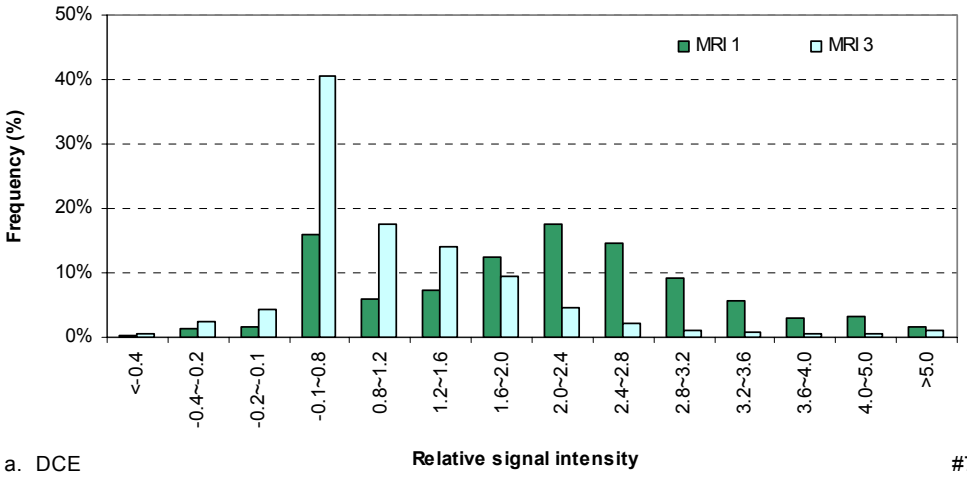

a. DCE #7

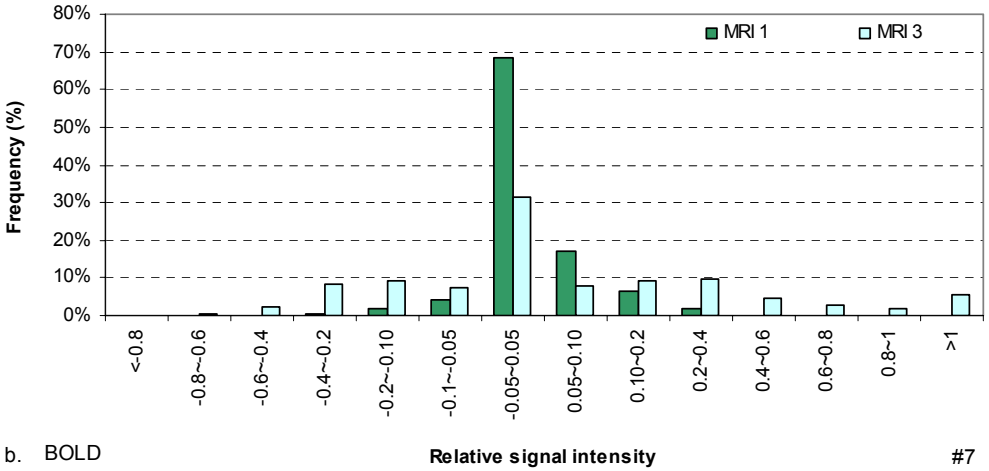

b. BOLD #7

Figure 5.25 comparison of patient #7 response to treatment

5. The unsuccessful imaging cases

There were two factors causing MRI failure during clinical BOLD study. One factor was an artifact during BOLD imaging (Figure 5.26).

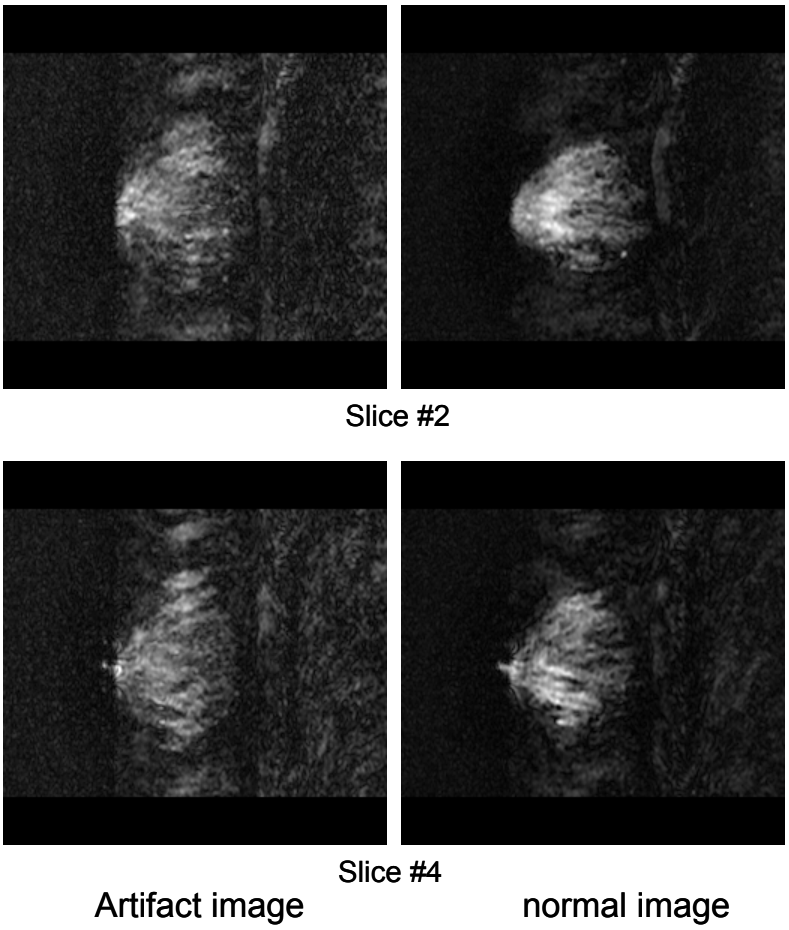

Figure 5.26 Failed BOLD imaging due to artifact

Since the BOLD image required the fast echo-planar imaging during scanning, it suffered from low signal contrast.

Another factor was patient motion during MRI scanning (Figure 5.27). At the beginning of the study, some patients moved, indeed one failed all experiments. By increasing communication with patients before scanning and improving mask handling, recent tests showed no failure due to patient motion in BOLD MRI experiment.

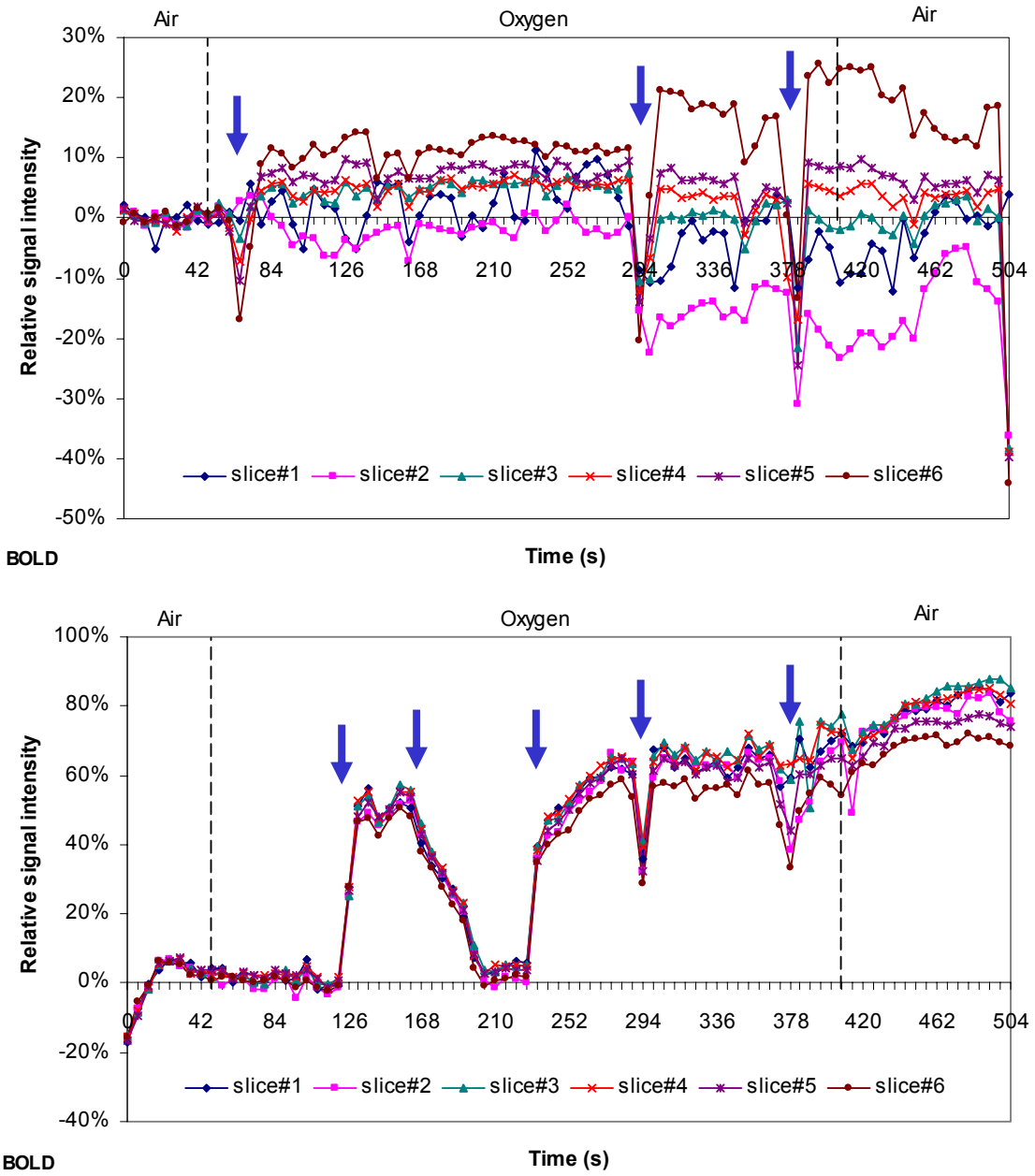

Figure 5.27 Problems of patient motion in BOLD signal (two patients)
(The arrows show patient motion during scanning)

Here, another example showed the patient motion caused the DCE MRI failure (Figure 5.28).

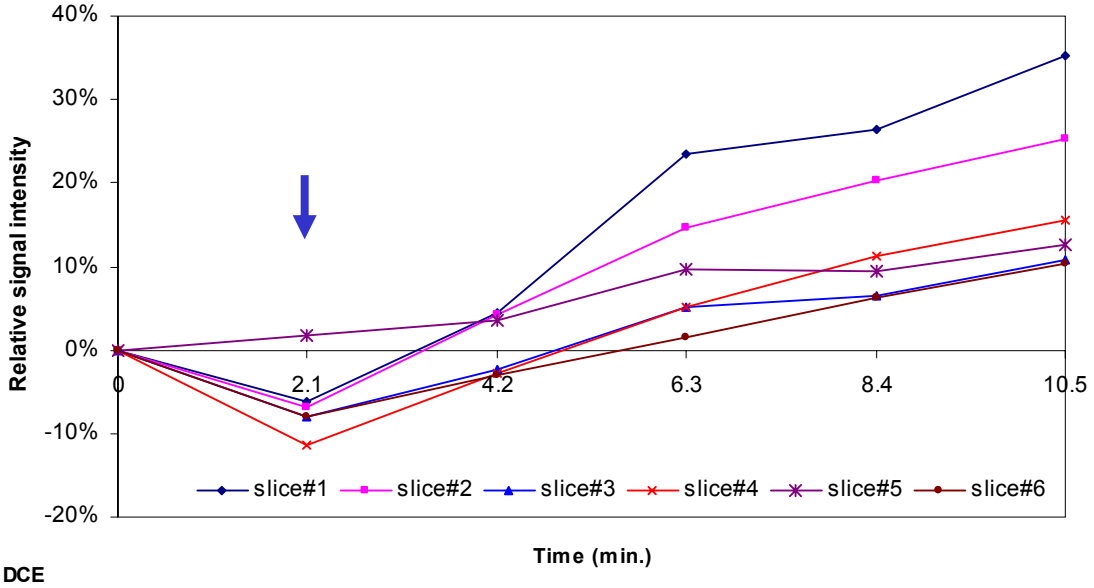

Figure 5.28 Failed DCE data due to patient motion
(The arrow shows patient motion during scanning)

5.4 Discussion

Since fat is the main compartment in normal breast, the chemical shift artifact of fat has to be considered during BOLD and DCE MR imaging. The chemical shift between fat and water is about 3.5 ppm, or a difference of 255 Hz at 1.5T. Because the chemical shift artifact is a spatial mismapping of MRI signal based on frequency, it will cause low signal to noise ratio in water. I believe the use of fat suppression is crucial in clinical breast BOLD and DCE MRI imaging.

In animal experiments the tumor region is obvious. Separating tumor and normal tissue in MR images of the human breast is difficulty, but very important for this study. The intensity of raw images was analyzed on a voxel-by-voxel. The intensity of the tumor region was higher than that in normal tissue during BOLD and DCE

imaging (Figure 5.6, 5.7). Based on each MR image threshold, it was easy to classify the tumor region from BOLD and DCE images.

So far Gd-DTPA contrast MRI has been widely used in the clinical setting for diagnosing tumor vascularity. The high permeability of tumor vessels is a significant characteristic in comparison with the surrounding normal tissue (Figure 5.7). This characteristic of tumor allows use of contrast agent to diagnose tumor. When injecting extrinsic contrast agent, such as Gd-DTPA, the agent could leak out of vessels and into the mass of tumor, causing local T1 change and increasing the signal of T1 weighted images. The contrast medium uptake and signal enhancement are dependent on several physiological factors, such as tumor blood flow, volume of extra-vascular extra-cellular space, vascular surface area, and permeability. DCE MRI has been used to detect the tumor vascular function response during therapy (151). As an extrinsic contrast agent Gd-DTPA gives high contrast to noise ratio. There was big contrast enhancement in the tumor region (average, 200% before chemotherapy). With chemotherapy, the DCE enhancement decreased (Figure 5.11, 5.12). The permeability parameter *Kep* also showed decrease (Figure 5.14). Based on treatment outcome in patients, the AUC and *Kep* in good responders were lower than poor responders at MRI3 and MRI4. There were no significant differences between these two groups (Figure 5.14, 5.16). However, it is hard to predict the final chemotherapeutic outcome only based on the AUC or *Kep* value.

Hypoxia is a characteristic of tumors. Previous studies showed that nearly 50% of locally advanced breast cancers exhibit hypoxic and/or anoxic tissue areas that are heterogeneously distributed within the tumor mass (152). Hypoxia is predominantly

caused by structural and functional abnormalities of the newly formed tumor vessels arising from neovascularization, by a disturbed microcirculation, by enlarged diffusion distances, and by tumor-associated or therapy-induced anemia (152). Also it is main reason for resistance in radiotherapy and chemotherapy. The studies have proved that poor and fluctuating tumor blood flow (acute hypoxia) as well as increased diffusion distances (chronic hypoxia) can result in diminished and erratic distribution of chemotherapeutic agents, with a consequent effect on therapeutic efficacy. Some chemotherapeutic agents, for example, cyclophosphamide, carboplatin and doxorubicin (Adriamycin®), have been shown to be oxygen dependent under both *in vivo* and *in vitro* conditions (153). The microcirculation and oxygenation of tumor can play a very important role in tumor progression with these chemotherapeutic agents. The efficacy of some chemotherapeutic agents can be increased by a variety of direct and indirect mechanisms, which relate to high microcirculation and oxygenation in tumor (142).

Breathing oxygen causes a significant increase in the blood oxygen saturation and a decrease in the amount of deoxyhemoglobin (Figure 5.17). The decrease of deoxyhemoglobin concentration can cause local Bulk Magnetic Susceptibility decrease and increase signal of T2 weighted image. So, the deoxyhemoglobin can be called the intrinsic contrast agent. Also, it has been reported that inhalation of carbogen (95% O_2 + 5% CO_2) gas increases oxygenation of tumor and gives BOLD response in advanced head-and-neck cancers, breast cancers and prostate cancers in the clinical studies (50,74).

The tumor BOLD response to oxygen inhalation was observed in our previous animal study (63,154). Also, the deoxyhemoglobin concentration in tumor region is sensitive to blood volume and hematocrit. Since the local oxygenation level depends upon two factors: oxygen transportation (microcirculation perfusion) and oxygenation consumption, BOLD MRI is sensitive to the change of the microcirculation and oxygenation. My results demonstrate that the signal intensity increased in tumor region during the oxygen inhalation although the range of relative signal intensity was from 2% to 20%. This enhancement suggests that there are BOLD responses in tumor region due to increase oxyhemoglobin or pO_2 in blood in the tumor region by breathing oxygen.

Analysis of BOLD and DCE enhancement histogram showed predictive value for therapeutic response. The DCE enhancement is related to the vascular perfusion, density and function of tumor. The BOLD enhancement is related to the change of the microcirculation and blood oxygenation in the tumor region. The region with high-enhancement in BOLD and DCE could be related to good perfusion and high vascular density in tumor region. My previous chapter, which compared BOLD and DCE MRI with different vascular differentiation in tumor sublines showed the correlation of these two enhancements. If cancer cell metabolism is stable, the perfusion could be the key factor for influencing tumor oxygenation. The change of tumor oxygenation could directly affect the BOLD enhancement. The frequency of low- and high-enhancement of BOLD and DCE becomes an important prognostic parameter for tumor physiology. Comparison of the two patient's response (Figure 5.22,5.23) showed the prognostic value related to the higher frequency of low- and high-

enhancing regions in BOLD and DCE. Following the poor response patient, these parameters didn't change much (Figure 5.24) during treatment. However, if these parameters were changed during the treatment, the patient still can get the good therapeutic response following treatment (Figure 5.25). The histogram analysis proved that the tumor microcirculation (perfusion) could be the key prognostic factor in breast cancer chemotherapy.

The clinical results show correlation between the tumor BOLD responses and therapeutic outcome since chemotherapy agent, doxorubicin (Adriamycin®), reported to be oxygen dependent under both *in vitro* and *in vivo* experiment. The results provided evidence this oxygen dependent relationship exists in clinical patients. Based on our BOLD result it showed that the tumor oxygenation of each patient was different, even the same patient during therapeutic period. For example, one patient showed low BOLD response (3%) during first MRI scanning, and there was high BOLD response (20%) after chemotherapy (Adriamycin®). Following another chemotherapy, this patient showed significant response. Meanwhile her DCE data showed the decreasing AUC. It demonstrated that microcirculation and oxygenation of cancer could be modulated by chemotherapy. With improvement of tumor oxygenation and microcirculation, the efficiency of chemotherapy could be further enhanced in following therapy.

Also, this case may support the idea of "normalization of tumor vasculature" reported by Dr. Jain (155). With treatment, the tumor vasculature was modulated and the microenvironment may was changed. These tumor changes may provide the chance to enhance chemotherapy with improving microcirculation and oxygenation.

The important issue is can we monitor this improvement (normalization window) in the clinic and how to monitor it. My clinical study suggests that BOLD MRI could be useful approach for non-invasively tracking the normalization window in the clinical setting.

In my early BOLD studies, there were some failed cases because of patient motion during MRI scanning. It could be the disadvantage of BOLD examination application clinical practice. Recent study showed the patient motion can be minimized by collaboration of patient and reforming technique of face mask.

Overall, the DCE enhancement and BOLD enhancement both showed the prognostic value in histogram analysis for assessing breast cancer chemotherapy. The BOLD enhancement was more sensitive to therapeutic response in AUC and histogram analysis. Early assessment of therapy effect could be very important during therapy. It was reported that the ^{99m}Tc was used in SPECT for early prediction of the endocrine therapy effect in advanced breast cancer (156).

The BOLD technique is non-invasive and sensitive to the change of the oxygenation and the microcirculation. The correlation between high BOLD response and better treatment outcome suggests a valuable prognostic capability for application in oncology. Furthermore, extensive investigation of BOLD MRI for early assessment of breast cancer chemotherapy is planned.

5.5 Conclusion

The BOLD technique for assessment of breast cancer chemotherapy response may become valuable in the clinical setting. The histogram analysis was used to analyze the BOLD and DCE enhancement of patient. It suggests relationships between the low- and high-enhancement and ultimate chemotherapy response was predictive of ultimate. There is a positive correlation between BOLD enhancement (AUC) and the breast cancer chemotherapy response. During this research, we established techniques for clinical application, which include the special MRI pulse sequence, the identification of cancer region, the data processing strategy, and the parameter for BOLD and DCE analysis, and patient handling during MRI scanning. The significant correlation between high BOLD response and good treatment outcome will give a valuable prognostic capability for application in oncology. If this technique could be early applying in the clinical setting and benefit to huge patient population, it could be our greatest pleasure in this research.

CHAPTER 6

Conclusions and Recommendations

Oxygenation and microcirculation play very critical roles in tumor growth and therapy. Using a non-invasive approach to evaluate tumor oxygenation and microcirculation could assist in assessing tumor therapeutic response and planning further treatment or developing novel therapeutic stratagem.

As reported, the "steal effect" in BOLD study is common during voxel-by-voxel analysis, which shows the negative relative signal during BOLD response. In my work, I found the BOLD signal decreased during blood oxygenation increase in phantom study. The vessels which were different angle with Bo showed the different "in-flow effect" and the enhancement of BOLD signal in oxygenation variation was greater than that in flow variation. This may help us to understand tumor physiological response during the inhalation oxygen.

The MRI DCE and BOLD results were compared in animal tumor experiment. It demonstrated a correlation between DCE and BOLD in regional response of the prostate tumor via different microvascular development.

Finally, the DCE and BOLD MRI techniques were used in breast cancer for evaluation of chemotherapy in the clinical setting. The DCE and BOLD imaging techniques and data processing approach were established. BOLD signal is sensitive to changes of tumor oxygenation and the blood flow, which is very useful information for tumor prognosis in clinic setting. However, patient motion during scanning could fail the BOLD data because of low contrast-to-noise ratio. How to

minimize patient motion during MRI scanning becomes very important for clinical application. The clinical results have demonstrated that the BOLD technique potential value in the tumor oncology.

There are some recommendations for further BOLD clinical research, for example, using negative pressure breast coil for controlling breast position, using the diving mask to minimize patient motion during changing gas, using air-oxygen-air-oxygen-air breathing pattern for investigating breast cancer response, using single shot EPI for increasing signal quality.

- Research supported

DOD graduate fellowship DAMD17-02-1-0592(LJ), Susan G. Komen Foundation IMG-0402967, NIH R01 79515, and using facilities of the Rogers MR center, an NIH BTRP Facility #P41-RR02584, and the Cancer Imaging Program (Pre-ICMIC) P20 CA86354.

REFERENCES:

1. Goffman TE, Raubitschek A, Mitchell JB, Glatstein E. The emerging biology of modern radiation oncology. Cancer Res 1990;50(24):7735-7744.

2. Jain RK. Determinants of tumor blood flow: a review. Cancer Res 1988;48(10):2641-2658.

3. Shubik P. Vascularization of tumors: a review. J Cancer Res Clin Oncol 1982;103(3):211-226.

4. Jain RK. Barriers to drug delivery in solid tumors. Sci Am 1994;271(1):58-65.

5. Song CW. Effect of local hyperthermia on blood flow and microenvironment: a review. Cancer Res 1984;44(10 Suppl):4721s-4730s.

6. Chaplin DJ, Olive PL, Durand RE. Intermittent blood flow in a murine tumor: radiobiological effects. Cancer Res 1987;47(2):597-601.

7. Vaupel P, Kallinowski F, Okunieff P. Blood flow, oxygen and nutrient supply, and metabolic microenvironment of human tumors: a review. Cancer Res 1989;49(23):6449-6465.

8. Vaupel P, Fortmeyer HP, Runkel S, Kallinowski F. Blood flow, oxygen consumption, and tissue oxygenation of human breast cancer xenografts in nude rats. Cancer Res 1987;47(13):3496-3503.

9. Kallinowski F, Zander R, Hoeckel M, Vaupel P. Tumor tissue oxygenation as evaluated by computerized-pO_2-histography. Int J Radiat Oncol Biol Phys 1990;19(4):953-961.

10. Griebel J, Mayr NA, de Vries A, Knopp MV, Gneiting T, Kremser C, Essig M, Hawighorst H, Lukas PH, Yuh WT. Assessment of tumor microcirculation: a new role of dynamic contrast MR imaging. J Magn Reson Imaging 1997;7(1):111-119.

11. Reddick WE, Taylor JS, Fletcher BD. Dynamic MR imaging (DEMRI) of microcirculation in bone sarcoma. J Magn Reson Imaging 1999;10(3):277-285.

12. Mayr NA, Hawighorst H, Yuh WT, Essig M, Magnotta VA, Knopp MV. MR microcirculation assessment in cervical cancer: correlations with histomorphological tumor markers and clinical outcome. J Magn Reson Imaging 1999;10(3):267-276.

13. Taylor JS, Tofts PS, Port R, Evelhoch JL, Knopp M, Reddick WE, Runge VM, Mayr N. MR imaging of tumor microcirculation: promise for the new millennium. J Magn Reson Imaging 1999;10(6):903-907.

14. Nagele T, Petersen D, Klose U, Grodd W, Opitz H, Gut E, Martos J, Voigt K. Dynamic contrast enhancement of intracranial tumors with snapshot-FLASH MR imaging. AJNR Am J Neuroradiol 1993;14(1):89-98.

15. Fujii K, Fujita N, Hirabuki N, Hashimoto T, Miura T, Kozuka T. Neuromas and meningiomas: evaluation of early enhancement with dynamic MR imaging. AJNR Am J Neuroradiol 1992;13(4):1215-1220.

16. Brooks RA, Brunetti A, Alger JR, Di Chiro G. On the origin of paramagnetic inhomogeneity effects in blood. Magn Reson Med 1989;12(2):241-248.

17. Robinson SP, Howe FA, Griffiths JR. Noninvasive monitoring of carbogen-induced changes in tumor blood flow and oxygenation by functional magnetic resonance imaging. Int J Radiat Oncol Biol Phys 1995;33(4):855-859.

18. Peller M, Weissfloch L, Stehling MK, Weber J, Bruening R, Senekowitsch-Schmidtke R, Molls M, Reiser M. Oxygen-induced MR signal changes in murine tumors. Magn Reson Imaging 1998;16(7):799-809.

19. Al-Hallaq HA, Zamora M, Fish BL, Farrell A, Moulder JE, Karczmar GS. MRI measurements correctly predict the relative effects of tumor oxygenating agents on hypoxic fraction in rodent BA1112 tumors. Int J Radiat Oncol Biol Phys 2000;47(2):481-488.

20. Ogawa S, Menon RS, Tank DW, Kim SG, Merkle H, Ellermann JM, Ugurbil K. Functional brain mapping by blood oxygenation level-dependent contrast magnetic resonance imaging. A comparison of signal characteristics with a biophysical model. Biophys J 1993;64(3):803-812.

21. Ogawa S, Lee TM, Kay AR, Tank DW. Brain magnetic resonance imaging with contrast dependent on blood oxygenation. Proc Natl Acad Sci U S A 1990;87(24):9868-9872.

22. Ogawa S, Menon RS, Kim SG, Ugurbil K. On the characteristics of functional magnetic resonance imaging of the brain. Annu Rev Biophys Biomol Struct 1998;27:447-474.

23. Krings T, Erberich SG, Roessler F, Reul J, Thron A. MR blood oxygenation level-dependent signal differences in parenchymal and large draining vessels: implications for functional MR imaging. AJNR Am J Neuroradiol 1999;20(10):1907-1914.

24. Thulborn KR, Waterton JC, Matthews PM, Radda GK. Oxygenation dependence of the transverse relaxation time of water protons in whole blood at high field. Biochim Biophys Acta 1982;714(2):265-270.

25. Robinson SP, Rijken PF, Howe FA, McSheehy PM, van der Sanden BP, Heerschap A, Stubbs M, van der Kogel AJ, Griffiths JR. Tumor vascular architecture and function evaluated by non-invasive susceptibility MRI methods and immunohistochemistry. J Magn Reson Imaging 2003;17(4):445-454.

26. Mazurchuk R, Zhou R, Straubinger RM, Chau RI, Grossman Z. Functional magnetic resonance (fMR) imaging of a rat brain tumor model: implications for evaluation of tumor microvasculature and therapeutic response. Magn Reson Imaging 1999;17(4):537-548.

27. Taylor NJ, Baddeley H, Goodchild KA, Powell ME, Thoumine M, Culver LA, Stirling JJ, Saunders MI, Hoskin PJ, Phillips H, Padhani AR, Griffiths JR. BOLD MRI of human tumor oxygenation during carbogen breathing. J Magn Reson Imaging 2001;14(2):156-163.

28. Landuyt W, Hermans R, Bosmans H, Sunaert S, Beatse E, Farina D, Meijerink M, Zhang H, Van Den Bogaert W, Lambin P, Marchal G. BOLD contrast fMRI of whole rodent tumour during air or carbogen breathing using echo-planar imaging at 1.5 T. Eur Radiol 2001;11(11):2332-2340.

29. Elas M, Williams BB, Parasca A, Mailer C, Pelizzari CA, Lewis MA, River JN, Karczmar GS, Barth ED, Halpern HJ. Quantitative tumor oxymetric images from 4D electron paramagnetic resonance imaging (EPRI): methodology and comparison with blood oxygen level-dependent (BOLD) MRI. Magn Reson Med 2003;49(4):682-691.

30. Fan X, River JN, Zamora M, Al-Hallaq HA, Karczmar GS. Effect of carbogen on tumor oxygenation: combined fluorine-19 and proton MRI measurements. Int J Radiat Oncol Biol Phys 2002;54(4):1202-1209.

31. Baudelet C, Gallez B. How does blood oxygen level-dependent (BOLD) contrast correlate with oxygen partial pressure (pO_2) inside tumors? Magn Reson Med 2002;48(6):980-986.

32. Baudelet C, Gallez B. Cluster analysis of BOLD fMRI time series in tumors to study the heterogeneity of hemodynamic response to treatment. Magn Reson Med 2003;49(6):985-990.

33. Griffiths JR, Taylor NJ, Howe FA, Saunders MI, Robinson SP, Hoskin PJ, Powell ME, Thoumine M, Caine LA, Baddeley H. The response of human tumors to carbogen breathing, monitored by Gradient-Recalled Echo Magnetic Resonance Imaging. Int J Radiat Oncol Biol Phys 1997;39(3):697-701.

34. Noseworthy MD, Kim JK, Stainsby JA, Stanisz GJ, Wright GA. Tracking oxygen effects on MR signal in blood and skeletal muscle during hyperoxia exposure. J Magn Reson Imaging 1999;9(6):814-820.

35. Robinson SP, Howe FA, Rodrigues LM, Stubbs M, Griffiths JR. Magnetic resonance imaging techniques for monitoring changes in tumor oxygenation and blood flow. Semin Radiat Oncol 1998;8(3):197-207.

36. Robinson SP, Collingridge DR, Howe FA, Rodrigues LM, Chaplin DJ, Griffiths JR. Tumour response to hypercapnia and hyperoxia monitored by FLOOD magnetic resonance imaging. NMR Biomed 1999;12(2):98-106.

37. Robinson SP, Rodrigues LM, Howe FA, Stubbs M, Griffiths JR. Effects of different levels of hypercapnic hyperoxia on tumour R(2)* and arterial blood gases. Magn Reson Imaging 2001;19(2):161-166.

38. Li KC, Wright GA, Pelc LR, Dalman RL, Brittain JH, Wegmueller H, Lin DT, Song CK. Oxygen saturation of blood in the superior mesenteric vein: in vivo verification of MR imaging measurements in a canine model. Work in progress. Radiology 1995;194(2):321-325.

39. van Zijl PC, Eleff SM, Ulatowski JA, Oja JM, Ulug AM, Traystman RJ, Kauppinen RA. Quantitative assessment of blood flow, blood volume and blood oxygenation effects in functional magnetic resonance imaging. Nat Med 1998;4(2):159-167.

40. Moonen CT, van Zijl PC, Frank JA, Le Bihan D, Becker ED. Functional magnetic resonance imaging in medicine and physiology. Science 1990;250(4977):53-61.

41. Knopp MV, Weiss E, Sinn HP, Mattern J, Junkermann H, Radeleff J, Magener A, Brix G, Delorme S, Zuna I, van Kaick G. Pathophysiologic basis of contrast enhancement in breast tumors. J Magn Reson Imaging 1999;10(3):260-266.

42. Holodny AI, Schulder M, Liu WC, Wolko J, Maldjian JA, Kalnin AJ. The effect of brain tumors on BOLD functional MR imaging activation in the adjacent motor cortex: implications for image-guided neurosurgery. AJNR Am J Neuroradiol 2000;21(8):1415-1422.

43. Holodny AI, Schulder M, Liu WC, Maldjian JA, Kalnin AJ. Decreased BOLD functional MR activation of the motor and sensory cortices adjacent to a glioblastoma multiforme: implications for image-guided neurosurgery. AJNR Am J Neuroradiol 1999;20(4):609-612.

44. Helmer KG, Han S, Sotak CH. On the correlation between the water diffusion coefficient and oxygen tension in RIF-1 tumors. NMR Biomed 1998;11(3):120-130.

45. Hathout GM, Gambhir SS, Gopi RK, Kirlew KA, Choi Y, So G, Gozal D, Harper R, Lufkin RB, Hawkins R. A quantitative physiologic model of blood oxygenation for functional magnetic resonance imaging. Invest Radiol 1995;30(11):669-682.

46. Hoge RD, Atkinson J, Gill B, Crelier GR, Marrett S, Pike GB. Investigation of BOLD signal dependence on cerebral blood flow and oxygen consumption: the deoxyhemoglobin dilution model. Magn Reson Med 1999;42(5):849-863.

47. Smith RF, Rutt BK, Holdsworth DW. Anthropomorphic carotid bifurcation phantom for MRI applications. J Magn Reson Imaging 1999;10(4):533-544.

48. Johansson LO, Fischer SE, Lorenz CH. Benefit of T1 reduction for magnetic resonance coronary angiography: a numerical simulation and phantom study. J Magn Reson Imaging 1999;9(4):552-556.

49. Robinson SP, Rodrigues LM, Ojugo AS, McSheehy PM, Howe FA, Griffiths JR. The response to carbogen breathing in experimental tumour models monitored by gradient-recalled echo magnetic resonance imaging. Br J Cancer 1997;75(7):1000-1006.

50. Howe FA, Robinson SP, Rodrigues LM, Griffiths JR. Flow and oxygenation dependent (FLOOD) contrast MR imaging to monitor the response of rat tumors to carbogen breathing. Magn Reson Imaging 1999;17(9):1307-1318.

51. McDonald DA. Blood flow in arteries. 1960(Baltimore : Williams & Wilkins, 1960.):15-27.

52. Bradley WG, Jr., Waluch V, Lai KS, Fernandez EJ, Spalter C. The appearance of rapidly flowing blood on magnetic resonance images. AJR Am J Roentgenol 1984;143(6):1167-1174.

53. Caro C.G. PTJ, and Seed W.A. Mechanics of the circulation. Guyton AC, editor. London: Medical and Technical Publishers; 1974.

54. Wang Z, Su MY, Nalcioglu O. Measurement of tumor vascular volume and mean microvascular random flow velocity magnitude by dynamic Gd-DTPA-albumin enhanced and diffusion-weighted MRI. Magn Reson Med 1998;40(3):397-404.

55. S. Manimala Rao VN. Arterial blood gas monitoring. Indian J Anaesth 2002;46(4):289-297.

56. Dewhirst MW, Ong ET, Klitzman B, Secomb TW, Vinuya RZ, Dodge R, Brizel D, Gross JF. Perivascular oxygen tensions in a transplantable mammary tumor growing in a dorsal flap window chamber. Radiat Res 1992;130(2):171-182.

57. Silvennoinen MJ, Clingman CS, Golay X, Kauppinen RA, van Zijl PC. Comparison of the dependence of blood R2 and R2* on oxygen saturation at 1.5 and 4.7 Tesla. Magn Reson Med 2003;49(1):47-60.

58. Gati JS, Menon RS, Ugurbil K, Rutt BK. Experimental determination of the BOLD field strength dependence in vessels and tissue. Magn Reson Med 1997;38(2):296-302.

59. Spees WM, Yablonskiy DA, Oswood MC, Ackerman JJ. Water proton MR properties of human blood at 1.5 Tesla: magnetic susceptibility, T(1), T(2), T*(2), and non-Lorentzian signal behavior. Magn Reson Med 2001;45(4):533-542.

60. Janne d'Othee B, Rachmuth G, Munasinghe J, Lang EV. The effect of hyperoxygenation on T1 relaxation time in vitro. Acad Radiol 2003;10(8):854-860.

61. Bradley WG, Jr., Waluch V. Blood flow: magnetic resonance imaging. Radiology 1985;154(2):443-450.

62. Urchuk SN, Plewes DB. Mechanisms of flow-induced signal loss in MR angiography. J Magn Reson Imaging 1992;2(4):453-462.

63. Jiang L, Zhao D, Constantinescu A, Mason RP. Comparison of BOLD contrast and Gd-DTPA dynamic contrast-enhanced imaging in rat prostate tumor. Magn Reson Med 2004;51(5):953-960.

64. Reichenbach JR, Venkatesan R, Schillinger DJ, Kido DK, Haacke EM. Small vessels in the human brain: MR venography with deoxyhemoglobin as an intrinsic contrast agent. Radiology 1997;204(1):272-277.

65. Reichenbach JR, Venkatesan R, Yablonskiy DA, Thompson MR, Lai S, Haacke EM. Theory and application of static field inhomogeneity effects in gradient-echo imaging. J Magn Reson Imaging 1997;7(2):266-279.

66. Rauscher A, Sedlacik J, Barth M, Haacke EM, Reichenbach JR. Nonnvasive assessment of vascular architecture and function during modulated blood oxygenation using susceptibility weighted magnetic resonance imaging. Magn Reson Med 2005;54(1):87-95.

67. Hawighorst H, Knapstein PG, Knopp MV, Weikel W, Brix G, Zuna I, Schonberg SO, Essig M, Vaupel P, van Kaick G. Uterine cervical carcinoma: comparison of standard and pharmacokinetic analysis of time-intensity curves for assessment of tumor angiogenesis and patient survival. Cancer Res 1998;58(16):3598-3602.

68. Turetschek K, Preda A, Novikov V, Brasch RC, Weinmann HJ, Wunderbaldinger P, Roberts TP. Tumor microvascular changes in antiangiogenic treatment: assessment by magnetic resonance contrast media of different molecular weights. J Magn Reson Imaging 2004;20(1):138-144.

69. Cao Y, Brown SL, Knight RA, Fenstermacher JD, Ewing JR. Effect of intravascular-to-extravascular water exchange on the determination of blood-to-tissue transfer constant by magnetic resonance imaging. Magn Reson Med 2005;53(2):282-293.

70. Collins DJ, Padhani AR. Dynamic magnetic resonance imaging of tumor perfusion. Approaches and biomedical challenges. IEEE Eng Med Biol Mag 2004;23(5):65-83.

71. Su MY, Jao JC, Nalcioglu O. Measurement of vascular volume fraction and blood-tissue permeability constants with a pharmacokinetic model: studies in rat muscle tumors with dynamic Gd-DTPA enhanced MRI. Magn Reson Med 1994;32(6):714-724.

72. Tofts PS, Brix G, Buckley DL, Evelhoch JL, Henderson E, Knopp MV, Larsson HB, Lee TY, Mayr NA, Parker GJ, Port RE, Taylor J, Weisskoff RM. Estimating kinetic parameters from dynamic contrast-enhanced T(1)-weighted MRI of a diffusable tracer: standardized quantities and symbols. J Magn Reson Imaging 1999;10(3):223-232.

73. Abramovitch R, Frenkiel D, Neeman M. Analysis of subcutaneous angiogenesis by gradient echo magnetic resonance imaging. Magn Reson Med 1998;39(5):813-824.

74. van der Sanden BP, Heerschap A, Hoofd L, Simonetti AW, Nicolay K, van der Toorn A, Colier WN, van der Kogel AJ. Effect of carbogen breathing on the physiological profile of human glioma xenografts. Magn Reson Med 1999;42(3):490-499.

75. Rijpkema M, Kaanders JH, Joosten FB, van der Kogel AJ, Heerschap A. Effects of breathing a hyperoxic hypercapnic gas mixture on blood oxygenation and vascularity of head-and-neck tumors as measured by magnetic resonance imaging. Int J Radiat Oncol Biol Phys 2002;53(5):1185-1191.

76. Lohr F, Wenz F, Flentje M, Peschke P, Hahn EW. Measurement of the proliferative activity of three different sublines of the Dunning rat prostate tumor R3327. Strahlenther Onkol 1993;169(7):438-445.

77. Tennant TR, Kim H, Sokoloff M, Rinker-Schaeffer CW. The Dunning model. Prostate 2000;43(4):295-302.

78. Zhao D, Ran S, Constantinescu A, Hahn EW, Mason RP. Tumor oxygen dynamics: correlation of in vivo MRI with histological findings. Neoplasia 2003;5(4):308-318.

79. Hahn EW, Peschke P, Mason RP, Babcock EE, Antich PP. Isolated tumor growth in a surgically formed skin pedicle in the rat: a new tumor model for NMR studies. Magn Reson Imaging 1993;11(7):1007-1017.

80. Zhao D, Jiang L, Mason RP. Measuring changes in tumor oxygenation. Methods Enzymol 2004;386:378-418.

81. Port RE, Knopp MV, Hoffmann U, Milker-Zabel S, Brix G. Multicompartment analysis of gadolinium chelate kinetics: blood-tissue exchange in mammary tumors as monitored by dynamic MR imaging. J Magn Reson Imaging 1999;10(3):233-241.

82. Delorme S, Peschke P, Zuna I, Van Kaick G. Sensitivity of color Doppler sonography: an experimental approach. Ultrasound Med Biol 1999;25(4):541-547.

83. Karam JA, Mason RP, Koeneman KS, Antich PP, Benaim EA, Hsieh JT. Molecular imaging in prostate cancer. J Cell Biochem 2003;90(3):473-483.

84. Mason RP, Antich PP, Babcock EE, Constantinescu A, Peschke P, Hahn EW. Non-invasive determination of tumor oxygen tension and local variation with growth. Int J Radiat Oncol Biol Phys 1994;29(1):95-103.

85. Zhao D, Jiang L, Hahn EW, Mason RP. Continuous low-dose (metronomic) chemotherapy on rat prostate tumors evaluated using MRI in vivo and comparison with histology. Neoplasia 2005;7(7):678-687.

86. Choyke PL, Dwyer AJ, Knopp MV. Functional tumor imaging with dynamic contrast-enhanced magnetic resonance imaging. J Magn Reson Imaging 2003;17(5):509-520.

87. Hayes C, Padhani AR, Leach MO. Assessing changes in tumour vascular function using dynamic contrast-enhanced magnetic resonance imaging. NMR Biomed 2002;15(2):154-163.

88. Jiang L MR, Weatherall P, Debu Tripathy, Mason PR. Using BOLD and Gd-DTPA Contrast Enhanced MRI for Early Evaluation of Breast Cancer Chemotherapy. 2005 2005; Philadelphia PA,. p 63-64.

89. Thomas CD, Chenu E, Walczak C, Plessis MJ, Perin F, Volk A. Morphological and carbogen-based functional MRI of a chemically induced liver tumor model in mice. Magn Reson Med 2003;50(3):522-530.

90. Padhani AR, Gapinski CJ, Macvicar DA, Parker GJ, Suckling J, Revell PB, Leach MO, Dearnaley DP, Husband JE. Dynamic contrast enhanced MRI of prostate cancer: correlation with morphology and tumour stage, histological grade and PSA. Clin Radiol 2000;55(2):99-109.

91. Turnbull LW, Buckley DL, Turnbull LS, Liney GP, Knowles AJ. Differentiation of prostatic carcinoma and benign prostatic hyperplasia: correlation between dynamic Gd-DTPA-enhanced MR imaging and histopathology. J Magn Reson Imaging 1999;9(2):311-316.

92. Diergarten T, Martirosian P, Kottke R, Vogel U, Stenzl A, Claussen CD, Schlemmer HP. Functional characterization of prostate cancer by integrated magnetic resonance imaging and oxygenation changes during carbogen breathing. Invest Radiol 2005;40(2):102-109.

93. Gossmann A, Okuhata Y, Shames DM, Helbich TH, Roberts TP, Wendland MF, Huber S, Brasch RC. Prostate cancer tumor grade differentiation with dynamic contrast-enhanced MR imaging in the rat: comparison of macromolecular and small-molecular contrast media--preliminary experience. Radiology 1999;213(1):265-272.

94. Fan X, River JN, Zamora M, Tarlo K, Kellar K, Rinker-Schaeffer C, Karczmar GS. Differentiation of nonmetastatic and metastatic rodent prostate tumors with high spectral and spatial resolution MRI. Magn Reson Med 2001;45(6):1046-1055.

95. Bhujwalla ZM, Artemov D, Natarajan K, Ackerstaff E, Solaiyappan M. Vascular differences detected by MRI for metastatic versus nonmetastatic breast and prostate cancer xenografts. Neoplasia 2001;3(2):143-153.

96. Kaanders JH, Bussink J, van der Kogel AJ. ARCON: a novel biology-based approach in radiotherapy. Lancet Oncol 2002;3(12):728-737.

97. Robinson SP MD, Howe FA. Assessment of the novel tumor vascular targeting agent zd6126 by non-invasive multi-gradient echo mri.; 2001. p 2234.

98. Gu Y, Bourke VA, Kim JG, Constantinescu A, Mason RP, Liu H. Dynamic response of breast tumor oxygenation to hyperoxic respiratory challenge monitored with three oxygen-sensitive parameters. Appl Opt 2003;42(16):2960-2967.

99. Liu H SY, Worden KL, et al. Noninvasive Investigation of Blood Oxygenation Dynamics of Tumors by Near-Infrared Spectroscopy. Appl Optics 2000;39:5231-5243.

100. Xia M, Kodibagkar V, Liu H, Mason RP. Tumour oxygen dynamics measured simultaneously by near-infrared spectroscopy and (19)F magnetic resonance imaging in rats. Phys Med Biol 2006;51(1):45-60.

101. Hunjan S, Mason RP, Constantinescu A, Peschke P, Hahn EW, Antich PP. Regional tumor oximetry: ^{19}F NMR spectroscopy of hexafluorobenzene. Int J Radiat Oncol Biol Phys 1998;41(1):161-171.

102. Zhao D, Constantinescu A, Hahn EW, Mason RP. Tumor oxygen dynamics with respect to growth and respiratory challenge: investigation of the Dunning prostate R3327-HI tumor. Radiat Res 2001;156(5 Pt 1):510-520.

103. Zhao D, Constantinescu A, Hahn EW, Mason RP. Differential oxygen dynamics in two diverse Dunning prostate R3327 rat tumor sublines (MAT-Lu and HI) with respect to growth and respiratory challenge. Int J Radiat Oncol Biol Phys 2002;53(3):744-756.

104. Kim JG, Zhao D, Song Y, Constantinescu A, Mason RP, Liu H. Interplay of tumor vascular oxygenation and tumor pO_2 observed using near-infrared spectroscopy, an oxygen needle electrode, and ^{19}F MR pO_2 mapping. J Biomed Opt 2003;8(1):53-62.

105. Folkman J. Anti-angiogenesis: new concept for therapy of solid tumors. Ann Surg 1972;175(3):409-416.

106. Denekamp J. Vascular attack as a therapeutic strategy for cancer. Cancer Metastasis Rev 1990;9(3):267-282.

107. Pettit GR, Temple C, Jr., Narayanan VL, Varma R, Simpson MJ, Boyd MR, Rener GA, Bansal N. Antineoplastic agents 322. synthesis of combretastatin A-4 prodrugs. Anticancer Drug Des 1995;10(4):299-309.

108. Davis PD, Dougherty GJ, Blakey DC, Galbraith SM, Tozer GM, Holder AL, Naylor MA, Nolan J, Stratford MR, Chaplin DJ, Hill SA. ZD6126: a novel vascular-targeting agent that causes selective destruction of tumor vasculature. Cancer Res 2002;62(24):7247-7253.

109. Dark GG, Hill SA, Prise VE, Tozer GM, Pettit GR, Chaplin DJ. Combretastatin A-4, an agent that displays potent and selective toxicity toward tumor vasculature. Cancer Res 1997;57(10):1829-1834.

110. Siemann DW, Rojiani AM. Enhancement of radiation therapy by the novel vascular targeting agent ZD6126. Int J Radiat Oncol Biol Phys 2002;53(1):164-171.

111. Murata R, Siemann DW, Overgaard J, Horsman MR. Interaction between combretastatin A-4 disodium phosphate and radiation in murine tumors. Radiother Oncol 2001;60(2):155-161.

112. Murata R, Siemann DW, Overgaard J, Horsman MR. Improved tumor response by combining radiation and the vascular-damaging drug 5,6-dimethylxanthenone-4-acetic acid. Radiat Res 2001;156(5 Pt 1):503-509.

113. Siemann DW, Warrington KH, Horsman MR. Targeting tumor blood vessels: an adjuvant strategy for radiation therapy. Radiother Oncol 2000;57(1):5-12.

114. Thorpe PE, Chaplin DJ, Blakey DC. The first international conference on vascular targeting: meeting overview. Cancer Res 2003;63(5):1144-1147.

115. Li L, Rojiani AM, Siemann DW. Preclinical evaluations of therapies combining the vascular targeting agent combretastatin A-4 disodium phosphate and conventional anticancer therapies in the treatment of Kaposi's sarcoma. Acta Oncol 2002;41(1):91-97.

116. Siemann DW, Rojiani AM. Antitumor efficacy of conventional anticancer drugs is enhanced by the vascular targeting agent ZD6126. Int J Radiat Oncol Biol Phys 2002;54(5):1512-1517.

117. Tozer GM, Prise VE, Wilson J, Locke RJ, Vojnovic B, Stratford MR, Dennis MF, Chaplin DJ. Combretastatin A-4 phosphate as a tumor vascular-targeting agent: early effects in tumors and normal tissues. Cancer Res 1999;59(7):1626-1634.

118. Kragh M, Quistorff B, Horsman MR, Kristjansen PE. Acute effects of vascular modifying agents in solid tumors assessed by noninvasive laser Doppler flowmetry and near infrared spectroscopy. Neoplasia 2002;4(3):263-267.

119. Goertz DE, Yu JL, Kerbel RS, Burns PN, Foster FS. High-frequency Doppler ultrasound monitors the effects of antivascular therapy on tumor blood flow. Cancer Res 2002;62(22):6371-6375.

120. Rustin GJ, Galbraith SM, Anderson H, Stratford M, Folkes LK, Sena L, Gumbrell L, Price PM. Phase I clinical trial of weekly combretastatin A4 phosphate: clinical and pharmacokinetic results. J Clin Oncol 2003;21(15):2815-2822.

121. Galbraith SM, Maxwell RJ, Lodge MA, Tozer GM, Wilson J, Taylor NJ, Stirling JJ, Sena L, Padhani AR, Rustin GJ. Combretastatin A4 phosphate has tumor antivascular activity in rat and man as demonstrated by dynamic magnetic resonance imaging. J Clin Oncol 2003;21(15):2831-2842.

122. Prise VE, Honess DJ, Stratford MR, Wilson J, Tozer GM. The vascular response of tumor and normal tissues in the rat to the vascular targeting agent, combretastatin A-4-phosphate, at clinically relevant doses. Int J Oncol 2002;21(4):717-726.

123. Robinson SP, McIntyre DJ, Checkley D, Tessier JJ, Howe FA, Griffiths JR, Ashton SE, Ryan AJ, Blakey DC, Waterton JC. Tumour dose response to the antivascular agent ZD6126 assessed by magnetic resonance imaging. Br J Cancer 2003;88(10):1592-1597.

124. McIntyre DJ, Robinson SP, Howe FA, Griffiths JR, Ryan AJ, Blakey DC, Peers IS, Waterton JC. Single dose of the antivascular agent, ZD6126 (N-acetylcolchinol-O-phosphate), reduces perfusion for at least 96 hours in the GH3 prolactinoma rat tumor model. Neoplasia 2004;6(2):150-157.

125. Padhani AR. MRI for assessing antivascular cancer treatments. Br J Radiol 2003;76 Spec No 1:S60-80.

126. Horsman MR, Ehrnrooth E, Ladekarl M, Overgaard J. The effect of combretastatin A-4 disodium phosphate in a C3H mouse mammary carcinoma and a variety of murine spontaneous tumors. Int J Radiat Oncol Biol Phys 1998;42(4):895-898.

127. Horsman MR, Murata R. Vascular targeting effects of ZD6126 in a C3H mouse mammary carcinoma and the enhancement of radiation response. Int J Radiat Oncol Biol Phys 2003;57(4):1047-1055.

128. Hunjan S, Zhao D, Constantinescu A, Hahn EW, Antich PP, Mason RP. Tumor oximetry: demonstration of an enhanced dynamic mapping procedure using fluorine-19 echo planar magnetic resonance imaging in the Dunning prostate R3327-AT1 rat tumor. Int J Radiat Oncol Biol Phys 2001;49(4):1097-1108.

129. Mason RP, Ran S, Thorpe PE. Quantitative assessment of tumor oxygen dynamics: molecular imaging for prognostic radiology. J Cell Biochem Suppl 2002;39:45-53.

130. Pedley RB, Hill SA, Boxer GM, Flynn AA, Boden R, Watson R, Dearling J, Chaplin DJ, Begent RH. Eradication of colorectal xenografts by combined radioimmunotherapy and combretastatin a-4 3-O-phosphate. Cancer Res 2001;61(12):4716-4722.

131. Song Y, Worden KL, Jiang X, Zhao D, Constantinescu A, Liu H, Mason RP. Tumor oxygen dynamics: comparison of ^{19}F MR EPI and frequency domain NIR spectroscopy. Adv Exp Med Biol 2003;530:225-236.

132. Song Y, Constantinescu A, Mason RP. Dynamic breast tumor oximetry: the development of prognostic radiology. Technol Cancer Res Treat 2002;1(6):471-478.

133. Brown JM. The hypoxic cell: a target for selective cancer therapy--eighteenth Bruce F. Cain Memorial Award lecture. Cancer Res 1999;59(23):5863-5870.

134. Hockel M, Schlenger K, Aral B, Mitze M, Schaffer U, Vaupel P. Association between tumor hypoxia and malignant progression in advanced cancer of the uterine cervix. Cancer Res 1996;56(19):4509-4515.

135. Brizel DM, Scully SP, Harrelson JM, Layfield LJ, Bean JM, Prosnitz LR, Dewhirst MW. Tumor oxygenation predicts for the likelihood of distant metastases in human soft tissue sarcoma. Cancer Res 1996;56(5):941-943.

136. Hockel M, Vaupel P. Tumor hypoxia: definitions and current clinical, biologic, and molecular aspects. J Natl Cancer Inst 2001;93(4):266-276.

137. Zhao D, Jiang L, Constantinescu A, Mason RP. Evaluation of breast tumor microcirculationand oxygenation using a combination of BOLD, DCE and ^{19}F MRI [abstract]. Proc Int Soc Magn Reson Med Kyoto, 2004:1:222.

138. Beauregard DA, Pedley RB, Hill SA, Brindle KM. Differential sensitivity of two adenocarcinoma xenografts to the anti-vascular drugs combretastatin A4 phosphate and 5,6-dimethylxanthenone-4-acetic acid, assessed using MRI and MRS. NMR Biomed 2002;15(2):99-105.

139. Le D, Mason RP, Hunjan S, Constantinescu A, Barker BR, Antich PP. Regional tumor oxygen dynamics: ^{19}F PBSR EPI of hexafluorobenzene. Magn Reson Imaging 1997;15(8):971-981.

140. Mason RP, Rodbumrung W, Antich PP. Hexafluorobenzene: a sensitive ^{19}F NMR indicator of tumor oxygenation. NMR Biomed 1996;9(3):125-134.

141. Vaupel P, Mayer A. Hypoxia and anemia: effects on tumor biology and treatment resistance. Transfus Clin Biol 2005;12(1):5-10.

142. Vaupel P, Hockel M. Blood supply, oxygenation status and metabolic micromilieu of breast cancers: characterization and therapeutic relevance. Int J Oncol 2000;17(5):869-879.

143. Thomlinson RH, Gray LH. The histological structure of some human lung cancers and the possible implications for radiotherapy. Br J Cancer 1955;9(4):539-549.

144. Gray LH, Conger AD, Ebert M, Hornsey S, Scott OC. The concentration of oxygen dissolved in tissues at the time of irradiation as a factor in radiotherapy. Br J Radiol 1953;26(312):638-648.

145. Mason RP, Hunjan S, Le D, Constantinescu A, Barker BR, Wong PS, Peschke P, Hahn EW, Antich PP. Regional tumor oxygen tension: fluorine echo planar imaging of hexafluorobenzene reveals heterogeneity of dynamics. Int J Radiat Oncol Biol Phys 1998;42(4):747-750.

146. Watanabe K, Nomori H, Ohtsuka T, Naruke T, Uno K. [False negative cases of F-18 fluorodeoxyglucose-positron emission tomography (FDG-PET) imaging in small lung cancer less than 3 cm in size]. Nihon Kokyuki Gakkai Zasshi 2004;42(9):787-793.

147. Mazurchuk R, Spernyak JA. Magnetic resonance imaging of tumor response to chemotherapy. Methods Mol Med 2005;111:381-415.

148. Murakami M, Imahori Y, Kimura S, Tatsuzawa K, Ohwada K, Inoue Y, Sasajima H, Mineura K. Positron emission tomography elucidates transport system and tumor proliferation in meningiomas. Oncol Rep 2005;14(4):853-859.

149. Schirner M, Menrad A, Stephens A, Frenzel T, Hauff P, Licha K. Molecular imaging of tumor angiogenesis. Ann N Y Acad Sci 2004;1014:67-75.

150. Brix G, Semmler W, Port R, Schad LR, Layer G, Lorenz WJ. Pharmacokinetic parameters in CNS Gd-DTPA enhanced MR imaging. J Comput Assist Tomogr 1991;15(4):621-628.

151. Kitagawa K, Sakuma H, Ishida N, Hirano T, Ishihara A, Takeda K. Contrast-enhanced high-resolution MRI of invasive breast cancer: correlation with histopathologic subtypes. AJR Am J Roentgenol 2004;183(6):1805-1809.

152. Vaupel P, Briest S, Hockel M. Hypoxia in breast cancer: pathogenesis, characterization and biological/therapeutic implications. Wien Med Wochenschr 2002;152(13-14):334-342.

153. Shannon AM, Bouchier-Hayes DJ, Condron CM, Toomey D. Tumour hypoxia, chemotherapeutic resistance and hypoxia-related therapies. Cancer Treat Rev 2003;29(4):297-307.

154. Zhao D, Constantinescu A, Jiang L, Hahn EW, Mason RP. Prognostic radiology: quantitative assessment of tumor oxygen dynamics by MRI. Am J Clin Oncol 2001;24(5):462-466.

155. Jain RK. Normalization of tumor vasculature: an emerging concept in antiangiogenic therapy. Science 2005;307(5706):58-62.

156. Van Den Bossche B, Van Belle S, De Winter F, Signore A, Van de Wiele C. Early Prediction of Endocrine Therapy Effect in Advanced Breast Cancer Patients Using 99mTc-Depreotide Scintigraphy. J Nucl Med 2006;47(1):6-13.

VITAE

Lan Jiang was born in Chongqing, P.R. of China, on August 11,1962, the son of Wenqing Jiang and Baozhong Zheng. After completing his study at Nan Kai High School, Chongqing, in 1979, he entered the PLA Electronic Technology University. He received the degree of Bachelor of computer engineering in July, 1983. Then, He was a teacher in Third Military Medical University for teaching medical students basic computer knowledge, such as, BASIC language, DBASE database, and DOS operation system. In September, 1988 he entered the Graduate School of Chongqing University to study image processing and pattern recognition. He completed his M.S. proposal for lung cancer cell image processing and computer automatic recognition algorithm design. He was awarded the M.S. degree in Computer Science in July, 1991. Then, he worked in Lab of Microcirculation at 301 hospital in Beijing. At that time, he studied physiology, cardiovascular physiology, anatomy, fluid dynamics, and homodynamics by himself. His work was focused on macro- and micro-circulatory path-physiological research. During this period, he won the awards of National Natural Science Foundation of China and the National Science Technical Invention Award of China. In 1998, he received a postdoctoral fellow position and worked in Department of Physiology, Loma Linda University, CA, USA. In 2000, he joined Dr. Mason's group as research fellow in UT Southwestern Medical Center. In 2001, he enrolled in the Graduate Program of Radiological Sciences to pursue his doctoral research. In 2001, he married Hong Qiao in Dallas, TX. The older son David Jiang was born in 2001 and younger son Yixing (Jacky) Jiang was born in 2003.

Permanent Address: 4-8 Gaotan village No.2.

Sa Ping Bar qui, Chongqing

P.R. of China 400038